Neck Sense Rope System and Leaching Studies for SNO+

BY

Pouya Khaghani

Thesis submitted in partial fulfillment
of the requirements for the degree of
Master of Science (M.Sc.) in Physics

The Faculty of Graduate Studies
Laurentian University
Sudbury, Ontario, Canada

© P. Khaghani 2016

THESIS DEFENCE COMMITTEE/COMITÉ DE SOUTENANCE DE THÈSE
Laurentian Université/Université Laurentienne
Faculty of Graduate Studies/Faculté des études supérieures

Title of Thesis Titre de la thèse	Neck Sense Rope System and Leaching Studies for SNO+
Name of Candidate Nom du candidat	Khaghani, Pouya
Degree Diplôme	Master of Science
Department/Program Département/Programme	Physics
Date of Defence Date de la soutenance	November 16, 2015

APPROVED/APPROUVÉ

Thesis Examiners/Examinateurs de thèse:

Dr. Christine Kraus
(Supervisor/Directeur(trice) de thèse)

Dr. Fraser Duncan
(Committee member/Membre du comité)

Dr. Jacques Farine
(Committee member/Membre du comité)

Dr. Wolfgang Rau
(External Examiner/Examinateur externe)

Approved for the Faculty of Graduate Studies
Approuvé pour la Faculté des études supérieures
Dr. David Lesbarrères
Monsieur David Lesbarrères
Dean, Faculty of Graduate Studies
Doyen, Faculté des études supérieures

ACCESSIBILITY CLAUSE AND PERMISSION TO USE

I, **Pouya Khaghani**, hereby grant to Laurentian University and/or its agents the non-exclusive license to archive and make accessible my thesis, dissertation, or project report in whole or in part in all forms of media, now or for the duration of my copyright ownership. I retain all other ownership rights to the copyright of the thesis, dissertation or project report. I also reserve the right to use in future works (such as articles or books) all or part of this thesis, dissertation, or project report. I further agree that permission for copying of this thesis in any manner, in whole or in part, for scholarly purposes may be granted by the professor or professors who supervised my thesis work or, in their absence, by the Head of the Department in which my thesis work was done. It is understood that any copying or publication or use of this thesis or parts thereof for financial gain shall not be allowed without my written permission. It is also understood that this copy is being made available in this form by the authority of the copyright owner solely for the purpose of private study and research and may not be copied or reproduced except as permitted by the copyright laws without written authority from the copyright owner.

Abstract

SNO+ is a multipurpose scintillation-based neutrino experiment which is located at SNOLAB, Creighton mine, Sudbury. The primary scientific goal of the experiment is searching for the elusive process of neutrinoless double beta decay of ^{130}Te. In addition to $0\nu\beta\beta$ decay, SNO+ will be able to detect low energy solar neutrinos, geo- and reactor- anti-neutrinos, as well as supernova neutrinos. During an initial water phase, it will also search for invisible modes of nucleon decay.

This thesis briefly introduces neutrino physics and discusses the milestones in chapter 1. Chapter 2 discusses the SNO+ experiment in detail and outlines important developments in SNO+. Furthermore, chapter 3 and chapter 4 describe the two main projects that have been done by the author: i) leaching studies for the SNO+ experiment and ii) the neck sense rope system.

Looking for rare events requires very stringent background limits. One of the sources of background originates from ^{222}Rn daughters implanted into the inner surface of the SNO+ acrylic vessel. They can leach into the detector volume and increase the level of internal background. A leaching model has been developed by the author to estimate the activity and contribution to the backgrounds. The model is compatible with the measured value from a lead assay to within 1 sigma.

The SNO+ sense rope system is a mechanical system which monitors displacement of the AV neck to within 2mm accuracy. The system has been calibrated and installed underground alongside with the sliding floor. Chapter 4 discusses the system, the performed calibration and the installation procedure in more detail.

Acknowledgment

First and foremost, I would like to thank my supervisor, Christine Kraus for her continual support of my research, for her guidance, patience and her remarkable perseverance. With no doubt, working in her research group was the most rewarding experience in my life.

I would also like to thank Erica Caden who was a great source of advice. The sense rope project would have never been completed without her support. I would like to thank Valentina Lozza for advising me on the leaching studies and also Oleg Chkvorets for the helpful discussions and his positive sense of humor. Also, thanks to Chris Jillings for his valuable help on the sense rope calibration and his positive attitude toward the work. Many thanks to Dave Braid, Noel and Cam for their valuable helps on the sense rope calibration, electronics and installation. Without their support the sense rope system would have never been calibrated and installed in such a short span of time. Thanks to Erin who helped me a lot at the beginning of the sense rope calibration, Zack Barnard and Phil Rost for their helpful advice and discussions. I would also like to thank all the SNO+ members and the SNOLAB crew for all the good times working underground.

I would also like to thank my committee members, Dr. Jacques Farine, Dr. Fraser Duncan and Dr. Wolfgang Rau for taking the time to review my thesis.

I would like to thank my selfless parents for their continual support of my education and my uncles, my lovely aunt and my cousins for being an ever-present source of assistance. Thanks to my roommates, Zack, John, Adelle, Valeria and Negar for all the good times at 62 Gill St. and for doing the household chores on behalf of me. I would also like to thank Maggie for making the best french onion soup that I have ever had.

Finally, I would like to thank everyone who went out of their ways to give me a lift for early SNOLAB cages.

Table of Contents

List of Tables

List of Figures

Chapter 1: Neutrino Physics

> "*I have done something very bad today by proposing a particle that can not be detected; something no theorist should do ever.*" [1]
>
> — Wolfgang Paui

1.1 Introduction

Neutrinos, or "little neutral particles", are charge-less fermions which rarely interact. They are very abundant in the universe. They only interact through the weak nuclear force which has a much shorter range and is much weaker the other forces, therefore they typically pass through matter unimpeded. To illustrate that: roughly 10^{15} neutrinos passing through your body each second, completely unnoticed! There are three types, or "flavors", of neutrinos; electron type, muon type and tau type denoted by ν_e, ν_μ and ν_τ. The mass of neutrino is very tiny and their cross section to interact with an electron is about $10^{-48}\mathrm{m}^2$ [2] which is also small compared to the rest of the particles. Therefore, large detectors were built deep underground to observe these weakly interacting particles, where there are few cosmic rays to mask their signal. Data from underground experiments have led to significant discoveries in neutrino physics such as neutrino oscillations, where one type of neutrino changes into another type as it propagates. This chapter briefly reviews the historical milestones in the field of neutrino physics, summarizes our current understanding of neutrinos and discusses some open questions in the field.

1.2 The Birth of the Neutrino

1.2.1 The Electron Neutrino

The neutrino was first proposed by Wolfgang Pauli in 1930 to explain the continuous energy spectrum of beta emission [3]. If there were no neutrinos the spectrum would have discrete energies. The first milestone in the theory was when Enrico Fermi in 1934 formulated a theory of β-decay, now known as Fermi theory [3][4]. He also postulated that neutrinos would be mass-less particles.

The Fermi theory was remarkably successful describing the discoveries of muon particles and muon decay but still left a few in doubt of the neutrino's existence till the early 1950s when F. Reines and C. L. Cowan started searching for a way to measure inverse β-decay [5] where an anti-neutrino produces a positron and a neutron, shown in equation 1.1. After considering several methods, including a nuclear explosion, they ended up using 1400 liters of liquid scintillator as the detection medium next to a nuclear reactor. A nuclear reactor can produce large flux of anti-neutrinos. In June of 1956, Reines and Cowan sent a telegram informing Pauli of the direct detection of anti-neutrinos in their experiment, a result that was rewarded with the 1995 Nobel Prize.

$$\bar{\nu}_e + \mathrm{p} \longrightarrow n + \mathrm{e}^+ \tag{1.1}$$

1.2.2 Parity Violation

Conservation of parity states that the physical process of a system is invariant under space inversion, for instance moving from right-handed coordinates to left-handed coordinates. Parity conservation was firmly established in the electromagnetic and strong interactions

but for several years physicists had puzzled over the parity violation in the weak interactions. In 1956 C. Yang and T. Lee predicted the parity violation in the weak interactions [6] and also suggested several experiments to test the issue including the beta decay from polarized ^{60}Co. This experiment was performed in 1957 by C. S. Wu and parity violation was observed in beta decay [7]. Subsequent experiments confirmed the results and showed that neutrinos have their spin pointed in the opposite direction of their momentum, which is called a left-handed as a result [11], while the anti-neutrino is right-handed.

1.2.3 Discovery of the Muon and Tau Neutrinos

In 1962, the second type of neutrino, ν_μ, was observed in Brookhaven National Laboratory using the decay of pions [8], as shown in equation 1.2 and named after its associated lepton. L. Lederman, M. Schwartz and J. Steinberger were awarded the 1988 Nobel prize for the neutrino beam method and the demonstration of the doublet structure of the leptons through this discovery.

$$\begin{aligned} \pi^+ &\longrightarrow \mu^+ + \nu_\mu & \\ & & \mu^+ &\longrightarrow e^+ + \nu_e + \bar{\nu_\mu} \\ \pi^- &\longrightarrow \mu^- + \bar{\nu_\mu} & \\ & & \mu^- &\longrightarrow e^- + \bar{\nu_e} + \nu_\mu \end{aligned} \tag{1.2}$$

In 1975, the third generation of leptons, the tau particle, was discovered at the Stanford Linear Accelerator Center (SLAC) [9] and the existence of the third flavor corresponding neutrino, ν_τ, was suggested. Finally, in July 2000, the DONUT (Direct Observation of the NU Tau) collaboration located at Fermilab, announced the discovery of tau neutrino in the tau decay [10].

1.2.4 Neutrinos in the Standard Model

The Standard Model of particle physics identifies the fundamental particles and provides a method of calculating their interaction cross sections with exceptional accuracy. Since its formulation, it has been an invaluable tool and has provided enormous predictive power by theorizing new particles that were later observed. The Standard Model classifies particles into two groups based on their spin, the intrinsic angular momentum held by a particle. Bosons have spin in integer units of $\hbar$(0,1,2...) and Fermions have half integer spin in units of $\hbar$(1/2, 3/2,...). There are 12 fundamental Fermions that are the building blocks of matter and 5 fundamental Bosons which are force carriers as shown in figure 1.1. According to the standard model, neutrinos are massless particles which interact through the weak force by coupling to the massive W and Z bosons. Interactions involving the charged W bosons such as inverse beta decay are called Charged Current (CC) reactions and interactions with the neutral Z boson such as ν_x-e scattering are called Neutral Current (NC) reactions, where ν_x represents every type of neutrino. Despite the standard model's remarkable success, still a number of observed phenomena cannot be described by the theory such as neutrino oscillation. Experiments have observed that one type of neutrino can change into another type of neutrino, a process known as neutrino oscillations. This can only happen if neutrinos have a nonzero mass. This will be discussed in more detail in the following sections.

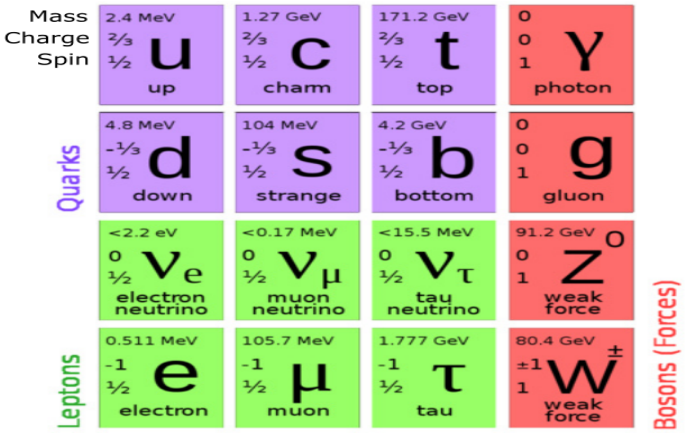

Figure 1.1: Table of the elementary particles in the standard model. It shows three generations of matter and the gauge bosons in the fourth column (red).

1.3 Sources of Neutrinos

There are various sources of neutrinos all around the universe, ranging from a nuclear power plant to an extra-galactic supernova. Neutrinos are continually produced through nuclear fusion reactions in the core of the sun or other stars, the beta decay of radioactive materials, and the interaction of high energy cosmic rays with the atmosphere. The sun is the biggest neutrino factory in our neighborhood, in terms of the intensity of the flux of neutrinos on earth which is roughly 7×10^{10}neutrinos/cm^2/s [12].

β^- decay branches of ^{40}K, ^{232}Th and ^{238}U inside the earth are also one of the sources of anti-neutrinos. Only anti-neutrinos from ^{232}Th and ^{238}U decay chains can be detected through inverse beta decay interaction, since they have energies above the corresponding threshold (1.8 MeV). Nuclear reactors whose fission products undergo beta decay, and accelerator are also common sources of neutrinos on earth. Table 1.1 shows various sources of neutrinos on earth, their average energies and flux.

The most important extra-solar system sources of neutrinos are Supernova events. Core-collapse SNe are the final explosion of single stars with mass between about 89 and 4060 solar masses produce large fluxes of neutrinos.

Source	**Type**	**Average Energy**	**Intensity**	Ref
Sun	ν_e	0.53 MeV	$7{\times}10^{10}$/cm^2/s	[12]
Atmospheric	ν_e,ν_μ	1 GeV	1/cm^2/s	[15]
Supernova	all	15 MeV	10^{57}/explosion	[16]
Geo-neutrinos	$\bar{\nu_e}$	0.5 MeV	4×10^6/cm^2/s	[13]
Nuclear Reactors	$\bar{\nu_e}$	4 MeV	$1.5 \times 10^{20}/s$ for 1 GWth reactor	[14]

Table 1.1: Various sources of neutrinos.

In a type II Supernova roughly 99% of the gravitational binding energy is released as the emission of all three flavor of neutrinos. On 24 February 1987 a very bright Supernova of type II, SN1987A, was discovered in the Large Magellanic cloud, at a distance of about 50 kpc from the solar system [17][18]. Three large underground neutrino detectors potentially

sensitive to SN neutrinos: Kamiokande-II [19], IMB [20], and Baksan [21][22], observed an unusual number of events with energy of the order of 10 MeV within a time window of the order of 13 s in the hours before the optical discovery. The observation of SN1987A neutrinos marked the beginning of "extra-solar system neutrino astronomy".

1.3.1 Solar Neutrinos

The Standard Solar Model (SSM) is a model based on theories and experimental observations which describes amongst other things various nuclear reactions in the Sun and predicts the flux of solar neutrinos [12]. The majority of solar neutrinos (∼98%) are produced through the proton-proton chain reactions (*pp*) shown in figure 1.2b. Additionally, chain reactions involving heavier elements, called the CNO cycle (figure 1.2a), produce solar neutrinos (∼2%) with higher energy levels ($\langle E_\nu \rangle \sim 0.9$ MeV) compared to *pp* neutrinos ($\langle E_\nu \rangle \sim 0.27$ MeV) [23]. Furthermore, ^{8}B produces relatively small number of solar neutrinos with higher energy levels (∼6.7 MeV). The energy spectra of solar neutrinos are shown in figure 1.3.

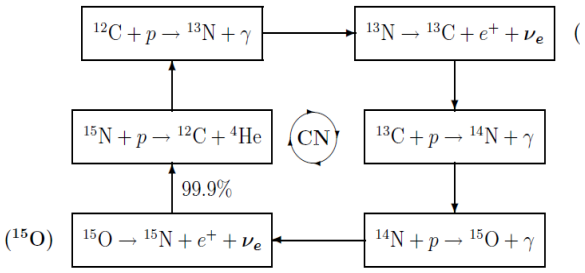

(a) The CNO cycle.

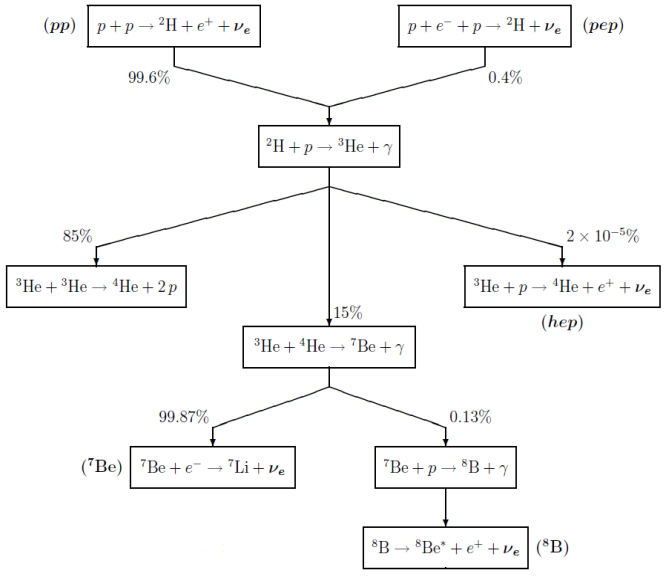

(b) The *pp* chain.

Figure 1.2: Figure (a) shows the solar neutrinos which are produced through the CNO cycle. Figure (b) shows the *pp* chain. The produced neutrinos are in boldface.

The first measurement of solar neutrinos was accomplished by R. Davis in 1968. Davis

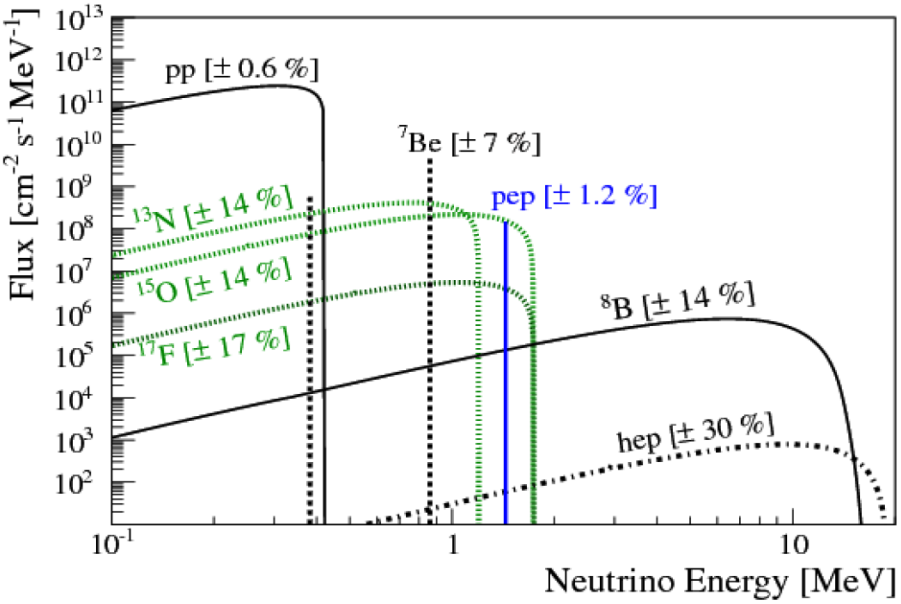

Figure 1.3: Energy spectra of neutrino fluxes from the pp and CNO chains, as predicted by the SSM. For continuous sources, the differential flux is in cm^2 s^{-1} MeV^{-1}. For the lines, the flux is in cm^2 s^{-1} [23].

built a detector which consisted of a 378,000 litre tank of tetracholorethylene (C_2Cl_4) which he constructed underground in a gold mine called Homestake [24][25][26]. Neutrinos were detected through a reaction described by equation 1.3 where the neutrino changes a chlorine atom to an argon atom. The decay of ^{37}Ar was measured in a proportional counter. The measured result was incompatible with the theory. The measured flux of solar neutrinos was only about a third of the flux predicted by the SSM [27]. The discrepancy between the theoretical expectation and the observed number of solar neutrinos was also confirmed by other experiments such as Kamiokande-II [28], IBM [29] and GALLEX [30]. This would come to be known as the solar neutrino problem.

$$\nu_e + {}^{37}\mathrm{Cl} \longrightarrow {}^{37}\mathrm{Ar} + \mathrm{e}^- \tag{1.3}$$

1.3.1.1 Sudbury Neutrino Observatory

In 1985, H. Chen proposed an experiment to resolve the Solar Neutrino Problem. The SNO (Sudbury Neutrino Observatory) experiment was built between 1990-1999 and located in Creighton Mine, Sudbury, Ontario, Canada. The experiment was placed 2km underground

which provides 6000m water equivalent of shielding against cosmic radiation. The detection target medium was 1,000 tonnes of heavy water contained inside a 6m radius Acrylic Vessel, known as AV. In order to detect the light signal, the AV is surrounded by approximately 9500 photo-multiplier tubes (PMTs) which are mounted on a stainless steel frame, known as the PMT support structure (PSUP). In addition, 7400 tonnes of ultra pure water were held inside the cavity volume, as a shielding against radioactive backgrounds coming from the surrounding rock (cavity walls). The SNO detector is shown in figure 1.4b.

SNO had two main reaction channels; one sensitive to the electron type neutrinos, charged current interaction (CC) shown in equation 1.4, and the other sensitive to every type of neutrino equally, neutral current interaction (NC) as shown in equation 1.5. Additionally, neutrinos were detected through neutrino-electron elastic scattering (ES) see equation 1.6.

$$\nu_e + \mathrm{d} \longrightarrow \mathrm{p} + \mathrm{p} + \mathrm{e}^- \qquad (CC) \tag{1.4}$$

$$\nu_x + \mathrm{d} \longrightarrow \nu_x + \mathrm{n} + \mathrm{p} \qquad (NC) \tag{1.5}$$

$$\nu_x + \mathrm{e}^- \longrightarrow \nu_x + \mathrm{e}^- \qquad (ES) \tag{1.6}$$

The SNO experiment took data between 1999 and 2006. The SNO collaboration published their first result in 2001 and confirmed that the total measured flux of all flavor neutrinos is compatible with the solar model prediction, while the flux of ν_e are only a third of the total flux [31].

By comparing charged-current neutrinos, ν_e, with neutral current neutrinos , ν_x (see figure 1.4a), the SNO collaboration showed that the missing solar neutrinos are the result of neutrino flavor transformation, a process known as neutrino oscillation.

The first evidence for neutrino oscillation was observed by the Super-Kamiokande experiment measuring the atmospheric neutrinos flux [32]. The SNO result was a solid confirmation of neutrino oscillations and consistent with the results from Super-Kamiokande.

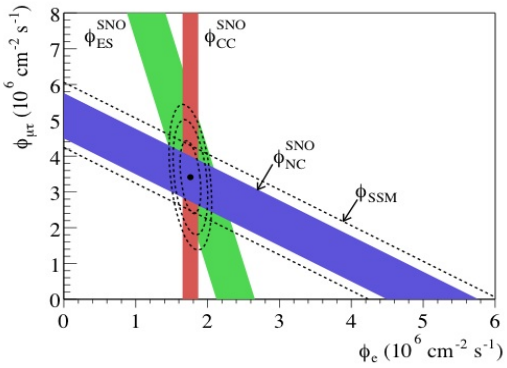

(a) Taken from [33]

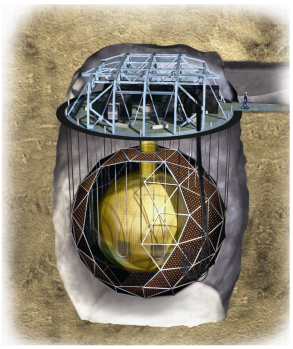

(b) SNO Detector

Figure 1.4: Figure (a): Flux of ^8B solar neutrinos which are τ or μ flavor vs flux of electron neutrinos deduced from the three neutrino reactions in SNO. The diagonal bands show the total flux as predicted by the Solar Model (dashed lines) and that measured with the NC reaction in SNO (solid band). Figure (b) shows the SNO detector which is suspended inside the cavity volume and surrounded by photo-multiplier tubes.

Additionally, neutrino flavor oscillation implied that neutrinos have non-zero mass states. SNO+ is the successor of the SNO experiment and will utilize most of the hardware including the detector. Chapter 2 describes the SNO+ experiment in more detail.

1.4 Neutrino Oscillation

Neutrino oscillation is a quantum mechanical phenomenon proposed in 1957 by Pontecorvo in analogy with kaon oscillations [34]. Neutrino experiments confirmed that neutrinos change flavor as they propagate through space. This implies that neutrinos have three mass eigenstates in the free space Hamiltonian, $|\nu_k\rangle$ (k=1, 2, 3), which are not identical with their flavor eigenstates, $|\nu_\alpha\rangle$ ($\alpha = e, \mu, \tau$). The flavor eigenstates can be written in terms of mass states as follows

$$|\nu_\alpha\rangle = \sum_{i=1}^{3} U_{\alpha k} |\nu_k\rangle \tag{1.7}$$

where $U_{\alpha k}$ is called Pontecorvo-Maki-Nakagawa-Sakata matrix (PMNS). $U_{\alpha k}$ is a unitary operator (matrix) which transforms the neutrino mass states to the flavor states. As with any unitary matrices, PMNS matrix can be expressed in terms of three rotation angles plus one complex phase. The mixing angles for neutrino oscillation are known as θ_{12}, θ_{23}, and

θ_{13}. The transformation matrix can be expressed as a product of three matrices as shown in equation 1.8.

$$U_{\alpha k} = \begin{pmatrix} 1 & 0 & 0 \\ 0 & c_{23} & s_{23} \\ 0 & -s_{23} & c_{23} \end{pmatrix} \times \begin{pmatrix} c_{13} & 0 & s_{13}e^{-i\delta} \\ 0 & 1 & 0 \\ -s_{13}e^{i\delta} & 0 & c_{13} \end{pmatrix} \times \begin{pmatrix} c_{12} & s_{12} & 0 \\ -s_{12} & c_{12} & 0 \\ 0 & 0 & 1 \end{pmatrix} \tag{1.8}$$

where $c_{ij} = \cos\theta_{ij}$, $s_{ij} = \sin\theta_{ij}$, and δ is the CP-violating phase (Dirac phase). Neutrino oscillation is a direct result of non-zero mixing angles. The probability for a neutrino produced as an α-type to be detected as a β-type can be expressed in terms of the distance between the source and the detector, L, mixing angles, and the differences of the squares of the masses, Δm^2_{ij} which comes from the Hamiltonian. In the case of two neutrino mixing, there is only one squared-mass difference. Equation 1.9 shows the probability for the two-neutrino case where E_ν represents the energy of neutrinos in GeV.

$$P_{\alpha\to\beta} = \sin^2 2\theta_{12} \sin\left(\frac{1.27\Delta m^2_{12}(\mathrm{eV}^2)L(\mathrm{km})}{E_\nu(\mathrm{GeV})}\right) \tag{1.9}$$

According to the direct and indirect measurements, the current best-fit values (as of July 2014) for the mixing angles are $\theta_{12} = 33.36^{\circ}{}^{+0.81^{\circ}}_{-0.78^{\circ}}$, $\theta_{23} = 40.0^{\circ}{}^{+2.1^{\circ}}_{-1.5^{\circ}}$ or $50.4^{\circ}{}^{+1.3^{\circ}}_{-1.3^{\circ}}$, and $\theta_{13} = 8.66^{\circ}{}^{+0.44^{\circ}}_{-0.46^{\circ}}$ [35]. As it is obvious from equation 1.9, the probability is only sensitive to the squared-mass difference but not the absolute mass of neutrinos. According to the solar and atmospheric measurements, there are two possible orders for the mass states, known as neutrino mass hierarchies which are shown in figure 1.5. One of the questions which is still unanswered about neutrinos is whether Δm^2_{13} has a positive or negative sign. Conventionally, the case where $\Delta m^2_{13} > 0$ is called the normal hierarchy, and $\Delta m^2_{13} < 0$ is known as the inverted hierarchy.

According to the Particle Data Group (PDG 2015), the current best values of squared-mass differences, are $\Delta m^2_{12} = 7.58^{+0.19}_{-0.20} \times 10^{-5}\mathrm{eV}^2$ measured by the KamLAND experiment [36], and $\Delta m^2_{23} = 2.35^{+0.12}_{-0.08} \times 10^{-3}\mathrm{eV}^2$ measured by the Minos experiment [37].

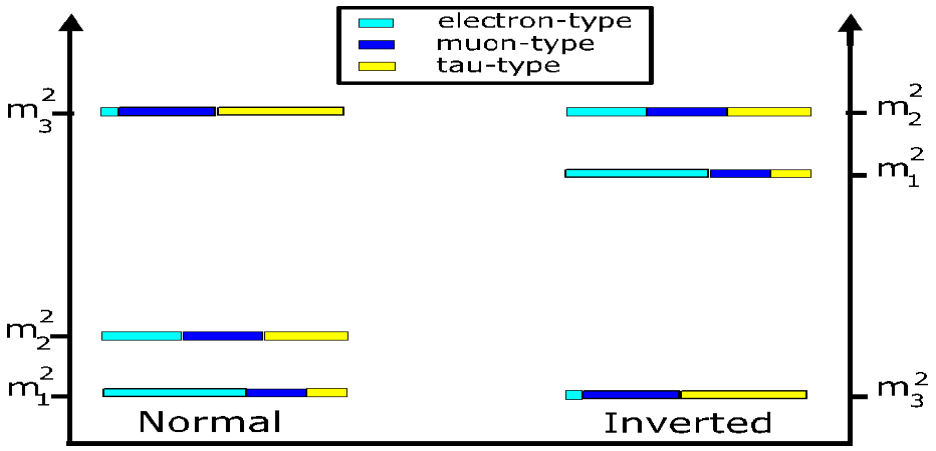

Figure 1.5: Two possible neutrino mass orderings, known as the normal hierarchy ($\Delta m^2_{13} > 0$), and the inverted hierarchy ($\Delta m^2_{13} < 0$).

1.5 Direct Measurements of Neutrino Mass

In 1933, Fermi and Perrin studied the effect of massive neutrinos in beta decays and concluded that the results are compatible with the neutrino as a mass-less particle [48]. Although, as we discussed in the last section, the results from neutrino oscillation experiments proved that neutrinos are actually massive particles. These experiments are just sensitive to squared-mass difference and so far we know that there are at least two massive neutrinos, one with a mass larger than about $\sqrt{\Delta m^2_{21}} \approx 9 \times 10^{-3}$eV and the other one with a mass larger than about $\sqrt{\Delta m^2_{32}} \approx 5 \times 10^{-2}$eV. Further information on the absolute mass of neutrinos should be investigated with other methods which will be described in the following sections.

1.5.1 Beta Decay Experiments

One of the most sensitive methods to measure the mass of ν_e is by observing the end point of the electron spectrum in beta decay (equation 1.10). Since the electron type neutrino is a flavor eigen-state, it does not have any particular mass but it can be assumed as a mixture of different mass states. The neutrino mass shifts the end point of the electron spectrum slightly.

$$ {}^{A}_{Z}X \longrightarrow {}^{A}_{Z+1}X^{'} + \mathrm{e}^{-} + \bar{\nu}_{e} \tag{1.10} $$

Since the rate of the events goes to zero at the end point, in practice it is very difficult to measure the end point of the electron spectrum and it requires very high energy resolution. The emitted electron and anti-neutrino share the beta emission energy, therefore least energetic beta decay isotopes are the best candidates for this method. Using tritium which has one the least energetic beta decays (∼18.6 keV), Mainz [49] and Troitsk [50] experiments put an upper limit on the mass of electron neutrino ($m_{\nu_e} < 2.3$eV). The Mainz and Troitsk collaborations merged in a joint collaboration called KATRIN which will reach the sensitivity of 0.2eV [51].

1.5.2 Neutrinoless Double Beta Decay

The idea of double beta decay was first proposed by Maria Goeppert-Mayer in 1935 [52]. Double beta decay occurs when a single beta decay is energetically forbidden for a nucleus, or when beta decay violates the angular momentum selection rules. The nucleus can undergo two beta decays simultaneously, where two neutrons are converted to two protons, two electrons, and two anti-neutrinos (shown in equation 1.11). This process is theoretically possible for 26 isotopes and has been experimentally observed for 11 isotopes.

$$ {}^{A}_{Z}X \longrightarrow {}^{A}_{Z+2}X^{'} + 2\,\mathrm{e}^{-} + 2\bar{\nu}_{e} \tag{1.11} $$

Neutrinoless double beta decay, $0\nu\beta\beta$, was first proposed by W. H. Furry in 1939 [38], which is a process by which two neutrons are converted to two protons and two electrons but no neutrinos are emitted (see equation 1.12). This reaction is forbidden in the standard model of particle physics since it violates the lepton number conservation rules.

$$ {}^{A}_{Z}X \longrightarrow {}^{A}_{Z+2}X^{'} + 2\,\mathrm{e}^{-} \tag{1.12} $$

This process would be possible if neutrinos behave as massive Majorana particles; In other words, the neutrino acts as its own anti-particle. Therefore, the emmited neutrino by a nucleon can be absorbed by the other nucleon and all of the energy would be transferred to the electrons. In this case, a nucleus which can decay through $2\nu\beta\beta$, can also undergo $0\nu\beta\beta$, although with a different lifetime. Neutrinoless double beta decay experiments are the most promising way to find if neutrinos are Majorana particles. Additionally, it can help us to measure the absolute mass scale of the neutrino. The decay rate for neutrinoless double beta decay, $\Gamma^{0\nu\beta\beta}$, is proportional to the effective Majorana mass squared, $\langle m_{\beta\beta}\rangle^2$, as shown in equation 1.13.

$$\Gamma^{0\nu\beta\beta} = G_{0\nu}|M^{0\nu\beta\beta}|^2 \langle m_{\beta\beta}\rangle^2 \tag{1.13}$$

where $G_{0\nu}$ is called phase space factor which depends on the Q-value of the reaction, and $M^{0\nu\beta\beta}$ is the nuclear matrix element. The nuclear elements are not very well determined and differ from model to model. By observing neutrinoless double beta decay for different isotopes, the nuclear model can be improved as well.

$$\langle m_{\beta\beta}\rangle = \sum_{k=1}^{3} U_{\nu_e k}^2 \, |m_k\rangle \tag{1.14}$$

The effective Majorana mass can be written in terms of the mass eigenstates, $|m_k\rangle$, (equation 1.14), where $U_{\alpha k}$ is the PMNS matrix. Neutrino oscillation is totally negligible due to the short path lenghts within the detector. The electron flavor neutrinos are the only type of neutrinos which are produced in this reaction. This explains why only the electron flavor neutrino elements are considered in the PMNS matrix in equation 1.14. Equation 1.15 shows the rate of $2\nu\beta\beta$. As seen, the rate is not constrained by the Majorana mass, thus $2\nu\beta\beta$ event is much more probable compared to $0\nu\beta\beta$.

$$\Gamma^{2\nu\beta\beta} = G_{2\nu}|M^{2\nu\beta\beta}|^2 \tag{1.15}$$

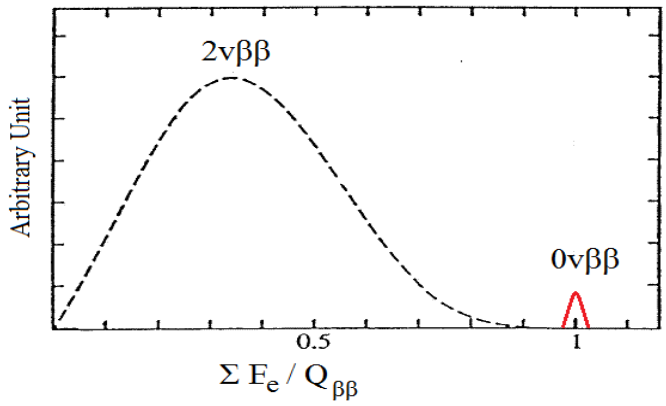

Figure 1.6: A schematic of $2\nu\beta\beta$ signal (dashed black) as well as the $0\nu\beta\beta$ (solid red). The neutrinoless double beta decay peak will be wider due to the imperfect energy resolution of the detector.

Table 1.2 shows some of the isotopes which are candidates for neutrinoless double beta decay experiments, alongside with their natural abundance. In $0\nu\beta\beta$ process all the energy would be transformed to the emitted electrons, thus the corresponding signal ideally would be a sharp peak at the Q-value, right at the end point of the $2\nu\beta\beta$ spectrum, as shown in figure 1.6. The $2\nu\beta\beta$ spectrum can mask the $0\nu\beta\beta$ signal due to the imperfect energy resolution of the detector. Looking for neutrinoless double beta decay requires very high energy resolution and very stringent background limits.

The latest status of the experiments indicate no sign of detection and set new limits on the rate of $0\nu\beta\beta$ and Majorana mass. In 2001, some members of the Heidelberg-Moscow collaboration claimed the detection of $0\nu\beta\beta$ in Germanium-76, with a mass of 0.32 ± 0.03 eV [39]. The results were widely criticized by the other members of the collaboration as well as the physics community. In 2006, the same authors published new results and set a limit on the half-life as 2.3×10^{25}years [40]. The best current limits on $T^{0\nu}_{1/2}$ are set by the EXO-200 and KamLAND-Zen experiments. Using ^{136}Xe as the isotope, EXO-200 measured $T^{0\nu}_{1/2} > 1.6 \times 10^{25}$year (90% C.L.) [41] and KamLAND-Zen published their results in 2013, where the half-life was measured as $T^{0\nu}_{1/2} > 1.9 \times 10^{25}$year (90% C.L.) [42]. Also, the

Isotope	**Q-value [MeV]**	**Abundance [%]**	**Experiment**
^{48}Ca	4.2737	0.187	CANDLES
^{76}Ge	2.0391	7.73	Heidelberg-Moscow, GERDA, Majorana
^{82}Se	2.9955	8.73	SuperNEMO, LUCIFER
^{96}Zr	3.3477	2.8	NEMO-3
^{100}Mo	3.0350	9.82	NEMO-3, MOON
^{110}Pd	2.0040	11.72	-
^{116}Cd	2.8091	7.49	COBRA
^{124}Sn	2.2877	5.79	TIN
^{130}Te	2.5303	34.08	SNO+, COBRA, CUORE
^{136}Xe	2.4578	8.86	EXO, KamLand, XMASS
^{150}Nd	3.3673	5.63	DCBA

Table 1.2: Neutrinoless double beta decay candidates with their corresponding Q-value, natural abundance, and the experiments which have utilized the Isotopes as well as the current experiments.

GERDA collaboration set the best limit on $0\nu\beta\beta$ of ^{76}Ge. They measured $T^{0\nu}_{1/2} > 2.1 \times 10^{25}$ for Germanium [44] which disfavored the controversial claimed value by the Heidelberg-Moscow experiment. Figure 1.7 shows the best current limits on $0\nu\beta\beta$ of ^{136}Xe and ^{76}Ge. Additionally, the shaded gray band shows the predictions for the half-lives for two isotopes based on different nuclear models.

There are several neutrinoless double beta decay experiments which are under construction and will be ready to start taking data eventually. SNO+ is one of the experiments which will search for $0\nu\beta\beta$ of ^{130}Te, using 780 tonnes of organic liquid scintillator as the detection medium. ^{130}Te is a proper candidate for this purpose because of its relatively high natural abundance (see table 1.2), as well as the high optical transparency in the energy region of interest. $2\nu\beta\beta$ of ^{130}Te has been already observed by the NEMO-3 experiment [45]. The CUORE experiment will be also searching for $0\nu\beta\beta$ of ^{130}Te. It uses tellurium dioxide (TeO_2) crystal as both the source of decay and as the medium to detect the signal.

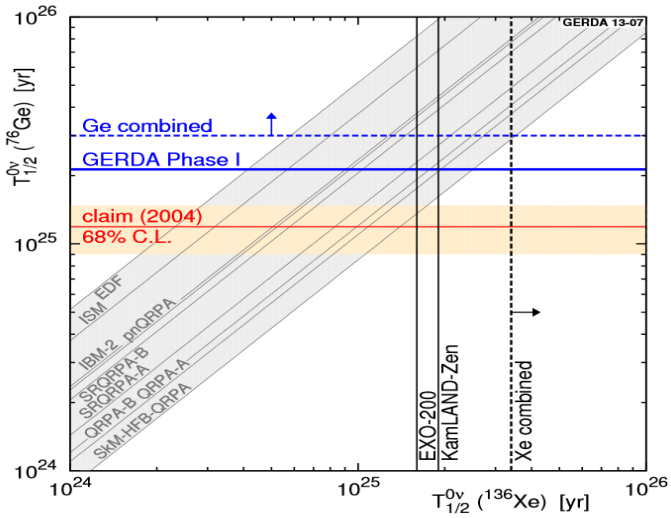

Figure 1.7: Limits (90% C.L.) on $T^{0\nu}_{1/2}$ of ^{76}Ge versus ^{136}Xe. Shaded gray area shows the predictions for the half-lives for two Isotopes based on different nuclear models [44].

1.6 Multipurpose Scintillator-based Experiments

Scintillator is a material which produces light when a charged particle passes through it. Liquid Scintillator is widely used as a detection medium in neutrino experiments as well as other fields. The relatively high light yield of liquid scintillator makes it a perfect target to capture low energy events. In addition, the liquid scintillator has higher level of purity and reasonable price compared to the other target detection media.

Borexino is one of the scintillator-based neutrino experiments. The experiment started taking data in 2007. Borexino was the first experiment that directly measured *pep* neutrinos [46] in 2012. The experiment may also be able to detect neutrinos from supernova within our galaxy. One of the main sources of background in Borexino is coming from cosmogenic muons.

SNO+ and KamLAND are two other multipurpose scintillator-based experiments. They both are able to capture solar neutrinos, reactor- and geo- anti-neutrinos as well as neutrinos from a possible supernova event. Although the highest priority for SNO+ will be searching for neutrinoless double beta decay of ^{130}Te. Kamland-Zen also uses the KamLAND detector to study neutrinoless double beta decay of ^{136}Xe. The advantage of SNO+ over

KamLAND is that the detector is much larger and thus will have a higher rate of events. The KamLAND experiment can not detect the low energy solar neutrinos due to a relatively high rate of the cosmogenic muon background. SNO+ has a very low rate of cosmogenics because of 6000 meter water equivalent ($m.w.e$) of rock shielding, whereas KamLAND only has 2700 $m.w.e$ shielding [47].

Chapter 2: The SNO+ Experiment

"I don't see the logic of rejecting data just because they seem incredible."

— Fred Hoyle

SNO+ is a multipurpose neutrino experiment which is located at SNOLAB, Creighton mine, Sudbury. Most of the hardware has been refurbished from the SNO experiment. SNO+ will use 780 tonnes of organic liquid scintillator called Linear Alkyl Benzene (LAB) as the target material. The primary scientific goal of SNO+ is searching for the elusive process of neutrinoless double beta decay of ^{130}Te. In the initial phase of $0\nu\beta\beta$, the detector will be loaded with 0.3% of natural tellurium, with an expected effective Majorana neutrino mass sensitivity in the range of 55-133 meV [53] which is above the inverted mass hierarchy ($\sim$50meV). In addition to $0\nu\beta\beta$, SNO+ will be detecting low energy solar neutrinos, geo and reactor anti-neutrinos, and neutrinos coming from a possible galactic supernova event. The following sections will describe the SNO+ experiment in more detail. Scientific goals will be discussed as well as the experiment backgrounds. Furthermore, the calibration hardware will be presented.

2.1 The SNO+ Detector

The SNO+ detector reuses most of the hardware from the SNO experiment which was introduced briefly in section 1.3.1.1. The detector consists of a 12m diameter acrylic vessel (AV) which is suspended in a $6263m^3$ chamber, called the SNO Cavity [54]. The AV is supported by 10 pairs of hold up ropes from a platform known as the SNO+ deck. In order to detect the scintillation signal the AV is surrounded by $\sim$ 9500 photomultilier tubes known as PMTs. The PMTs are mounted facing radially inward on a 18m diameter stainless steel structure, known as the PSUP which is held by 15 stainless steel cables from the deck. The volume between the PSUP and the AV will be filled with 1700 tonnes of ultra pure water (UPW). This water shields the detector against the external backgrounds from the PMTs and the PSUP. Furthermore, the cavity volume around the PSUP will hold 5700 tonnes of UPW which shields the detector against the backgrounds from the surrounding rock. Furthermore, 91 outward looking PMTs also monitor the cavity volume which can identify and reject the muon events.

2.1.1 Detector Upgrades

The SNO+ liquid scintillator is composed of Linear Alkyl Benzene (LAB) and Diphenyloxazole (PPO) as a fluor dissolved in a concentration of 2g/l. Liquid scintillator has a much higher light yield compared to the heavy water used in the SNO experiment, thus SNO+ has a lower energy threshold and the detector is sensitive to lower energy events. Furthermore, LAB has high purity levels directly from the manufacturer and long term stability. It has good optical properties such as long scattering length, high transparency and linear response in energy, which makes LAB a perfect target material for SNO+. The detector required upgrades due to utilizing the liquid scintillator. The liquid scintillator has a lower density ($\rho = 0.86\text{g/cm}^3$) than the surrounding UPW, thus about 3×10^5lb of buoyancy force would be exterted on the fully filled up AV. In order to hold the AV and compensate for the buoyancy force hold-down rope system was designed and installed. The hold-down rope system consists of 20 high purity polyethylene fiber (Tensylon) ropes of 38mm diameter [55] and were laid over the AV (figure 2.1b) and anchored to the bottom

of the cavity as shown in figure 2.1a. In addition to the hold-down rope system, the old hold-up rope system has been replaced with the new Tensylon ropes of 20mm diameter in order to reduce the radioactive contamination.

A new purification system was required to be designed to purify the new target material. New purification techniques have been developed to reach a higher level of purification and the scintillator purification plant has been installed in the SNO+ utility room. The target is roughly the same cleanliness requirements **w**hich Borexino and KamLAND have already achieved to and is a purity level of roughly 10^{-17}g/g$_{LAB}$ for both the ^{238}U and ^{238}Th chain in the liquid scintillator [56].

The SNO+ calibration hardware has been designed to match the cleanliness requirements of SNO+. The hardware materials have been investigated to be compatible with LAB. Section 2.4.3 will discuss the SNO+ calibration hardware in more detail.

SNO+ reuses the original SNO PMTs. Faulty PMT bases have been repaired and replaced [57]. The trigger levels for the signals also needed to be set for the new physics goals and the higher light yield of the liquid scintillator. In addition, the electronics, DAQ and the data storage capacity also needed to be upgraded to handle the higher rate of events.

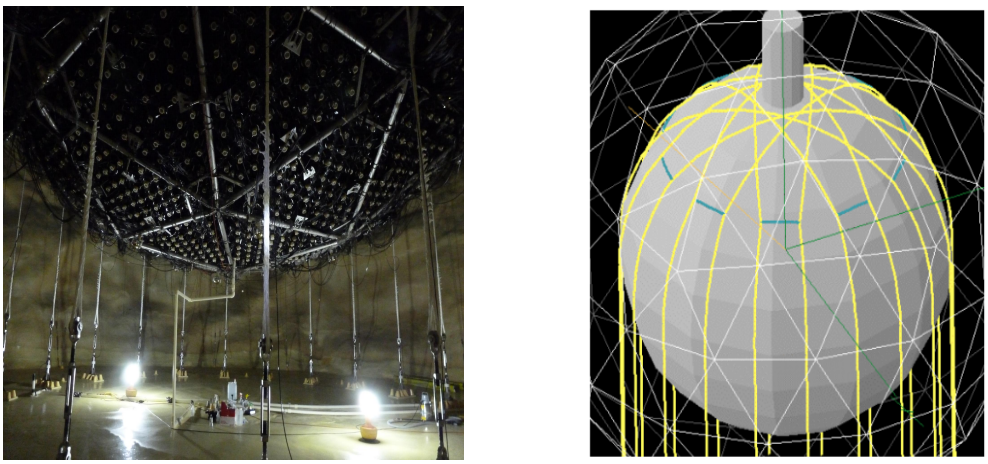

(a) (b)

Figure 2.1: Figure (a) shows the SNO+ cavity and shows 20 hold down ropes anchored to the bottom of the cavity (the figure is taken by the author). Figure (b) Sketch of the hold down rope system on the top of the acrylic vessel to compensate for the buoyant force that the scintillator produces on the AV [55].

2.2 Physics Goals for SNO+

The primary scientific aim for the SNO+ experiment is searching for the process of neutrinoless double beta decay with ^{130}Te loaded into the detector. In addition, SNO+ will be detecting low energy solar neutrinos, geo- and reactor- anti-neutrinos. Neutrinos from a possible galactic supernova event can be detected as well. Also, invisible nucleon decay can be detected during the water phase. The SNO+ run plan can be broken into four phases as follow:

- **Water Phase**

  As the first phase of the experiment, the AV will be filled with ultra pure water. The main goals of this phase include identifying the level of external backgrounds, testing the refurbished electronics, and measuring the PMTs response. The physics goal in this phase will be searching for exotic physics including invisible nucleon decay of ^{16}O and possibly axion-like particles. Furthermore, more physics events can be detected in this phase such as Cherenkov radiations from cosmic muons as well as neutrinos from a galactic supernova and possibly reactor anti-neutrinos. This phase is foreseen for early 2016 and will last for few months.

- **Scintillator Phase I**

  The ultra pure water will be replaced and the detector will be filled with the pure liquid scintillator. The backgrounds can be identified during this phase of the experiment. In addition, the optical model can be verified. Depending on the level of background, low energy solar neutrinos will be observed in this phase, as well as geo and reactor anti-neutrinos. In addition, SNO+ will be able to detect supernova neutrinos in the scintillator phase. This phase is foreseen for 2016 and will last for few months.

- **Tellurium Phase (Scintillator+Tellurium)**

  The main goal is searching for $0\nu\beta\beta$ with ^{130}Te. The AV will be filled with 780 tonnes

of liquid scintillator loaded with ^{130}Te. The initial concentration of ^{130}Te in LAB will be 0.3% with an effective Majorana neutrino mass sensitivity in the range of 55-133meV [58] . Recently, the possibility of loading 10 times more natural tellurium has been investigated, which would enable SNO+ to achieve sensitivity deep into the parameter space for the inverted neutrino mass hierarchy in the future. In addition to $0\nu\beta\beta$, low energy solar neutrinos, supernova neutrinos, geo and reactor anti-neutrinos can be observed in this phase. The tellurium phase is foreseen for 2017 and will last for a couple years.

- **Scintillator Phase II**

  After the $0\nu\beta\beta$ phase, the tellurium will be removed and the liquid scintillator will be purified and returned to the AV. The experiment will be running with the pure liquid scintillator as the target material for detecting low energy solar neutrinos, as well as geo and reactor anti-neutrinos. The detector also will be sensitive to supernova neutrinos.

2.2.1 Neutrinoless Double Beta Decay with SNO+

One of the most important unanswered questions in the field of neutrino physics is whether neutrinos are Dirac or Majorana particles. SNO+ is aiming to answer this question by investigating the neutrinoless double beta decay process with ^{130}Te (Q-value = 2.526MeV). The isotope will be directly loaded into the liquid scintillator volume. Tellurium was selected as the preferred candidate due to high natural abundance of 34% (see table 1.2). This allows loading tonnes of the isotope without enrichment. Furthermore, the other advantage of tellurium is that the Te-loaded liquid scintillator does not have high absorption lines in the region where the PMTs are sensitive (350nm-550nm). Figure 2.2 compares the absorption lines of TeLS with the previously considered candidate, ^{150}Nd. the $2\nu\beta\beta$ signal is one of the main backgrounds for the SNO+ neutrinoless double beta decay phase, due to the imperfect energy resolution of the detector. ^{130}Te has a half-life of 7×10^{20}y [45] which is relatively higher than the other candidates. The long half-life of tellurium will reduce the

$2\nu\beta\beta$ background significantly.

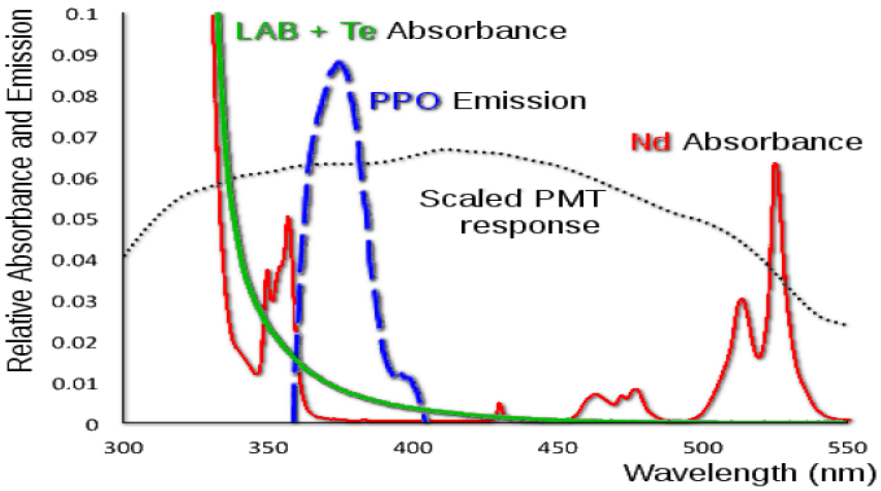

Figure 2.2: Absorption lines of the Te-loaded liquid scintillator compared to Nd-loaded liquid scintillator [59].

Various methods for loading the isotope have been investigated and developed by the collaboration. The initial concentration of 0.3% (800kg) of natural tellurium has been confirmed. With 0.3% tellurium loading into the detector, the expectation is to reach the sensitivity in the range of 55-133meV [53] which is just above the inverted mass hierarchy. Section 2.3 will discuss the backgrounds for the tellurium phase.

2.2.2 Solar Neutrinos with SNO+

The SNO experiment successfully solved the solar neutrino problem by measuring the ^{8}B solar neutrino flux [33]. Flux of the ^{7}Be solar neutrinos has been measured by Borexino [46]. The next step in the field of solar neutrino physics would be measuring CNO, *pp*, and *pep* neutrinos. The final phase SNO+ aims to measure the low energy solar neutrinos with pure liquid scintillator as a target material. The lower energy threshold of liquid scintillator compared to the SNO experiment (3.5 MeV), will allow the detector to measure the *pep* neutrinos. As discussed in chapter 1, the *pep* neutrinos (proton-electron-proton) come from one of initial stages of proton fusion inside the Sun, where it produces ^{2}H and an electron neutrino. They have a single value energy of 1.442MeV (see figure 1.3). Due to their low

flux uncertainty (±1.2%), they are one of the best sources to determine the parameters on the neutrino oscillation. Neutrinos are detected in a scintillator experiment through the "elastic scattering" interaction. Detecting *pep* neutrinos with SNO+ is challenging and requires very stringent background limits (see section 2.3). SNO+ can also measure the flux of CNO solar neutrinos as well as the ^{7}Be neutrinos. Measuring the flux of CNO neutrinos provides us with information about the metallicity of the Sun. In addition, the ^{8}B neutrinos that were measured in the SNO experiment, can be measured in lower energy regions. The backgrounds for solar phase will be discussed in more details in section 2.3.

2.2.3 Geo- and Reactor- Anti-neutrinos with SNO+

A Geo-neutrino is an electron type anti-neutrino which is produced naturally through the β^{-} decay of the radioactive nuclides in the earth's crust and mantel. 99% of the geo-neutrinos originate form the decay chain of ^{40}K, ^{232}Th, and ^{238}U. The SNO+ detector can measure anti-neutrinos through the inverse beta decay interaction. Linear alkyl benzene, as the target material in SNO+, has a large number of protons compared to the heavy water, which makes SNO+ an ideal detector for electron anti-neutrinos. The positron from the event annihilates instantly in the detector and produces scintillation light. Subsequently, 220μs later the neutron captures on hydrogen in the scintillator and emits a 2.2 MeV gamma. The electron anti-neutrino event can be tagged using the delayed coincidence. The generated energy by the positron in this event is equal to the kinetic energy of the positron plus 1.022 MeV which comes from the positron-electron annihilation. SNO+ can detect anti-neutrinos with energy of greater than 1.8 MeV due to the energy threshold of the inverse beta decay. The neutrinos coming from uranium and thorium decay chains can be detected in SNO+. ^{40}K neutrinos cannot be detected due to their lower energy level. Measuring the geo-neutrinos will help to determine the uranium and thorium content of deep inside the earth.

Geo-neutrinos has been measured previously by the KamLAND experiment in 2005 [60], and Borexino in 2010 [61]. One of the advantages of SNO+ over Borexino and KamLAND is the geological region around the experiment. SNO+ is located in the Canadian Shield, also called the Laurentian Plateau which has a higher concentration of radioactive elements

than the one in Japan or Italy. In addition, SNO+ has lower background levels from reactor anti-neutrinos, compared to KamLAND. SNO+ expects 29 geo-neutrino events in one year of data taking [62]. Figure 2.3 shows the expected signal from geo-neutrinos in SNO+.

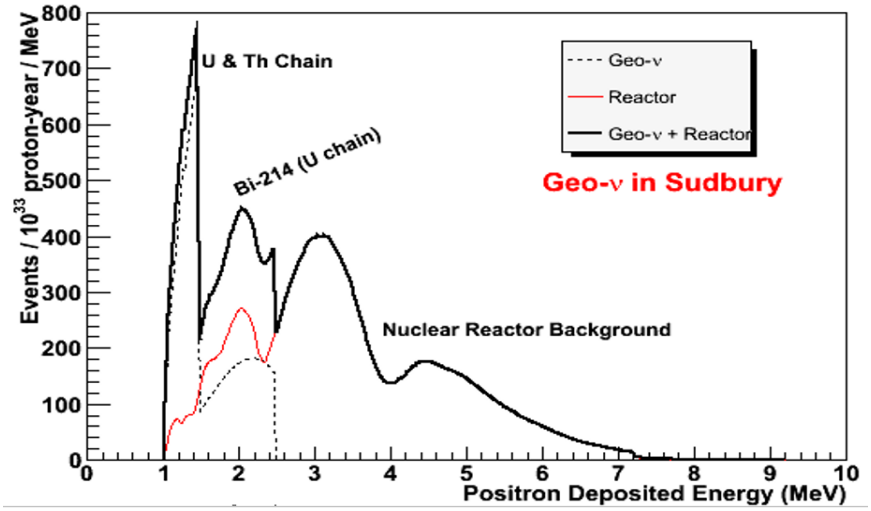

Figure 2.3: The expected signal for geo-neutrinos in SNO+ [63].

Using the inverse beta decay interaction, SNO+ can also measure the reactor anti-neutrinos that come from the beta decay in nuclear power plants. Since the flux of anti-neutrinos from each reactor is well-known, measuring the flux of reactor neutrinos has the potential to make a constraint on Δm^2_{12}. SNOLAB is located near three main reactors with two effective distinct baselines (distance from the power plants). The Bruce nuclear station which is 240km apart form the detector, and the Pickering and Darlington reactors which are located 330km from SNOLAB. The KamLAND experiment has measured the reactor anti-neutrinos previously [47], although SNO+ has the potential to put a new limit on Δm^2_{12}.

2.2.4 Supernova Neutrinos with SNO+

SNO+ can detect neutrinos coming from a possible galactic supernova event. The average energy of supernova neutrinos is about 15 MeV within a few second time interval. The electron type supernova neutrinos can be detected through charged current interactions in the detector. Additionally, every flavor neutrinos can be detected via neutral currents

interactions on ^{12}C and the proton. The experiment expects to record more than 100 events for a $10^{53} erg$ supernova event at 10kpc [64]. SNO+ also participates in the inter-experiment Supernova Early Warning System (SNEWS), which aims to provide a fast alert using the coincidence observation of burst signals in several detectors [65].

2.3 Backgrounds in SNO+

Generally any detectable event that can fall in the energy region of interest and mask the signal is considered to be a background event in the experiment. Searching for rare events requires very stringent background limits in the energy region of interest. Radioisotopes are one of the main sources of background in SNO+. The radioactive background can be classified into two general categories, internal and external. Internal backgrounds are produced within the detector volume (e.g. radioactive contamination in LAB or tellurium). External backgrounds are produced in the regions outside the detector volume but propagate into it, such as radioactive contamination in the ropes, PSUP, and UPW. The main portion of radioactive background originates from the decay chains of Uranium (^{238}U) and Thorium (^{232}Th). They both are naturally occurring radioisotopes, with the half life of 4.47×10^9 years for ^{238}U, and 1.4×10^{10} years for ^{232}Th. The uranium and thorium decay chains are shown in figures 2.4a and 2.4b, as well as the half-lives and the Q-values. Very low concentration of uranium or thorium can emit many alphas and betas which generate scintillation light in the detector. The goal is reaching the purity level of about 10^{-17}g/g$_{LAB}$ for both the uranium and thorium chain in the liquid scintillator. This is the same cleanliness level achieved by the Borexino experiment [56]. In order to reach that level of purification, LAB will be purified through distillation, water extraction, nitrogen and steam stripping, and going through metal scavenger adsorption columns [66]. The scintillator purification system has been designed and is being installed underground in the SNO+ utility room. The UPW

purification system has also been upgraded. In addition to removing the radioactive backgrounds, tagging the events according to their characteristics is a technique to constrain the background. Cosmogenic muons are also another source of backgrounds in a scintillator based experiment. SNO+ has a very low rate of cosmogenic muons due to the $\sim$ 6000 m.w.e shielding from the overburden rock, which leads to a rate of 3 muons passing through the detector per hour.

The $2\nu\beta\beta$ signal is an inevitable background for the search for neutrinoless double beta decay, due to the imperfect energy resolution of the detector. Tellurium has a relatively long double beta decay half-life $\sim 7 \times 10^{20}$y, which reduces this background signal. The main backgrounds for tellurium phase include ^{208}Tl, ^{212}Bi, Pile-up ^{212}Po and excited ^{208}Pb* ($\gamma \sim 2.614$ MeV), from the thorium chain, and ^{214}Bi and ^{214}Po from the uranium chain [58]. The radioactive backgrounds can be identified and reduced by tagging techniques (e.g. α-β time coincidence). The external background mainly comes form the acrylic vessel, PSUP and shielding water. The external background will be reduced by limiting the fiducial volume of the detector to a 3.5 m fiducial radius cut, which preserves 20% of signal events. Also, ^{8}B solar neutrinos can undergo the elastic scattering inside the detector and generate scintillation lights, which is one of the backgrounds for the tellurium phase. The previous measurements of ^{8}B solar neutrinos flux by the SNO collaboration, can also help to identify and reduce the ^{8}B background. One of the most important sources of background in SNO+ comes from the radon daughters. ^{222}Rn is a radioactive noble gas which is occurring in the ^{238}U decay chain as shown in figure 2.4a. The radon level in the lab air has been measured as 131.0$\pm$6.7 Bq/m^3 [68]. During the transition from SNO to SNO+ the AV has been exposed to the lab air and as a result the radon has diffused into the surface of the acrylic vessel. Radon decays to ^{210}Pb which has a relatively long half-life (22 years) and subsequently decays by beta emission to ^{210}Bi, and ^{210}Po. Radon daughters can leach from the inner surface of the acrylic into the detector volume and increase the background. SNO+ is concerned with the leaching rate of radon daughters. Chapter 3 describes the leaching model and presents the leaching calculations which were done by the author. ^{210}Bi is the main radioactive background for the solar phase, specifically CNO neutrinos. ^{210}Bi decays through beta emission with a Q-value of 1.16 MeV. Figure 2.6 shows the expected energy

spectrum for the solar phase, assuming that the Borexino level of backgrounds are reached in SNO+. Furthermore, ^{210}Po decays to ^{206}Pb through the alpha emission. Subsequently, the produced alpha may undergo a reaction with a ^{13}C nucleus in the liquid scintillator and produced neutrons. The neutrons thermalize within a few microseconds and can be captured by the carbon atoms, which emits 2.223 MeV gamma. This process is known as $^{13}C(\alpha, n)$ reaction and can fall in the energy region of interest for the $0\nu\beta\beta$ search and contributes to the background. Figure 2.5 shows the expected energy spectrum from a 0.3% Te-loading and two years of data taking with a fiducial volume cut of 20%. The effective Majorana mass has been assumed as 200 meV [69][70].

2.4 Calibration

Without comprehensive calibrations, the observed data from the experiment are very hard to interpret. What can be observed in an event in SNO+ is the charge and the time of each PMT hit. Various types of calibration are required to link the PMT measurements of the time and charge to a description of the initial event in terms of the energy, position and nature of the interaction. A combination of Monte Carlo simulations and comprehensive calibrations enable us to reconstruct the events and interpret the raw data and identify the interaction. Four main categories of calibration are required to fully understand the SNO+ detector: energy calibration (PMT parameters), electronics, optical calibrations, and the geometrical parameters for the detector. PMT parameters mainly include the light collection efficiency for PMTs and cable timing delays. Electronics are verified with every calibration, since it consists of the observable parameters, such as voltage of PMTs and background noise in the circuits. SNO+ is basically a complicated light measuring device including different mediums in terms of optical properties. The optical calibration aims to identify the optical characteristics of the detector such as attenuation length and light

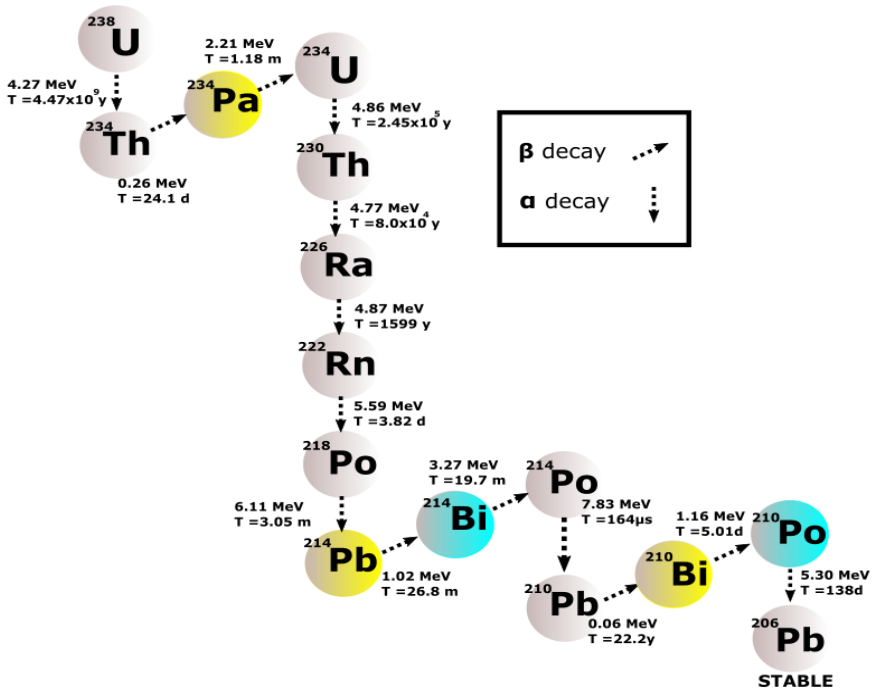

(a)

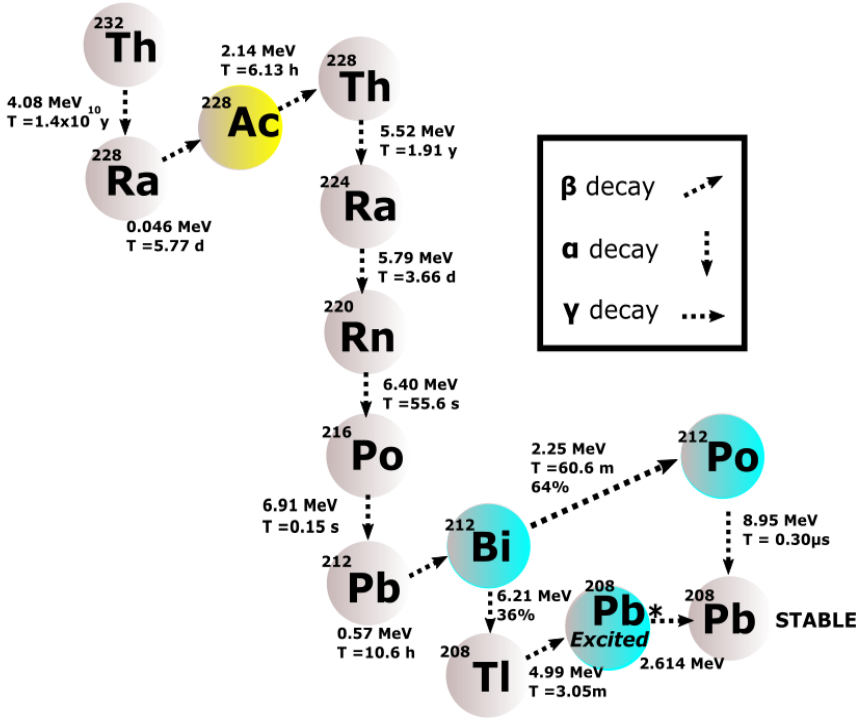

(b)

Figure 2.4: Figure (a) shows the decay chain for ^{238}U and figure (b) shows the decay chain of ^{232}Th. The background isotopes for $0\nu\beta\beta$ search are highlighted in blue and the background for the solar neutrinos are highlighted in yellow.

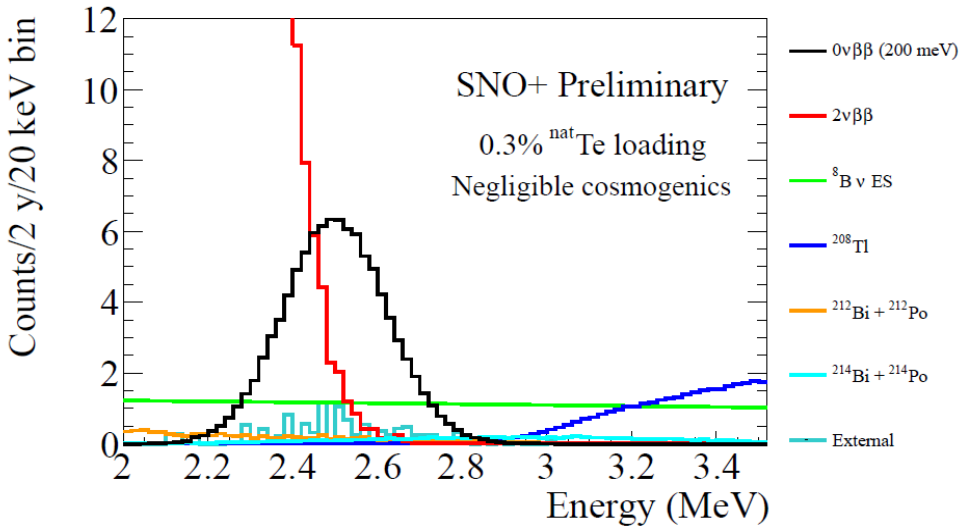

Figure 2.5: Expected energy spectrum for the SNO+ $0\nu\beta\beta$ search. The spectrum is obtained for 2 years of running, a fiducial volume cut at 3.5 m radius, and 0.3% Te-loading into the liquid scintillator. The effective Majorana mass is assumed to be 200 meV [21][22].

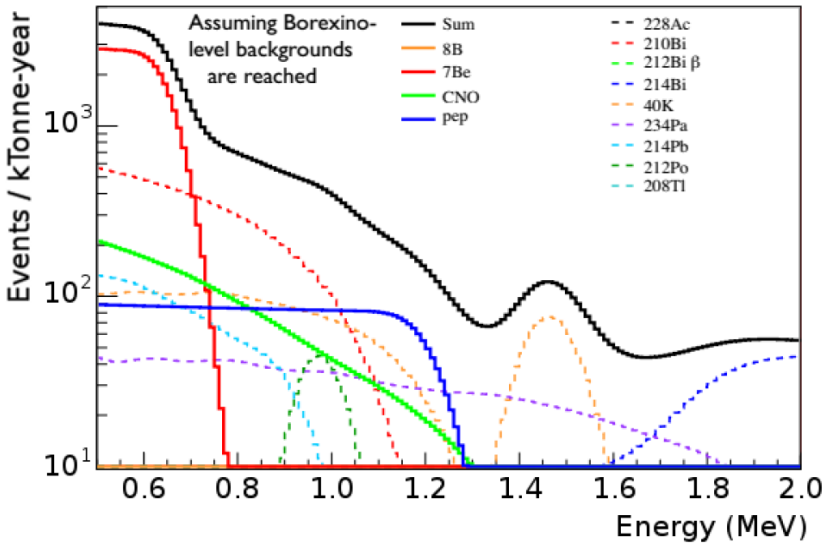

Figure 2.6: Expected energy spectrum and background for the SNO+ solar phase [23].

scattering. Furthermore, in order to reconstruct the events it is necessary to monitor the position of the detector relatively with respect to PSUP and the other components, since the AV is suspended through the rope system and can be displaced relative to the PSUP. This section will briefly outline the various calibration systems and focus on the required

infrastructure and the hardware.

2.4.1 Calibration Sources

Several calibration sources, with various energies, have been investigated to be utilized in the SNO+ liquid scintillator. Different sources are required to characterize the PMTs' response to different particles such as βs, γs and neutrons. Furthermore, these sources help to calibrate the electronics and PMT parameters as well as energy reconstruction and optical calibrations. Some of the sources have been developed in order to tag their signal. A small PMT was installed inside the source. Comparing the timing of the source PMT with the detector PMTs, the source can be identified and tagged. In addition, an α-β coincidence tagging technique can be applies to some of the sources. Tagging the calibration sources also enables us to subtract the background events and provides a clean calibration data sample. Furthermore, it helps us to identify the backgrounds in the detector. Table 2.1 shows the calibration sources for SNO+. The time stability of the detector is one of the concerns that can be inspected by deploying the same source repeatedly during the operating time of the detector. Using the calibration hardware, all of the described sources will be deployed into the AV. Although, deploying the calibration sources is not the only task for the calibration hardware. It has many components which will be described in the following sections.

2.4.2 Optical Calibration

The laser-ball is a specialized optical calibration source. This tool is inherited from the SNO experiment and has been upgraded to be compatible with the liquid scintillator in SNO+. The main purpose of the laser-ball is understanding the optical properties of the detector such as absorption and scattering as well as timing parameters for PMTs. The laser-ball consists of a 109 mm diameter light diffusing quartz flask illuminated through optical fibers. The optical fibers are carried from the deck to the source through the laser-ball umbilical which is shown in figure 2.8. The laser-ball system can excite five different laser dyes at

Source	Energy	Particles Emitted	Tagged?
AmBe	4.4	γ, n	Coincidence
^{16}N	6.1	γ	Yes
^{24}Na	4.12	2γ: 1.37, 2.75 MeV	Yes
^{48}Sc	3.33	3γ: 0.98, 1.04, 1.31 MeV	No
^{57}Co	0.136	γ: 0.122 MeV	No
^{60}Co	2.5	2γ: 1.17, 1.33 MeV	Yes
^{90}Y	2.28	β	No
Laser ball	Various	γ	No

Table 2.1: Calibration sources for SNO+. The second column shows the total energy of the event [71].

wavelengths ranging from 380 nm to 490 nm [59].

In addition, SNO+ has another optical calibration tool, called the External LED/Laser Light Injection Entity (ELLIE) system. This system consists of light injection fibers which have been installed outside of the detector on the PSUP, as shown in figure 2.7. One of the benefits of this system over the laser-ball is that the optical properties of the detector can be monitored without introducing any background into the liquid scintillator. The laser/LED system is located on the deck on top of the detector and through optical fibers, it is connected to the 91 positions on the PSUP.

2.4.3 Calibration Hardware

Most of the calibration hardware systems in SNO+ have been adapted from the SNO experiment such as the Umbilical, the Umbilical Retrieval Mechanism (URM), the Universal Interface (UI), Source Storage Box (SSB), Source Connection Devices (SCD), and the Neck Sense Rope System (NSRS). The materials have been investigated and upgraded to be compatible with liquid scintillator and the scientific goals of the experiment. Figure 2.8 shows the SNO+ detector with some of the calibration hardware components. The next sections will describe some of the components in more detail.

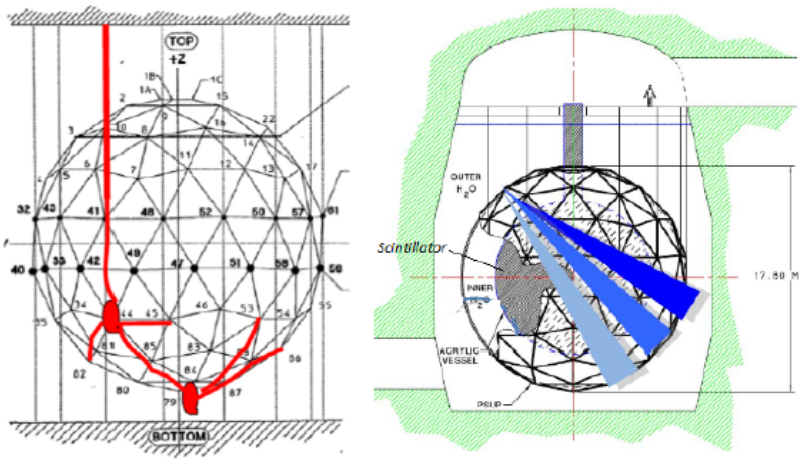

Figure 2.7: a) shows ELLIE system. b) Example of one of SMELLIE nodes with beams in three directions [72].

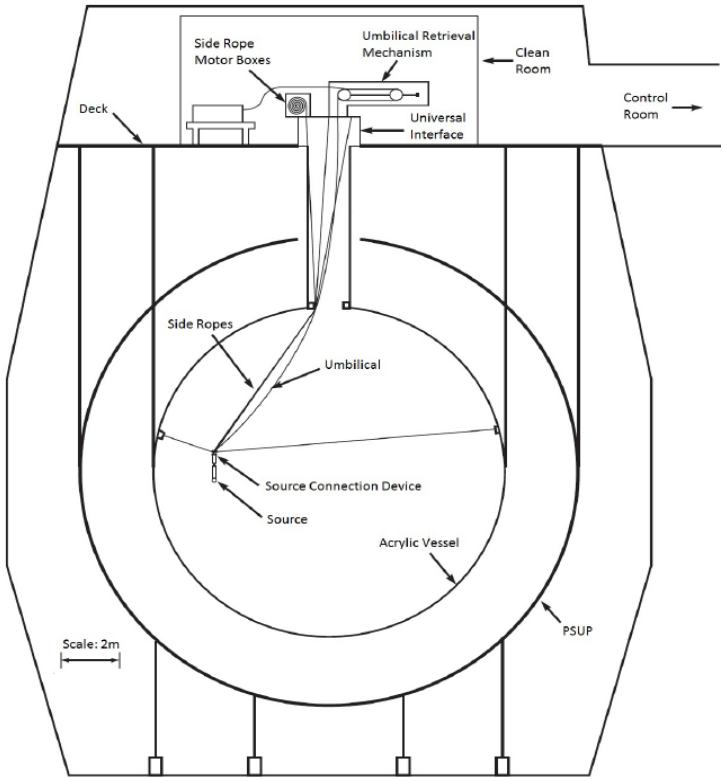

Figure 2.8: The SNO+ detector and calibration source deployment system [73].

2.4.3.1 Umbilical

The umbilical system has been developed to deploy and place the calibration sources into the liquid scintillator inside the acrylic vessel. It consists of the umbilical central rope, the

umbilical retrieval mechanism (URM), the calibration side ropes, the manipulation system, and the motor box (see figure 2.8). The position of calibration sources must be known to reconstruct the event based on the timing of PMT hits. Using the central umbilical rope, the source can be displaced along the vertical axis and the side ropes manipulate the horizontal position of the source. The combination of the central rope and side ropes allows the source to be positioned in two dimensions in the scintillator within 5cm accuracy. The URM is located on the SNO+ deck and controls the movement of the central rope which holds the weight of the source. It contains a set of pulleys, electrical components and the gas connections for different sources. In addition, 4 motor boxes will be located on top of the upper UI, and control the movement of the side ropes. A new URM is being designed for the scintillator phase. Due to the background requirements of SNO+, the entire URM will be sealed to prevent radon ingress. Physical properties of the system such as the friction of the pulleys and the operational tension of the system have been measured. Additionally, all the materials have been tested to ensure the compatibility with the liquid scintillator as well as measuring the radioactive contaminants.

2.4.3.2 Universal Interface

Generally speaking, the inside of the AV can be accessed through the universal interface (UI) structure. The UI is made out of stainless steel and sits on top of the chimney in the Deck Clean Room (DCR). It consists of two different parts, known as the lower UI and the upper UI which are shown in figure 2.9. The lower UI is attached to the top of the neck and sealed through a double o-ring. A number of pipes used to transfer the liquid in and out of the AV are attached to the lower UI. In addition, the outer bottom edge of the lower UI houses three attachment blocks used to attach the neck positioning sense ropes as shown in figure 2.12a. The sense rope system is a mechanical system was to monitor displacement of the AV. Chapter 4 will be dedicated to the SNO+ sense rope system.

The sliding floor is installed around the lower UI. The sliding floor is a 102.5" diameter movable platform which has been installed around the lower UI as shown in the figure 2.10a and figure 2.9. The sliding floor can be used as a solid working platform around the UI.

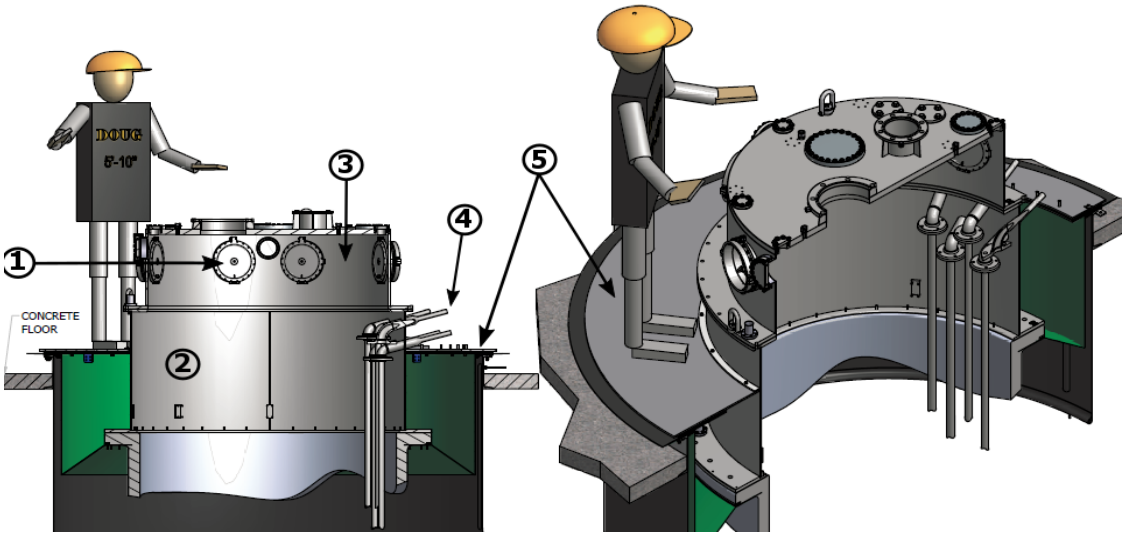

Figure 2.9: Figure is taken from [75] and shows the following parts: 1) Glove ports. 2) The lower UI. 3) The upper UI. 4)The pipes that transfer the liquid in and out of the AV. 5) The Sliding floor.

Additionally it provides a light barrier around the AV neck. Since it is a movable platform it allows the AV to displace 6" horizontally, 8" downward, and 2" upward, during the experiment [74]. Furthermore it protects the pipes and prevents any possible leak from the AV neck. There is also a fixed plate which is located underneath the sliding floor, shown in figure 2.10b. Seven square (2"×2") vertical plates are attached to the underside of the fixed plate [75]. These plates are used to mount the sense rope boxes, known as sense rope snouts, to the fixed plate.

The upper UI sits on top of the lower UI, see figure 2.9. There are three size of gate valves on top of the upper UI, 6" diameter, 8" diameter, and 10" diameter, where different calibration sources can be deployed into the AV through the URM. For each gate valve on the upper UI there is a corresponding gate valve on the URM as well as source storage box. Also there is a sensor on each gate valve to see whether the gate valve is open. Furthermore, there are four pairs of glove ports around the upper UI, as it is shown in figure 2.9, which allow a user to access to the inner volume of the UI. The upper UI houses 4 downward PMTs, known as neck PMTs. The neck PMTs can detect events taking place inside the neck volume. The side rope manipulators also sit on top of the upper UI.

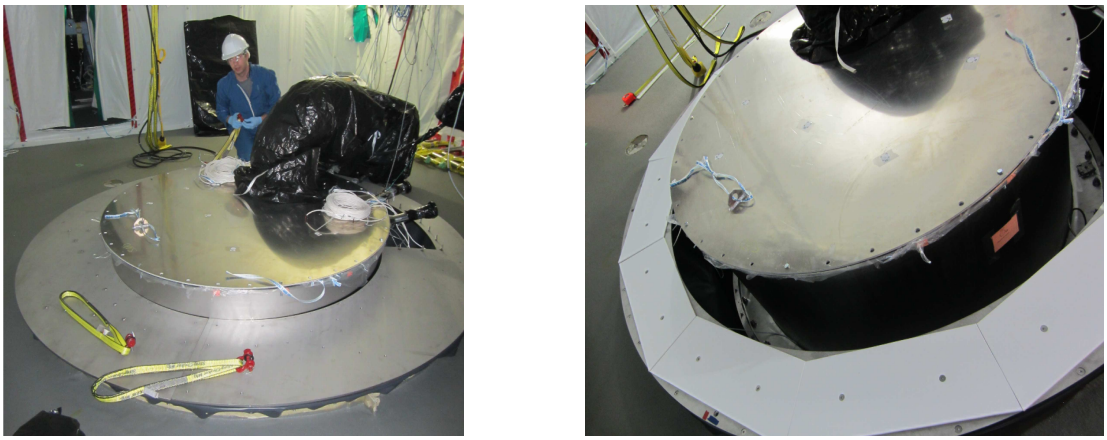

(a) (b)

Figure 2.10: Figure (a): The lower UI surrounded by the sliding floor plus the black ventilation pipe attached to the lower UI. Figure (b) shows the fixed plate, known as sensor attachment plate which is located underneath the sliding floor.

Additionally, a source storage box is being designed to keep the calibration source in a low radon environment, away from laboratory air. There are three sizes of gate valves on top of the storage box, which allow a clean transition of the source to the URM. The storage box has two pairs of glove ports which allow a user to manipulate the source in a clean environment. A quick connecting system has been also developed to transfer the source to the URM.

2.4.3.3 Cover Gas System

The radon level at SNOLAB is about 6×10^7atoms/m^3 ($\sim$130 Bq/m^3) [68]. As mentioned previously, radon daughters are direct backgrounds for SNO+, thus the detector must be sealed against the radon in the laboratory air. This was accomplished in the SNO experiment by replacing the air volume with boil-off N_2 from a liquid nitrogen dewar [76]. Since the old system does not meet the background constraints for SNO+, a new system have been designed for the experiment, known as the cover gas system. This system consists of three flexible bags (3$\times$240 L), fail-safe pressure relief device (U-tube system) and electropolished stainless steel tubing. The new cover gas system will use N_2, which is one of the best candidates for this purpose. The boil-off nitrogen gas has a very low radon contamination due to the lower boiling temperature of liquid nitrogen (-196 °C) compared to the boiling

temperature of liquid radon (-62°C). Thus, it is easy to provide ultra pure boil-off nitrogen. The pressure of laboratory air fluctuates regularly. The pressure changes due to ventilation can be very rapid, with changes up to 0.5 psi within a 10 minute period [54]. The rapid pressure fluctuations can make a huge pressure difference between inside and outside the AV and damage the detector. The cover gas system balances out the pressure changes between the lab environment and inside the AV. The three flexible bags provide additional reservoir and let the AV to breath the low background nitrogen.

The cover gas system cannot be attached till the detector is almost full. In order to stabilize the pressure when the detector is empty, an orifice has been set on the upper UI which enables the AV to breath the laboratory air. The proper size of the hole has been calculated according to the pressure fluctuations in the lab. The calculations were done by the author and are described in the appendix A.

2.4.3.4 Cameras

In order to reconstruct an event, it is imperative to know the position of the AV and the calibration source within the detector. By measuring the length of the calibration ropes from the source manipulator system, the position of the source can be determined to within 5cm [77]. This system is not very accurate and suffers higher uncertainty when the source is away from the center of the detector. A camera system was proposed and designed to monitor the geometry of the detector with higher accuracy. This system consists of 6 underwater cameras symmetrically mounted inward looking on the PSUP, as shown in figure 2.11b. The system monitors the physical state of the detector, including the position of the rope net and any displacement of the AV with respect to the PSUP. The system also will be able to triangulate the position of the calibration source to accuracy of 1.5 cm at a distance of 9 meter. Figure 2.11a shows camera number 1 installed among the PMTs.

2.4.3.5 Neck Sense Rope System

The Neck Sense Rope System (NSRS) is a mechanical system that monitors displacement of the vessel chimney within accuracy of 2 mm, with respect to the deck. It consists of seven

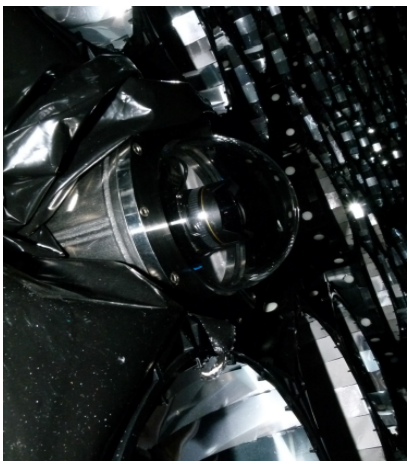

(a)

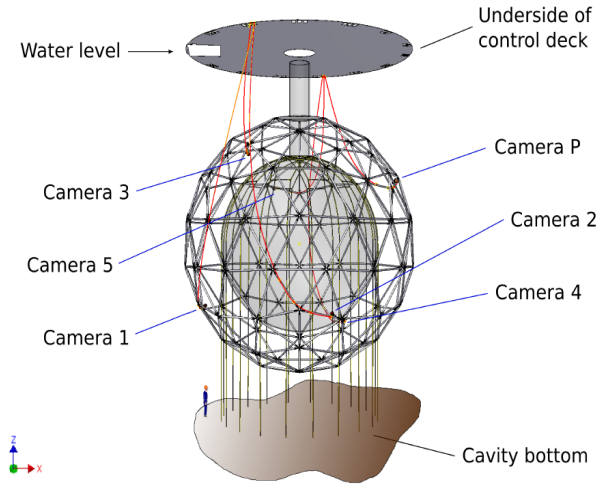

(b) .

Figure 2.11: (a): Camera number 1 installed on the PSUP among the PMTs. (b): The camera system. Figure is taken from [77].

independent sense ropes which enables the system to notice any translation (Δx, Δy, Δz) as well as a possible rotation ($\Delta\phi$, $\Delta\theta$, $\Delta\psi$). The sense ropes are attached to the bottom edge of the lower UI through three sense rope attachment blocks as shown in figure 2.12a. At the other end, the ropes are connected to the fixed sense rope boxes, known as sense rope snouts. Each sense rope snout contains a retraction mechanism, a brass drum and a precise potentiometer (see figure 2.12b) which enables the displacement (length) measurements. Using a simple circuit, the potentiometers are connected to the DeltaV® system. DeltaV consists of an Analog to Digital Converter (ADC) and provides a user interface to read the measurements in terms of electrical currents. The circuit keeps the current within the suitable range for the use of DeltaV (4-20mA).

Treating the AV as a rigid body, the sense rope system, the equator positioning system and the cameras together can provide a real-time position monitoring of the detector. Real-time monitoring of the neck displacements during operation, can ensure that either the neck or the vessel would not hit any of the surrounding structures. Additionally, it can provide us with some valuable information about the time dependent geometrical properties of the AV such as deformation.

(a)

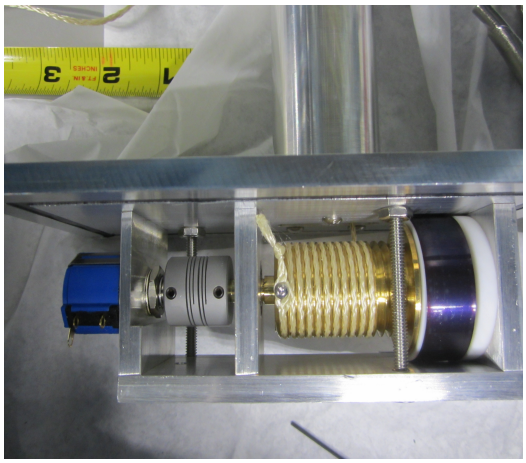

(b)

Figure 2.12: Figure (a): 3 sense ropes are attached to the attachment block number one which is mounted at the bottom edge of the lower UI. Figure (b): One of the sense snouts consists of a brass drum, a potentiometer, and a spring to keep the rope retracted.

In order to achieve the 2mm accuracy, the system must be calibrated precisely. In addition to the calibration, a survey is necessary to identify the relative geometry of the components. The accuracy of the electrical circuit and the stability of the DeltaV readings have been studied as well. The system has been calibrated and installed in fall 2014 alongside with the sliding floor installation. The author has been actively involved in the calibration and installation of the sense rope system. Chapter 4 will discuss the system in more detail and discuss the calibration and installation steps.

Chapter 3: Leachig Studies

3.1 Introduction

Surface contamination of radioactive isotopes is one of the sources of background in the scintillation-based experiments (e.g. Borexino, SNO+). It is primarily a problem since radioactive contaminants can be transferred into the high purity liquid scintillator and increase the internal backgrounds. As a result, there are strict limits on the surface cleanliness of all detector components that come into contact with the scintillator. ^{222}Rn is one of the main sources of radioactive surface contamination in the lab. Radon is a radioactive noble gas, occurring naturally as a decay product of ^{238}U. There is a significant concentration of uranium in soil and rocks, as a result there is a high level of radon gas in the laboratory air. The radon level at SNOLAB has been measured as 131.0 ± 6.7 Bq/m^3 through radon assay [78]. While transitioning from the SNO experiment to SNO+, the acrylic vessel has been empty and exposed to air for years, and as a result some level of radon has penetrated into the acrylic. ^{222}Rn decays to ^{210}Pb which has a relatively long half-life (22 years) and subsequently decays by beta emission to ^{210}Bi, and ^{210}Po. Radon daughters can leach into the detector volume (as shown in figure 3.1) and increase the level of internal background. ^{210}Bi is a direct background for measuring *pep* and CNO solar neutrinos, due to its end point energy of 1.16 MeV. Additionally, ^{210}Po is the main source of high energetic alphas ($E_\alpha = 5.3$ MeV) in SNO+. The decay process is a pure alpha emission in 99.998% of the cases. The energetic alpha interacts with ^{13}C nuclei and produce free neutrons in the liquid scintillator, see equation 3 .1. The free neutrons will thermalize in the detector and get

captured by the protons or carbon atoms. The neutron capture on a proton emits a 2.223 MeV gamma which can fall in the energy region of interest for neutrinoless double beta decay search [79].

$$\alpha + {}^{13}\mathrm{C} \longrightarrow \mathrm{n} + {}^{16}\mathrm{O} \qquad (3.1)$$

This interaction is denoted by ${}^{13}\mathrm{C}(\alpha, n){}^{16}\mathrm{O}$ and it was also identified and studied by the KamLAND experiment as a background [80].

Leaching kinetics highly depends on factors such as temperature, nature of contaminants, leaching medium and the initial conditions. Several bench-top measurements were performed at Laurentian University on the leaching rate of ${}^{210}\mathrm{Pb}$ and ${}^{210}\mathrm{Po}$ into different media for different temperatures [86]. Based on physics of mass transfer and diffusion, a temperature dependent model has been developed by the author. This tool can be used to fit the data and estimate the expected background rate from the leaching of radon daughters into the SNO+ detector.

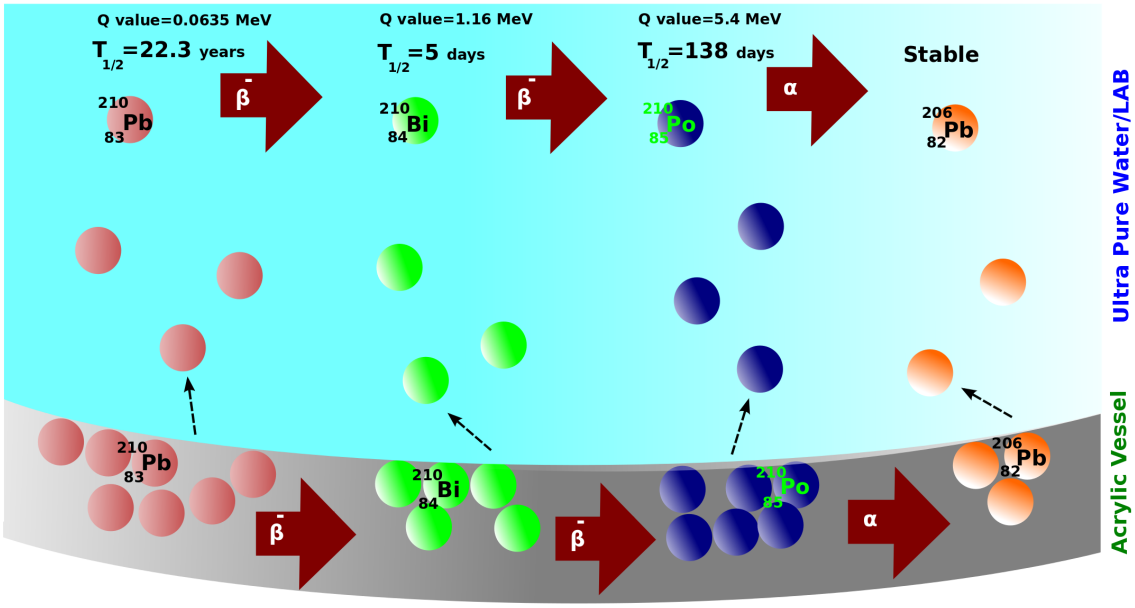

Figure 3.1: Leaching of ${}^{222}\mathrm{Rn}$ daughters into the detector volume, as well as decaying by beta emission. Diffusion of ${}^{222}\mathrm{Rn}$ or radon progeny (airborne particles) into the liquid is another source of radon daughters in the detector. However, this figure dismisses the ${}^{222}\mathrm{Rn}$ diffusion.

Between January 27th, 2015, 12:00PM (EST) and January 28th, 12:00AM (EST), an underground water assay was performed on the water which has been contained in the AV for almost 4 months. Using a high efficiency gamma counter the specific activity of ^{210}Pb in the water has been measured as 0.26 ± 0.04 Bq/m^3 [81]. The water assay provided an opportunity to test the leaching model. The leaching model was applied to estimate the amount of ^{210}Pb in the water. The total specific activity of ^{210}Pb in the water has been estimated through the leaching model as $0.169^{+0.085}_{-0.073}$ Bq/m^3 which is compatible with the measured value to within 1 sigma. The following sections will provide a summary of the physics of desorption and discuss the leaching model. We will also discuss some of the possible cases for leaching. Finally, the water assay will be described and the calculated results will be compared with the measured value.

3.2 Physics of Desorption

Desorption or leaching is a phenomenon whereby an adsorbed layer of atoms or molecules is released from or through a surface. Desorption occurs when phonons in the material break the surface bonds of the adsorbed material. External stimulus such as an incident photon or electron can also contribute to the rate of desorption. The rate is generally a function of the substrate, adsorbed species, contact fluid, and temperature. The leaching rate can be expressed as equation 3.1 [82].

$$\frac{dN}{dt} = -k(T)N^x \tag{3.1}$$

where N is the surface concentration, $k(T)$ is the rate constant for leaching, and x indicates the order of desorption. The kinetic order of desorption depends on the nature of adsorbed material and the number of elementary steps involved. It can be a zero-, first- or second-order process. Atomic or simple molecular leaching is typically a first-order process ($x = 1$). The desorption process is relatively simple in the case of SNO+ due to the extremely low level of impurities in the liquid scintillator. Several bench-top measurements have been

performed to determine the leaching rate of ^{222}Rn daughters into different media. 3.3 will discuss the leaching measurements for SNO+ in more detail. The measurements confirmed the first order leaching process for SNO+ [85]. Furthermore, Borexino has investigated a similar type of leaching and indicated the first order process as well [83].

The leaching constant or relative leaching rate, k, has a temperature dependency, which is given by Arrhenius equation (3.2).

$$k(T) = Ae^{\frac{-E_a}{RT}} \tag{3.2}$$

where R is the gas constant, and A is called the attempt frequency which depends on the adsorbed material and the medium. E_a is the activation energy, the minimum required energy for one molecule or atom to overcome all the surface barriers and be released from the surface. Concentration of the adsorbed contaminants has no effect on the activation energy of the process. For a first-order desorption the activation energy is about $\sim$1 eV/atom due to the energy level of molecular bonds [82]. The Arrhenius equation is a direct result of collision theory, where the probability of number of collisions with the energy greater than E_a is proportional to $e^{\frac{-E_a}{RT}}$.

Furthermore, the leaching constant can also be determined in terms of D, the diffusion coefficient of the material from acrylic into the medium, see equation 3.3.

$$k(T) = \frac{\pi^2 D(T)}{4L^2} \tag{3.3}$$

where L is the thickness of the layer of adsorbed material and the diffusion coefficient depends on temperature through the following expression [84] (equation 3.4).

$$D(T) = D_\circ e^{\frac{-E_a}{RT}} \tag{3.4}$$

3.3 Leaching Rate Measurements in SNO+

The leaching rate of radon daughters can be estimated by measuring the activity of ^{210}Po and ^{210}Pb in the leachate. The concentration of ^{210}Po can be measured by alpha counting the sample, where $E_\alpha = 5.3$ MeV. In addition, using a high efficiency gamma counter the activity of ^{210}Pb can be determined through measuring the 46.5 KeV peak through the ^{210}Pb spectrum.

The SNO+ collaboration used two different methods to measure the leaching rate of ^{222}Rn daughters; *in-situ* measurement of the leaching and leaching measurements from spiked acrylic [85]. In 2012, the *in-situ* measurement or the direct measurement of the leaching was proposed. Initially the bottom of the acrylic vessel was cleaned using Alconox® and UPW. The initial activity of the adsorbed material in the acrylic was measured using two 20 cm^2 silicon alpha counters. The activity of the implanted ^{210}Po on the bottom of the AV has been measured as 1.9 ± 0.2 Bq/m^2. The AV was filled with 12 L UPW from the SNO water plant. After five days of leaching, the water was collected and alpha- and gamma-counting were performed to determine the activity of ^{210}Pb and ^{210}Po. The activity of ^{210}Pb in the water has been measured as 16.9 mBq. In order to determine the background contamination in the leaching sample, a gamma counting was performed on a 8 l5 iter blank sample from the SNO water plant. The activity was measured as ∼1 mBq. The gamma spectrum of the leached ^{210}Pb in the water and the background spectrum are shown in figures 3.2b and 3.2a respectively. Assuming that ^{210}Pb is in an equilibrium with ^{210}Po, the leaching constant can be estimated through equation 3.5.

$$k(T) = \frac{A_w(lead)}{S \times \tau \times A_{int}[\mathrm{Bq/m^2}]} \qquad T = 25^\circ C \tag{3.5}$$

where $A_w(lead)$ is the total activity of ^{210}Pb in the water, S is the area of the acrylic under the water (∼0.88 m^2), τ is the leaching time (5 days), and A_{int} is the specific activity of the ^{210}Pb on the acrylic (1.9 ± 0.2 Bq/m^2). The leaching rate at 25°C has been estimated as $(2.0 \pm 0.3) \times 10^{-3}$ $[day^{-1}]$.

The second method to estimate the leaching rate of radon daughters was based on the

Figure 3.2

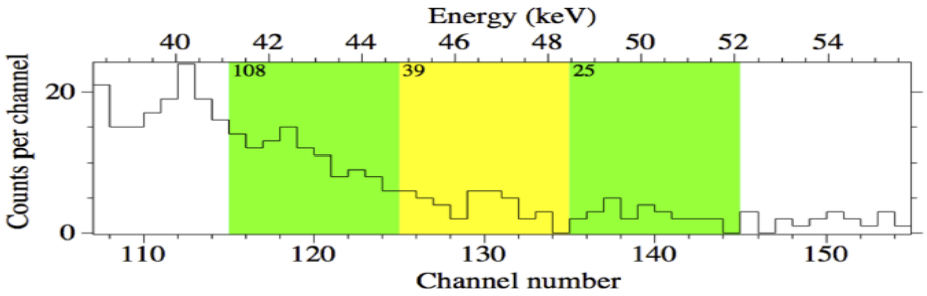

(a) Spectrum of the blank sample of 8L UPW from the SNO water plant. $T_{live} = 3.79$day

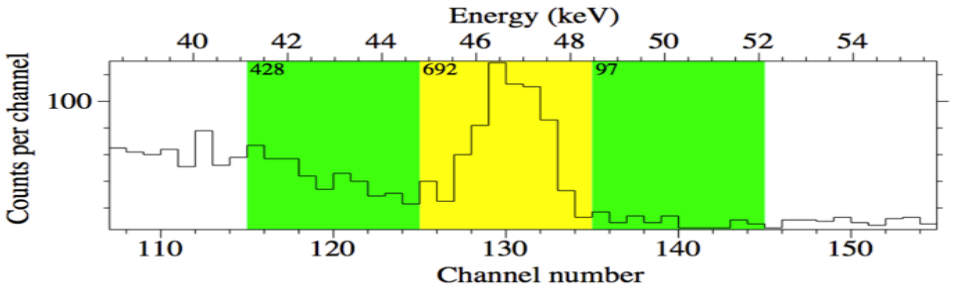

(b) Spectrum of water which has been contained in the AV for 5 days. ^{210}Pb peak area (yellow) consists of 530 ± 31 counts using high efficiency gamma counter. Figures are taken from [85].

bench-top activity measurements of the spiked acrylic samples [85]. Two similar samples of acrylic have been exposed to high intensity radon gas for 12 days. The samples have the same origin as AV and size of 7×7cm^2 and 5mm thickness (see figure 3.3). The radon

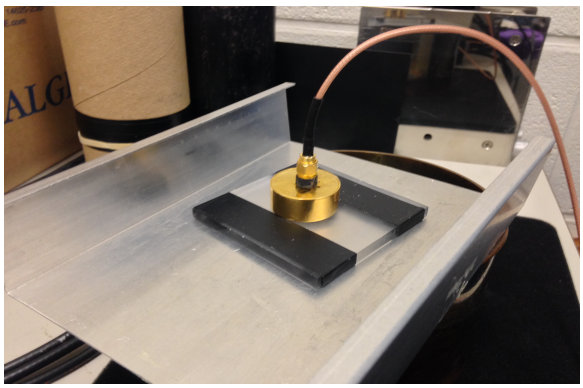

Figure 3.3: 7×7cm spiked acrylic sample used to measure the leaching rate of radon daughters.

was produced by a 500 kBq radium source. The initial activity of the produced ^{210}Po and

^{210}Pb in the acrylic was measured by alpha- and gamma-counting. Then samples were filled

Medium	**Nuclide**	**T** [$^{\circ}C$]	$\boldsymbol{k}$[1/day]	$\boldsymbol{\Delta k}$[1/day]	$\boldsymbol{\tau}$ [day]	$\boldsymbol{\Delta\tau}$[day]
LAB+PRS(5%)+H_2O(2%)+Te(3%)	^{210}Pb	**25**	3.9E-3	4.9E-4	256	32
	^{210}Po		3.5E-3	1.0E-3	288	83
	^{210}Po		2.8E-3	7E-4	357	89
	^{210}Pb	**12**	1.83E-3	0.29E-3	546	$^{+103}_{-74}$
	^{210}Po		<1.53E-3	-	>655	-
LAB+PRS(5%)+H_2O(25%)	^{210}Pb	**25**	8.7E-3	8.7E-4	115	11
	^{210}Pb	**12**	6.36E-4	6.4E-5	1573	157
	^{210}Po		<6.7E-4	-	>1493	-
UPW	^{210}Pb	**25**	2.2E-3	2.2E-4	455	45
	^{210}Po		2.1E-3	6.3E-4	476	143
	^{210}Pb		2.0E-3	6E-4	500	150
	^{210}Pb	**12**	4.8E-4	1.15E-4	2083	500
	^{210}Po		3.8E-4	5.78E-5	2632	400
	^{210}Pb	**95**	1.5	0.35	0.66	0.15
	^{210}Po		2	0.5	0.5	0.1
LAB	^{210}Pb	**25**	8E-4	3E-5	1250	47
	^{210}Po		-	-	-	-
	^{210}Pb	**12**	1.24E-4	1.61E-5	8060	1048
	^{210}Pb		1.6E-4	2.08E-5	6250	813
	Avg ^{210}Po		1.4E-4	1.74E-5	7200	900
UPW+0.25M EDTA	^{210}Pb	**25**	0.0134	3E-3	74	14
	^{210}Po		0.0130	4E-3	77	22
	^{210}Pb	**12**	1.24E-2	9E-4	81	6
	^{210}Po		<3.2E-3	-	>310	-
UPW+0.027M EDTA	^{210}Pb	**12**	4.6E-3	6.0E-4	156	$^{+16}_{-13}$
	^{210}Po		3.7E-3	1.5E-3	270	$^{+185}_{-78}$

Table 3.1: Leaching rates for ^{210}Pb and ^{210}Po into diverse cocktails. The measurements has been performed for three different temperatures (12°C, 25°C and 95°C) [86].

with different cocktails. After the leaching session the activity of the ^{210}Pb in the cocktail was measured directly by a high efficiency gamma counter. In order to measure the activity of ^{210}Po, few milliliter of nitric acid were added to the sample and then it was evaporated on a stainless steel plate used in an alpha-counter. One of the advantages of the sample method over the *in-situ* method is the possibility of investigating the leaching process into different media as well as different temperatures. Table 3.1 contains some of the leaching rate measurements of lead and ^{210}Po.

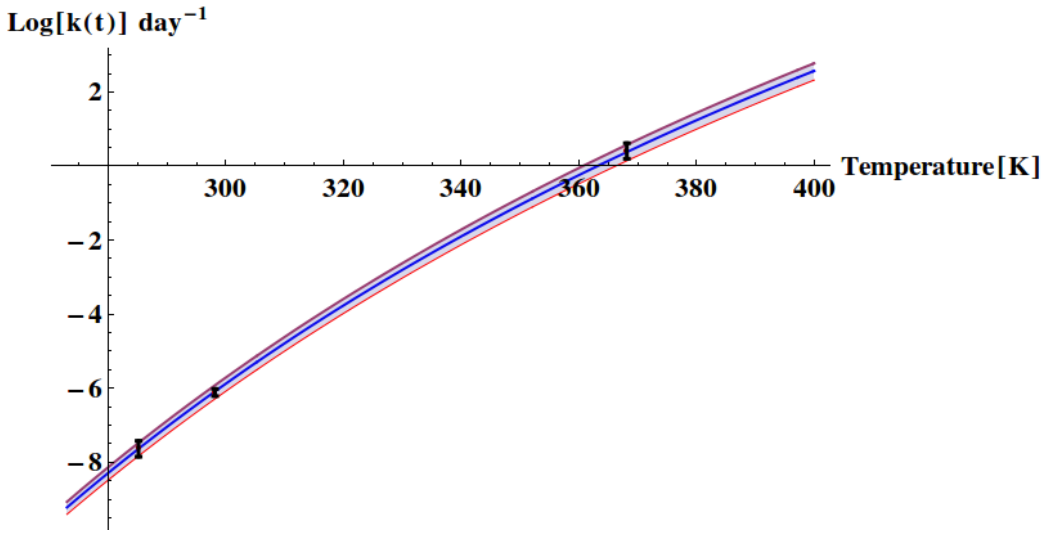

Figure 3.4: Log of the leaching rate of ^{210}Pb into UPW versus temperature which is called Arrhenius plot. Three data points measured at 12, 25, and 95°C and the best fit parameters, where $A = 1.336^{+0.50}_{-0.42} \times 10^{12}$ [day^{-1}] and $E_a = 0.874^{+0.004}_{-0.005}$eV/atom

The leaching measurements confirmed almost the same leaching rate for ^{210}Po and ^{210}Pb. The alpha counting method used to measure the activity of ^{210}Po, has a higher uncertainty (30%) compared to gamma counting, therefore lead assay is more convenient. Fitting the temperature-dependent exponential curve to the data points, two basic parameters of the leaching, activation energy and attempt frequency, can be estimated. Figure 3.4 and figure 3.5 show the best fit curve for the leaching rate of lead and polonium into UPW, respectively.

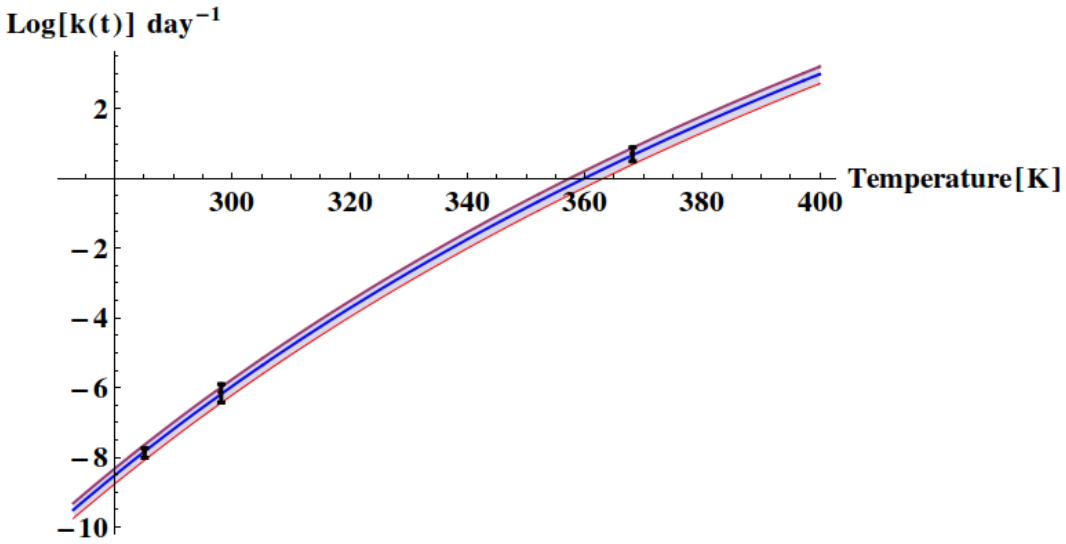

Figure 3.5: Log of the leaching rate of ^{210}Po into UPW versus temperature. Three data points measured at 12, 25, and 95°C and the best fit parameters, where $A = 9.3563^{+2.9}_{-2.7} \times 10^{12}$ [day^{-1}] and $E_a = 0.926^{+0.002}_{-0.002}$eV/atom

3.4 Leaching Model for SNO+

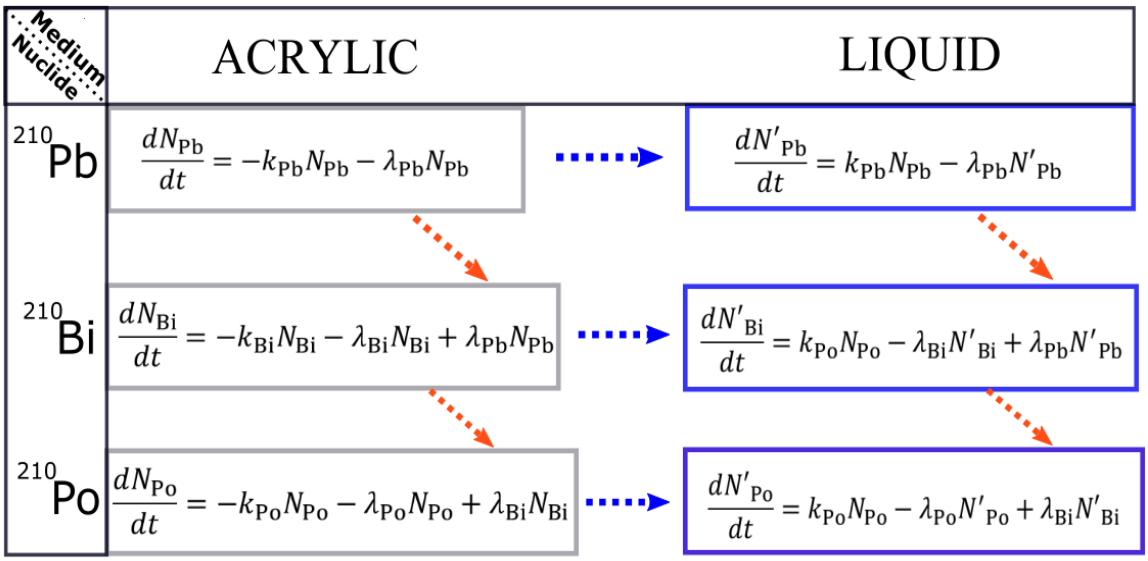

Figure 3.6: The leaching and decay process of radon daughters in the acrylic/liquid. The blue dashed arrow represents the leaching direction and the red dashed line shows the beta decay. However, the model dismisses the ^{222}Rn diffusion from the air into liquid.

From a pragmatic point of view, SNO+ is concerned with how quickly the surface contaminants will leach into the liquid scintillator or water. In addition to the ongoing desorption,

^{210}Pb decays to ^{210}Bi which subsequently decays to ^{210}Po. In the long-term leaching calculations, the decay terms ($-\lambda N$) can not be ignored. In order to determine the activity and concentration of leached contaminants, a simple leaching model was suggested. The model consists of a system of differential equations (Figure 3.6) including the leaching terms as well as the decay terms, where N_x and N'_x are the concentration of the x nuclide in the acrylic and the liquid, respectively. k_x and λ_x are the leaching constant and the decay constant associated to the nuclide x, respectively. Furthermore, when the cover gas system is not installed and the AV is breathing the lab air, ^{222}Rn can diffuse into the liquid and contribute to the concentration of ^{210}Pb. However, the suggested model dismisses the diffusion term for ^{222}Rn, assuming the AV is breathing from the cover gas system. In order to estimate the activity over time through the model, a number of boundary conditions (constraints) should be applied according to the initial concentrations and the environmental factors such as temperature. A simple tool in MATLAB® has been developed by the author, which can calculate the activity over time based on the boundary conditions and the environmental factors. The leaching rate can be interpolated according to the exponential temperature-dependent model as well as the leaching medium and the type of contaminant. The leaching tool estimates the activity and the concentration of the contaminants through the leaching model. It generates a text file including the activity of each isotope in the liquid for every day. In addition to the output text file, It generates a plot which shows the activity and concentration versus time[day]. The leaching model has been applied on some possible leaching scenarios. The following two sections will discuss two possible cases for the leaching of radon daughters.

3.4.1 Accelerating the Leaching Process with EDTA

The SNO+ collaboration suggested loading Ethylenediaminetetraacetic acid, known as EDTA, into UPW to accelerate the leaching process. EDTA is a colorless, water-soluble solid which is widely used to dissolve surface contamination. EDTA loaded cocktails (EDTA+UPW) have been prepared and investigated at Laurentian University. Benchtop measurements showed that EDTA accelerates the leaching rate of ^{210}Pb but has no

effect on the leaching rate of ^{210}Po, see table 3.1. 0.25M EDTA loaded UPW increases the leaching rate of ^{210}Pb by a factor of 30. SNO+ is concerned with the long-term presence of EDTA and the effect on the leaching rate of the radon daughters. The leaching tool was used to estimate the rate of leaching and activity of contaminants for different concentrations of EDTA in water. ^{210}Bi and ^{210}Po are assumed to be in equilibrium with ^{210}Pb ($\lambda_{Pb}N_{Pb} = \lambda_{Bi}N_{Bi} = \lambda_{Po}N_{Po} = 1$), and the initial activity is assumed to be 1. The relative activity was estimated for two different concentration of EDTA loaded into water at 12°C. The results indicate that the activity of the radon daughters in the acrylic will be reduced by 90% in about 500 days with 0.027M EDTA cocktail. The reduction would be five times faster with 0.25M EDTA. Figure 3.7 compares the leaching rate of the cocktails with UPW.

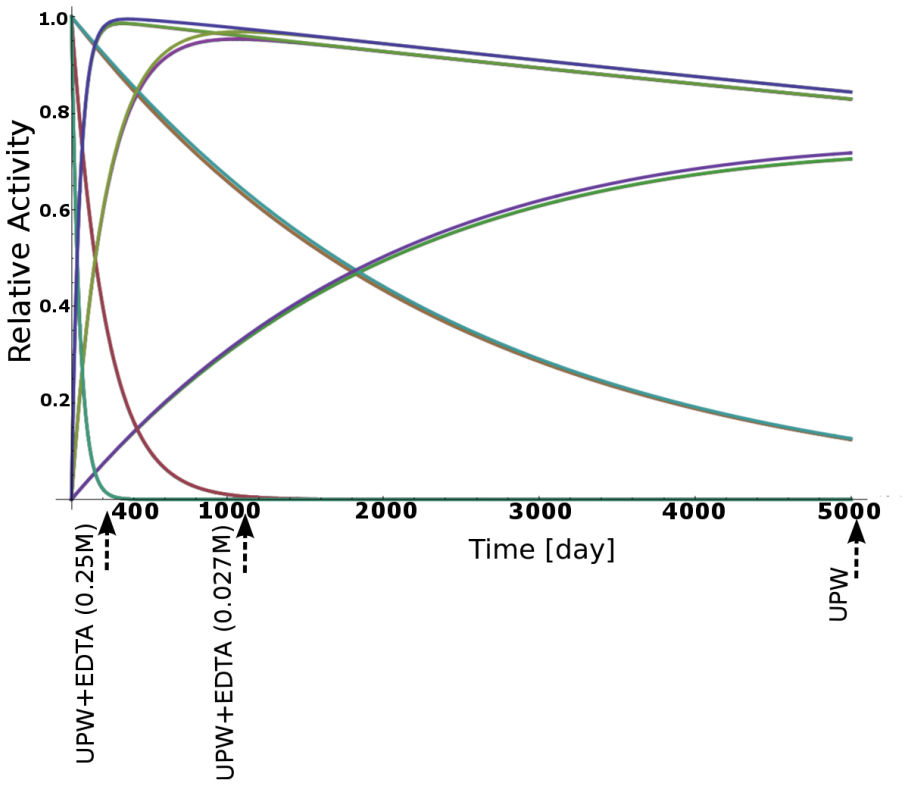

Figure 3.7: The leaching tool was used to calculate the activity of the radon daughters for different EDTA loaded cocktails. As shown in the figure, 0.25M and 0.027M EDTA accelerate the leaching process by a factor of 30 and 6, respectively.

3.4.2 Applying the Leaching Model to a Possible Time-line for SNO+

Another interesting case for SNO+ is determining the activity and concentration of radon daughters for a possible timeline. The leaching tool can be used to study the leaching process for each phase of the experiment. Temperature and the time intervals for each phase should be plugged into the code to estimate the activity. For an instance, the tool has been applied to the following suggested time line:

0) Total initial activity of 1.15 kBq of ^{210}Pb, ^{210}Bi and ^{210}Po.

I) 4 months of UPW at 12°C.

II) 5 months of UPW + (0.027M) EDTA at 12°C.

III) Water will be removed (the activity in the liquid is set to zero and the activity of radon daughters in the acrylic stays unchanged).

IV) 6 months of pure liquid scintillator. The activity in the liquid is negligible compared to the leaching at 12°C.

V) Remove the liquid scintillator (activity in the liquid is set to zero).

VI) Te loaded scintillator (no initial activity in liquid at 12°C. Up to 5 years with this configuration.

The tool makes a text file as an output which contains the concentration and the activity of the contaminants in the liquid as well as the acrylic. It also generates a plot which shows the activity over time. Figure 3.11 shows the activity of radon daughters over six years with the possible time line. The leaching calculations show that the activity of radon daughters would be reduced by 90% in less than three years with the suggested time line. The concentration of lead, ^{210}Bi and polonium are shown in figure 3.8, figure 3.9 and figure 3.10 respectively.

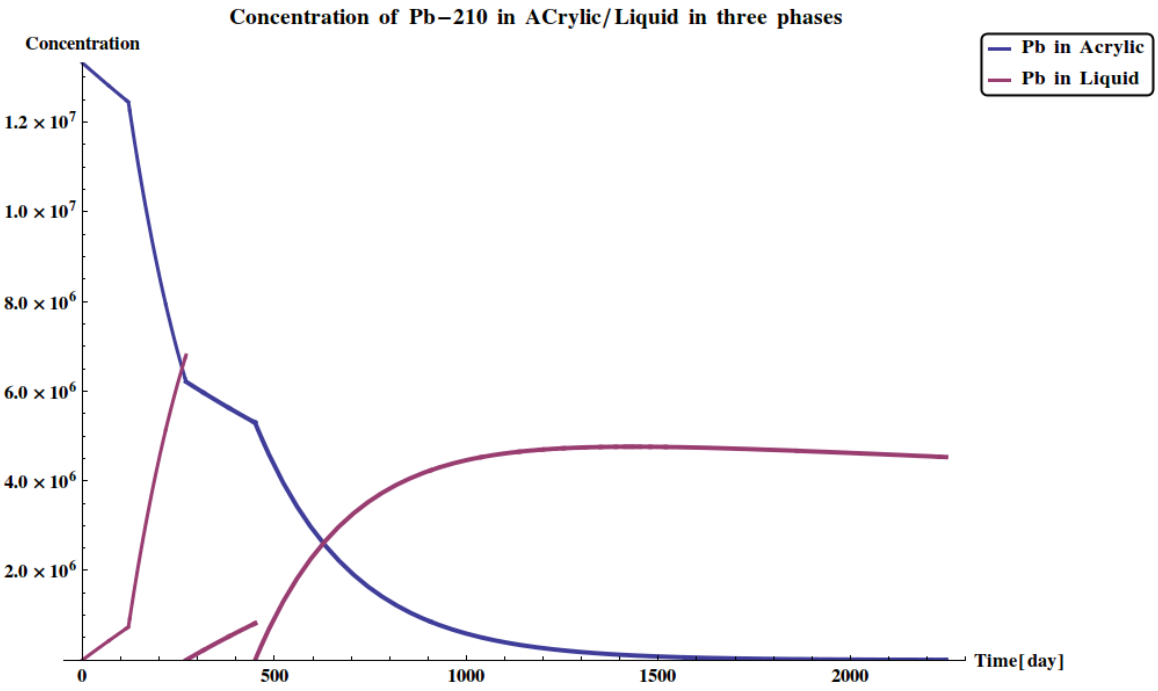

Figure 3.8: The concentration of lead in the liquid (red) and the acrylic (blue).

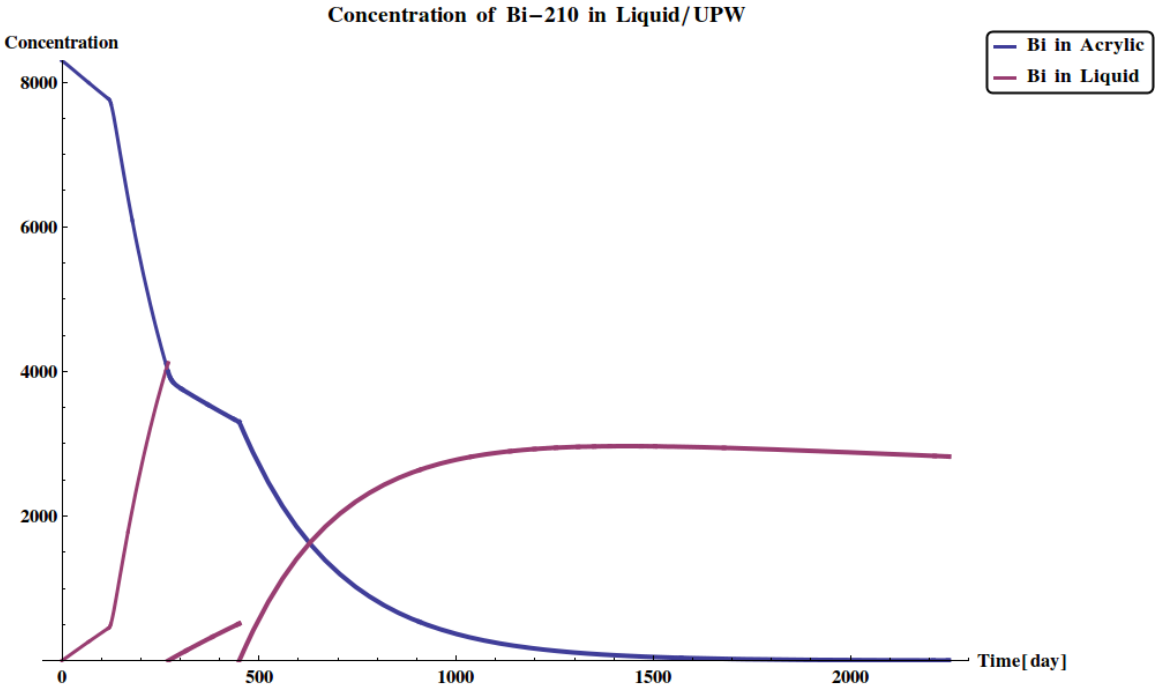

Figure 3.9: The concentration of ^{210}Bi in the liquid (red) and the acrylic (blue).

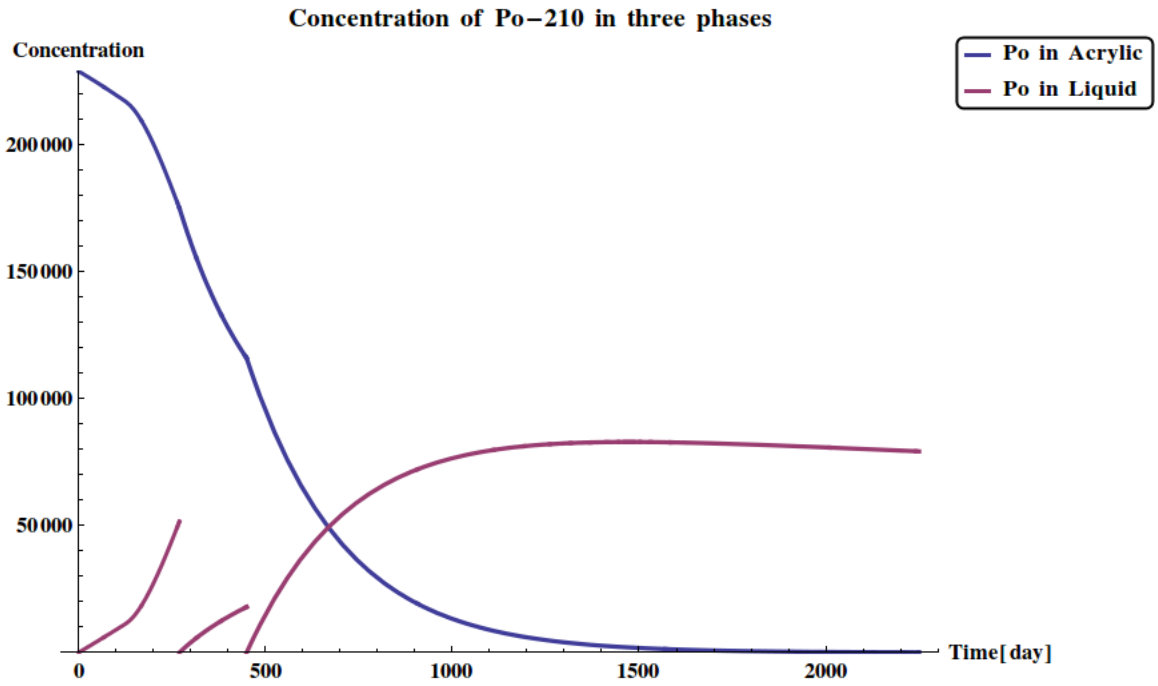

Figure 3.10: The concentration of ^{210}Po in the liquid (red) and the acrylic (blue).

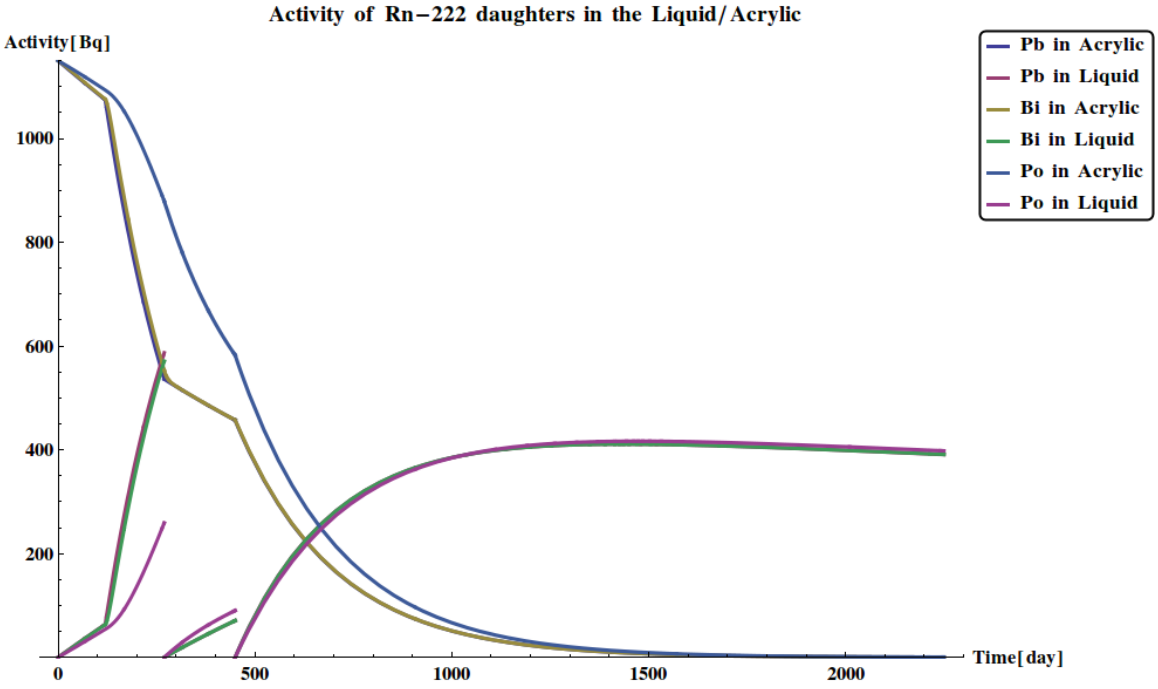

Figure 3.11: The activity of radon daughters over the possible time-line for SNO+.

3.5 Water Assay and Specific Activity of ^{210}Pb in the UPW

From January 27th, 2015, 12:00PM (EST) to January 28th, 12:00AM (EST), an assay was performed on the water which has been contained in the AV for almost 4 months [81]. The AV water level was monitored during the water-fill through the Delta-V system. The water level (in feet) is shown in Figure 3.12. Filling the AV with UPW started on October 8th, 2014. Filling was continued continuously for 34 days (T_{fill}) till the water level reached to 3.9m. The water held roughly at the constant level till January 20th (T_{const}). The water temperature was recorded using a heat sensor, and the average temperature found to be 18.4°C. Using a high efficiency gamma counter the specific activity of ^{210}Pb in the water was measured as $0.26^{+0.04}_{-0.04}$ Bq/m^3. The water assay provided a good opportunity to test the accuracy of the leaching model by comparing the calculated value with the measured value. The following sections will provide a summary of the leaching calculations for the water-fill. Furthermore, the other possible sources of ^{210}Pb in the water will be discussed.

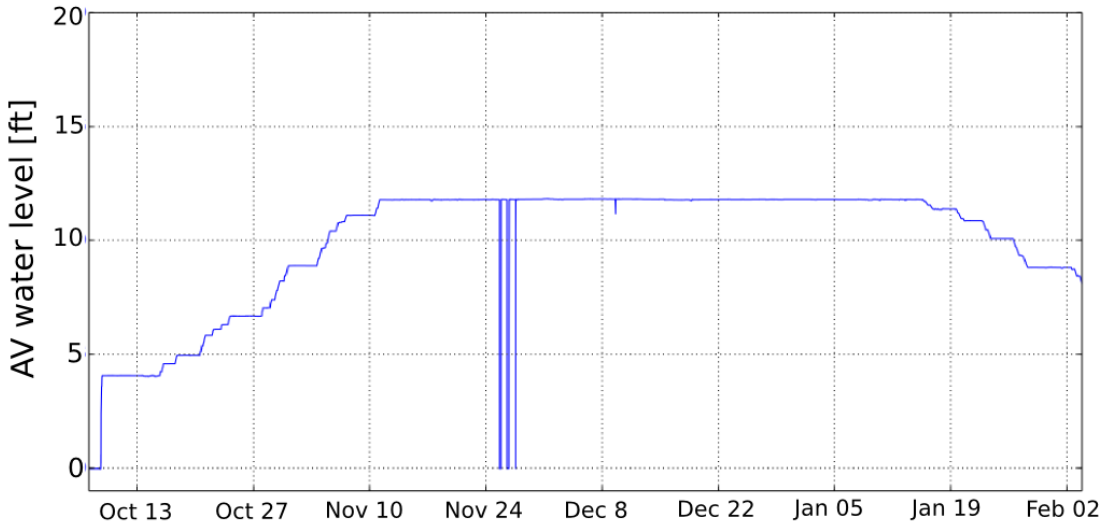

Figure 3.12: The water levels (in feet) during the SNO+ water-fill [81]. The Bubbler system was disconnected for couple of days during the installation of the sliding floor, which caused the noticeable drops in the plot.

3.5.1 Activity of Desorbed ^{210}Pb into UPW

The leaching rate of ^{210}Pb and ^{210}Po into UPW has been measured for three different temperatures (see table **??**). Fitting exponential curve to the data points, two basic parameters of the leaching, E_a and A, can be estimated. Figure 3.13 shows the best fit to the data points. The leaching constant for 18.4°C can also be interpolated through the curve. The leaching constant was estimated as $k(T) = 1.05^{+0.18}_{-0.19} \times 10^{-3}[\text{day}^{-1}]$ for T=18.4°C.

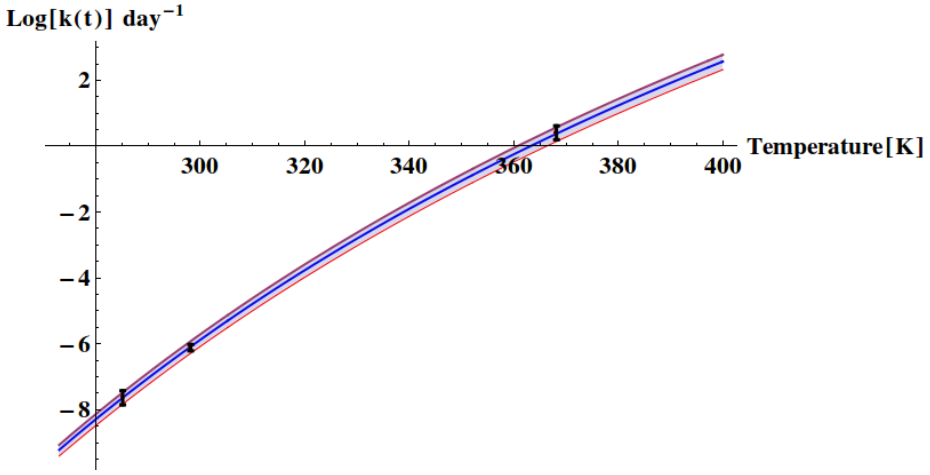

Figure 3.13: Three data points measured for 12, 25, and 95°C and the best fit parameters, where $A = 1.336^{+0.50}_{-0.42} \times 10^{12}$ [day^{-1}] and $E_a = 0.874^{+0.004}_{-0.005}$eV/atom

The initial specific activity of the radon daughters in the acrylic was measured as 2.3 ± 0.8Bq/m^2. The amount of ^{210}Pb leached into the water per unit area can be determined through the following equations (eq. 3.6).

$$\begin{aligned} \frac{dN_a(t)}{dt} &= -k(T)N_a(t) - \lambda N_a(t) \\ \frac{dN_w(t)}{dt} &= +k(T)N_a(t) - \lambda N_w(t) \end{aligned} \tag{3.6}$$

where N_a is the amount of ^{210}Pb in the acrylic leached per unit area. In this case we are more concerned with the total amount of lead in the water, as it was measured in the lead assay. The lead concentration in the water is denoted by $N_w(t)$. λ indicates the radioactive decay constant of ^{210}Pb. The leaching constant, $k(T)$ was estimated for T=18.4°C through the model. The leaching constant for 18.4°C interpolated as $1.05^{+0.18}_{-0.19} \times 10^{-3}[\text{day}^{-1}]$. Surface

integral of $N_w(t)$ all over the area under the water should give the total amount of desorbed ^{210}Pb as a function of time. Although, since T_{fill} is not short enough compared to T_{const}, the leaching process form every level has not initiated at the same time origin. $N_w(t)$ can be used to determine the total leached ^{210}Pb although we have to shift the time origin back according to the water level. Discrete presentation of the total amount of desorbed ^{210}Pb can be expressed as a summation(3.7) over all the data points (i).

$$C_{total}(t) = \sum_{i=1}^{i=t/\Delta\tau} N_w(t - i\Delta\tau)2\pi R(h_{i+1} - h_i) \tag{3.7}$$

where h_i indicates the water level at $t = i\delta\tau$ which is extracted through the time list of water levels. $\Delta\tau$ is time division. R is radius of the detector ($\sim$6m) and $2\pi R(h_{i+1} - h_i)$ is a ring shape differential of the area at each level. Total concentration of ^{210}Pb in the water, C_{total}, can be calculated through the summation of $N_w(t)$ at each level multiplied by the corresponding area which is a ring with a thickness of $dh/\sin\theta$ where $\theta = \cos^{-1}(\frac{R-h}{R})$. The specific activity of ^{210}Pb, *A(t)*, can be determined through equation (3.8).

$$A(t)[Bq/m^3] = \frac{\lambda C_{total}(t)}{V(t)} \tag{3.8}$$

where *V(t)* is the volume of the water which can be calculated in terms of the water level through equation (3.9).

$$V(t) = \pi(Rh(t)^2 - \frac{1}{3}h(t)^3) \tag{3.9}$$

When the situation entails removing the water, equation (3.8) can not be applied anymore but we can assume the water at the maximum level and subtract the amount of ^{210}Pb that could have leached into the water from the area above the water, ($C_-(t)$) (3.10).

$$C_-(t) = \sum_{i=1}^{i=t-T_{Const}/\Delta\tau} (\frac{dN_w(t - T_{int}(h_i))}{dt}).i\Delta\tau.(h_{i+1} - h_i).2\pi R \tag{3.10}$$

where $T_{int}(h_i)$ is the time when the leaching procedure begins at the h_i level. The specific

activity of ^{210}Pb in the water at the time of the assay was calculated as $0.155^{+0.088}_{-0.071}$ Bq/m^3 which is 40% lower than the measured value ($0.26^{+0.04}_{-0.04}$ Bq/m^3) through the lead assay. Figure 2 compares the calculated band with the measured value.

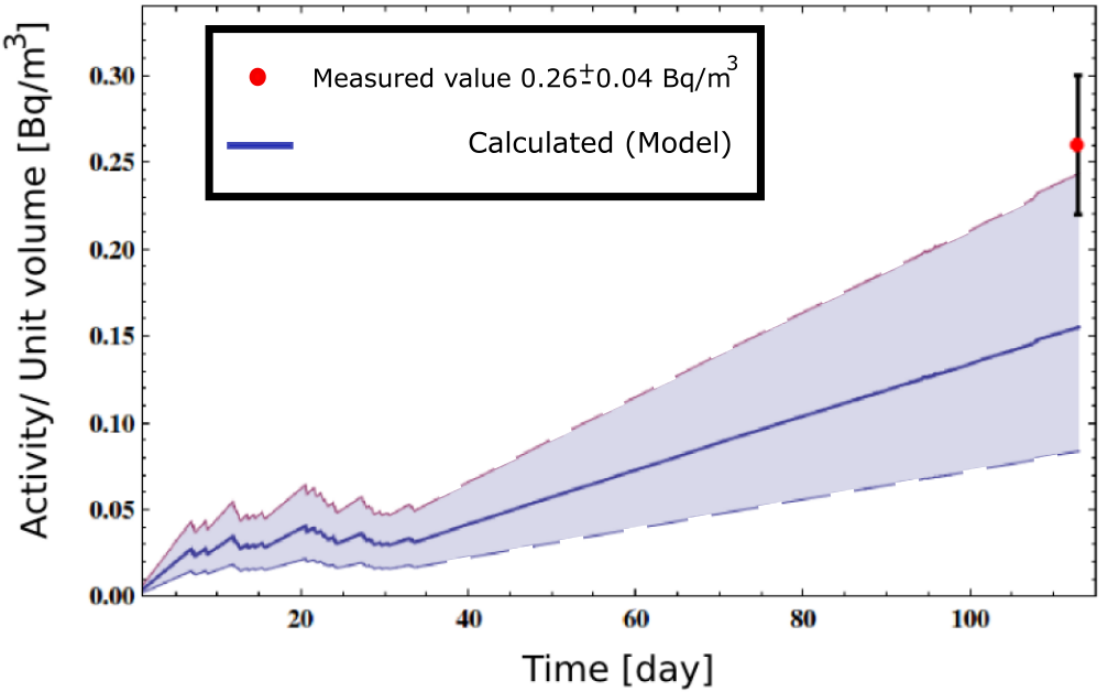

Figure 3.14: Specific activity of ^{210}Pb in the water and the measured activity.

3.5.2 Further Sources of ^{210}Pb inside the SNO+ Detector

3.5.2.1 The Lead Contamination in UPW

In addition to the leaching from the acrylic, there are other sources that could contribute the amount of ^{210}Pb in the water. Ultra-pure water produced in the SNO water plant facility still contains very low level of lead. In August 2014 an underground water assay was performed on a 10 tonne water tank from the SNO water plant. The water assay showed 0.047±0.010 mBq/m^3 specific activity of lead in UPW [81]. This much contamination is

negligible compared to the contamination from the leaching.

3.5.2.2 ^{210}Pb from the Diffusion of Radon into the Water

^{222}Rn is a water-soluble radioactive noble gas which is occuring naturally in the decay chain of ^{238}U. It has a half-life of 3.8 days. There is a relatively higher level of radon underground due to the uranium contamination of the soil and rocks. The radon level at SNOLAB has been measured for many years and the average level found to be 131 ± 6.7Bq/m^3. There is also some level of radon inside the acrylic vessel since the AV is breathing the lab air through an orifice which is located at Deck Clean Room (DCR). The radon levels in the SNO+ acrylic vessel has been assayed. An air tube was placed into the acrylic vessel to about the center and connected to RAD7 on the deck. RAD7 is a highly versatile radon detector used for many different purposes [67]. It turned out that the radon level is 37 Bq/m^3 lower than the lab air. Figure 3.15 shows the ratio of the radon levels in the AV to the control room. The ratio is found to be 0.6703 ± 0.0026 [78].

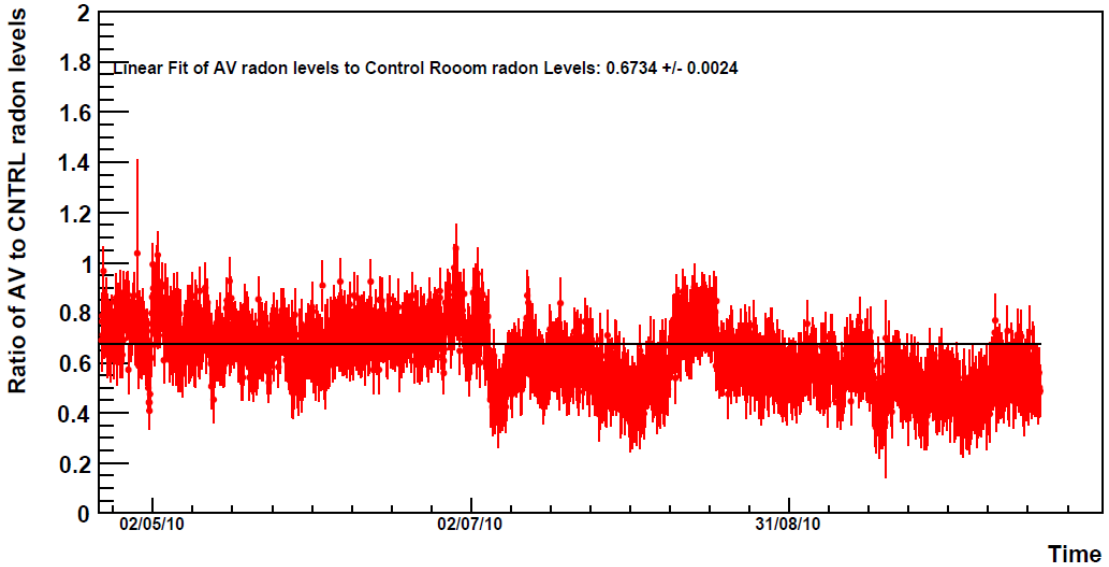

Figure 3.15: The ratio of ^{222}Rn levels in the SNO+ acrylic vessel versus the control room over 4 months [78]. The average level of ^{222}Rn in the AV is found to be 88 Bq/m^3

The radon in the AV could diffuse into the water during the 4 month water-fill and produce

^{210}Pb through the decay chain. In order to study the radon solubility, Fick's law can be applied (equation 3.11). Where $j(r,t)$, the flux in direction x, is proportional to the pertaining gradient of the concentration, $C(x,t)$. D is also denoted as diffusion coefficient.

$$j(r,t) = -D\,\nabla C(r,t) \tag{3.11}$$

Assuming that the concentration of radon in the air is constant we can write the Fick's second law (3.12).

$$\frac{\partial C_w(r,t)}{\partial t} = D\,\nabla^2 C_w(r,t) \tag{3.12}$$

Solving equation 3.12 is the baseline for diffusion calculations. To solve the partial differential equation, the boundary conditions should be applied. The most important boundary condition in the case of gas diffusion in liquid, comes from the partition coefficient between two media [87]. It can be stated as equation 3.13.

$$C_w(0,t) = \kappa\, C_{air}(t) \tag{3.13}$$

Where $C_w(0,t)$ indicates the concentration of radon on the border of the water and air, and $C_{air}(t)$ is the concentration of radon in the air. The partitioning coefficient, κ is the ratio at equilibrium of the dissolved gas concentration in a medium (as water) to the concentration of radon in the air. Diffusion along the x and y axis can be ignored ($\hat{z}$ is downward) due to the symmetry of the diffusion process. The second boundary condition indicates that the radon flux at the bottom of the AV ($z = l$) should be zero (3.14). l represents the depth of the water.

$$\frac{\partial C(z,t)}{\partial z}|_{z=l} = 0 \tag{3.14}$$

In order to solve the equation, the Fourier method of separation of variables can be applied, where $C(z,t)$ is expressed as a product of two functions: $\eta(z)$ and $\theta(t)$. Applying the boundary conditions the concentration of radon as a function of depth and time can be expressed as follows.

$$C(z,t) = \kappa\, C_{air}(1 - \frac{4}{\pi}\sum_{n=0}^{\infty}\frac{e^{\frac{-(2n+1)^2\pi^2 D}{4l^2}t}}{(2n+1)}\ \sin\frac{(2n+1)\pi z}{2l}) \tag{3.15}$$

Equation 3.15 shows the spatial and time-independent distribution of radon for the case of short-term exposure in which the radioactive decay of radon has been ignored. In addition, the concentration of radon in the air, C_{air}, was assumed to be constant. The total activity of radon, $A(t)$ [Bq/m^3], can be obtained by integrating $C(z,t)$ over the volume (3.16).

$$A(t) = \frac{S}{V}\int_0^l C(z,t)dz \tag{3.16}$$

where S represents the cross section [length^2] surface of water and V is the volume. Assuming that the water level is constant the result can be written as equation 3.17.

$$A(t) = \kappa\, C_{air}(1 - \frac{8}{\pi^2}\sum_{n=0}^{\infty}\frac{e^{\frac{-(2n+1)^2\pi^2 D}{4l^2}t}}{(2n+1)^2}) \tag{3.17}$$

The short term-exposure of water to radon is less than three days due to the half-life of radon. Since water-fill is a long-term exposure, the radioactive decay term should be added to the equation. The Fick's second law can be modified as equation (3.18).

$$\frac{\partial C_w(r,t)}{\partial t} = D\ \nabla^2 C_w(r,t) - \lambda C(z,t) \tag{3.18}$$

The boundary conditions are the same as the short-term exposure case. $C(z,t)$ can be written as equation 3.19.

$$C(z,t) = u(z,t)e^{-\lambda t} \tag{3.19}$$

Solving the equation through the separation of variables is analogous to the previous case and is not be described in detail. The final result for concentration of radon in water is expressed in equation 3.20

$$C(z,t) = \kappa\, C_{air}\left(\frac{\cosh\sqrt{\frac{\lambda}{D}}(l-z)}{\cosh\sqrt{\frac{\lambda}{D}}l} - \frac{D\pi}{l^2}\sum_{n=0}^{\infty}\frac{(2n+1)e^{\left(\frac{-(2n+1)^2\pi^2 D}{4l^2}+\lambda\right)t}}{\frac{(2n+1)^2\pi^2 D}{4l^2}+\lambda}\sin\frac{(2n+1)\pi z}{2l}\right) \tag{3.20}$$

Since the water level, l, and the cross section surface, S, are not constant during the water-fill, the total specific activity can be expressed as a summation over the small time divisions (equation 3.21). This method is similar to what we did in the last section to calculate the amount of desorbed ^{210}Pb during the water-fill.

$$A(t) = \sum_{i=0}^{i=t/\Delta\tau} S_i \int_0^{h_i} C(z,t)dz \tag{3.21}$$

Where S_i is the surface in contact with the air which can be written in terms of the water level (h_i) as follows (3.22).

$$S_i = \pi(R\cos\theta)^2 \tag{3.22}$$

where $\theta = \sin^{-1}(\frac{R-h_i}{R})$ and R is the radius of the detector ($\sim 6m$).

The partition coefficient, κ, and the diffusion coefficient, D, should be determined according to the water-fill temperature ($T_{avg} = 18.4°$C). The partition coefficient highly depends on temperature and salinity. Temperature dependency of κ can be expressed by an empirical equation, known as Weigel equation [89] (3.23).

$$\kappa = \frac{^{222}Rn_{(water)}}{^{222}Rn_{(air)}} = 0.105 + 0.405\, e^{-0.05027T} \tag{3.23}$$

Where the partition coefficient of ^{222}Rn between the pure water and air, κ is expressed in terms of temperature, T[°C]. The partition coefficient is calculated to be 0.266 for 18.4°C. Depending on the diffusion process, the diffusion coefficient for radon into pure water can differ. Conventional values for pure molecular diffusion of radon into water range from 1.14×10^{-5} to 1.56×10^{-5} cm^{2}sec^{-1} [91]. Although some of the recent studies show 30 to 50 times greater values [92]. Using the conventionally accepted measurements, the diffusion coefficient of ^{222}Rn was interpolated as 1.15×10^{-5} cm^{2}sec^{-1} for the average

temperature during the water-fill (18.4°C). The total specific activity of radon in water has been calculated through equation 3.21. Figure 3.16 shows the activity of radon in water as a function of time.

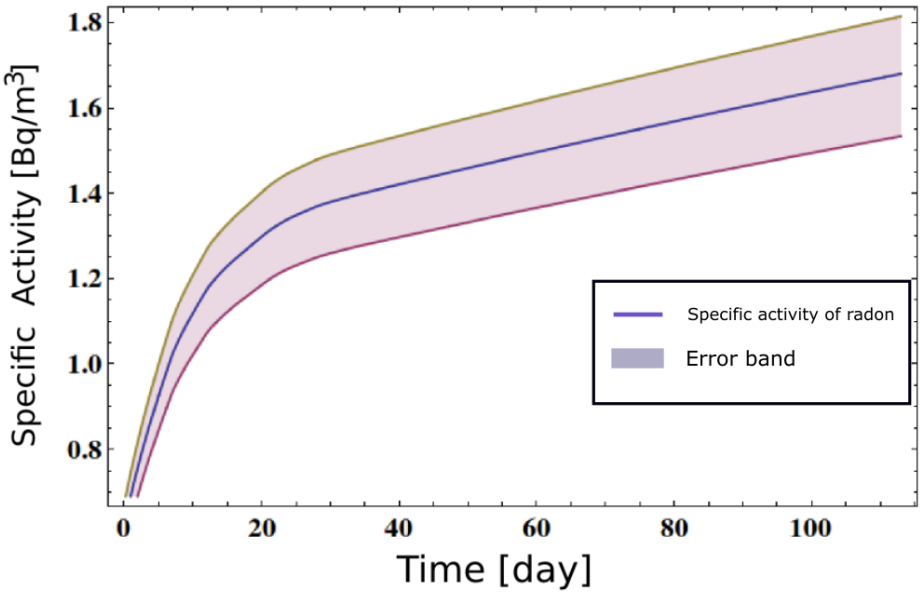

Figure 3.16: Diffused radon in the water (specific activity) during the 4 month water-fill.

The amount of produced ^{210}Pb from the diffused radon, can be calculated through the decay chain. Since we are not concerned with analytical solution, a discrete data set can be generated through the analytical expression for the radon concentration in the water (eq. 3.21). Using a discrete data set makes the calculations simpler. The specific activity of produced ^{210}Pb through the radon diffusion was calculated as $A = 0.012^{+0.003}_{-0.001}$ Bq/m^3. The value is about 10 times lower compared to desorbed ^{210}Pb in the water. Figure 3.17 shows the calculated specific activity of ^{210}Pb in the water during the water-fill.

The total specific activity of ^{210}Pb during the water-fill, from the leaching process plus the ^{210}Pb produced through the radon diffusion, was calculated as $A = 0.169^{+0.085}_{-0.073}$ Bq/m^3. The total calculated activity during the water-fill is shown in figure 3.18. The calculated value is compatible with the measured value from the water assay ($A = 0.26^{+0.04}_{-0.04}$ Bq/m^3) to within 1σ. The diffusion and leaching process might be more complicated in reality due to the temperature gradient from the bottom of the AV. Thermal fluctuations during the water-fill can also affect the process. Although, the result shows that the simple model applied on

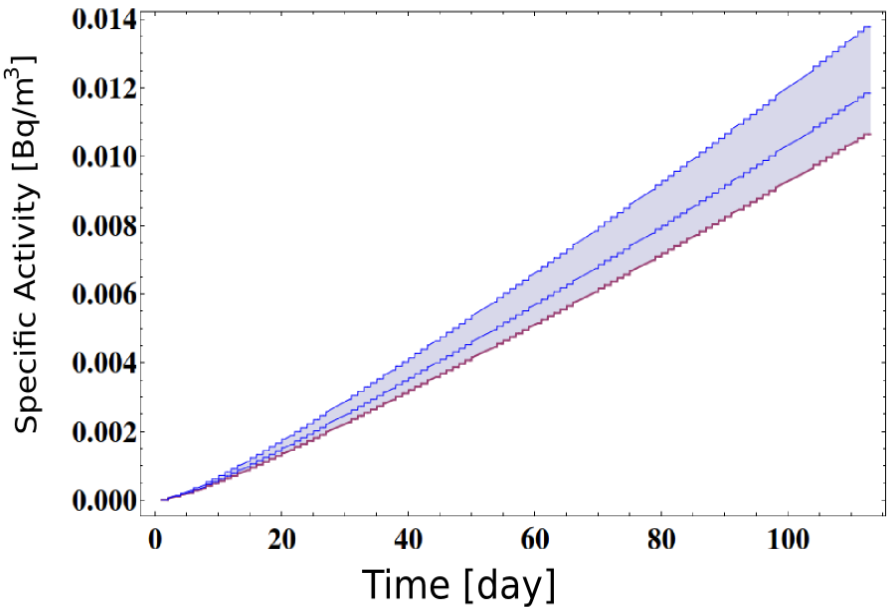

Figure 3.17: Specific activity of ^{210}Pb in the water, produced through the radon diffusion during the water-fill.

the leaching and diffusion can describe the processes adequately.

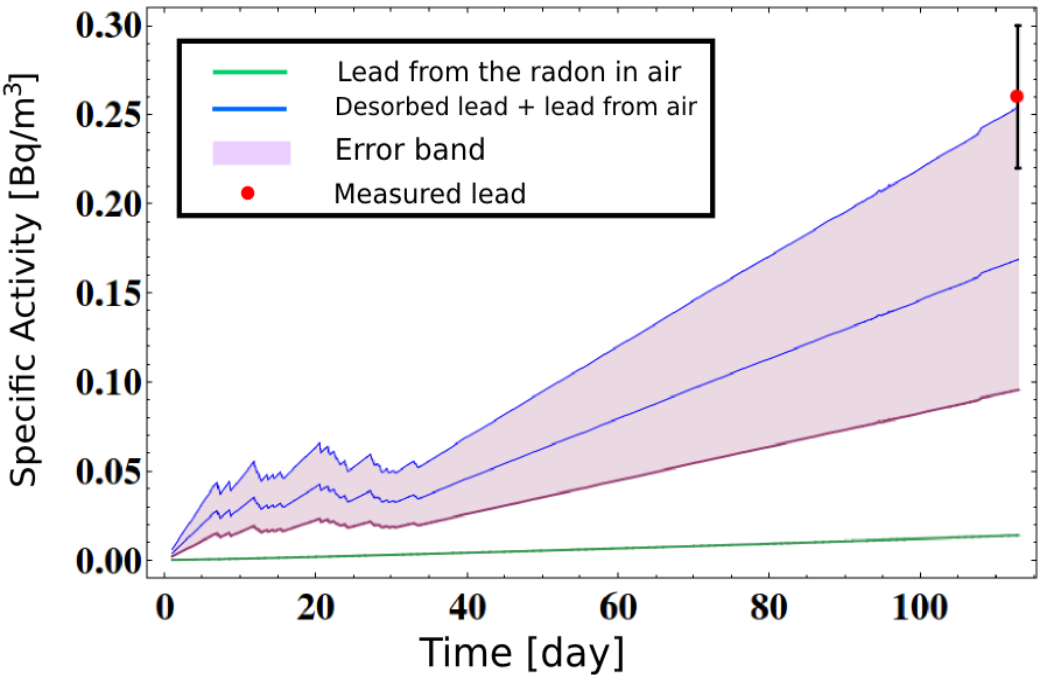

Figure 3.18: Total specific activity of ^{210}Pb in the water is shown in blue (calculated). ^{210}Pb produced through the radon diffusion is shown in green (calculated) and the measured value (red).

Chapter 4: Neck Sense Rope System

4.1 Introduction

The SNO+ AV is supported by the rope system (see figures 2.1a and 2.1b) which includes 10 pairs of hold up ropes which hold the detector from the deck as well as 20 hold down ropes which are mounted to the bottom of the cavity and compensate for the buoyant force due to the lighter density of the liquid scintillator compared to the surrounding water. Therefore, the AV is not fixed and can be displaced with respect to the SNO+ deck or PSUP due to stretching of the ropes. The vertical movements of the AV are expected to be greater compared to the horizontal displacements due to the filling process. For instance the acrylic vessel is expected to move roughly 4" upward once it is fully filled with LAB. The vertical displacements are also the biggest concern since the detector can strike into the surrounding structures such as PSUP, and may get damaged. Thus, monitoring the position of the detector is vital. Monitoring the displacements during the operation can ensure that neither the neck nor the acrylic vessel would hit the surroundings.

SNO+ uses a mechanical system, known as "neck sense rope system" which monitors the position of the neck. In addition, the position of the AV equator is monitored by the equator positioning system. Furthermore, recording the position of the neck and the equator can also help us to study the time-dependent geometrical properties of the AV such as deformation. The sense rope system is briefly introduced in 2.4.3.5.

A very general displacement of the neck can be described in terms of 6 independent variables,

three components of translation (x, y, z), and three components of rotation (ϕ, θ, ψ). The sense rope system consists of 7 independent sense ropes which enables monitoring with 6 degrees of freedom. The accuracy of the system is expected to be about 2mm for the translational components and about 0.3° for the rotational components. Three anchor points were placed on the bottom edge of the lower UI (top edge of the acrylic neck) as it is shown in figure 4.1. The sense ropes are attached to the anchor points with square shaped blocks, known as attachment blocks, which are shown in figure 2.12a. Figure 4.1 illustrates

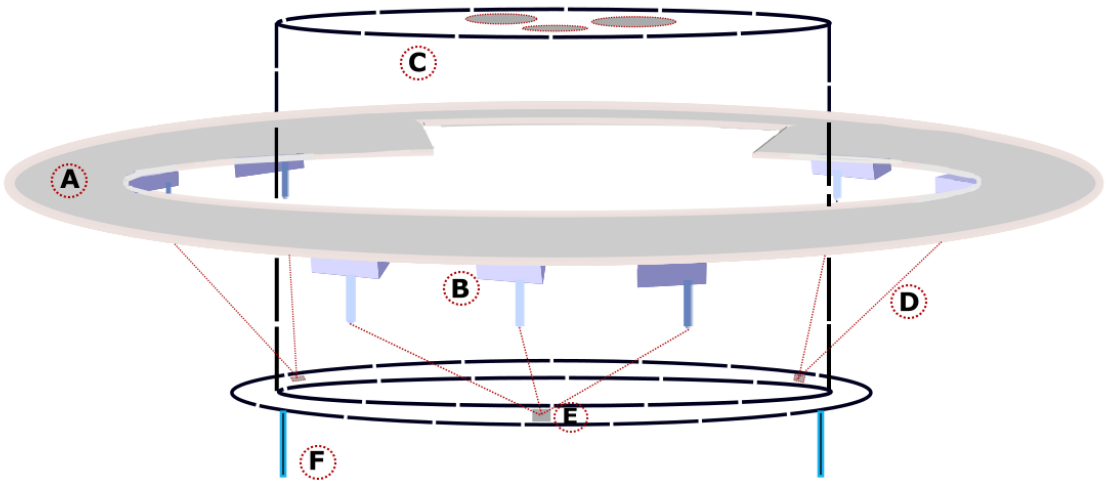

Figure 4.1: Schematic diagram of the sense rope system which shows the following parts: A represents the fixed support plate which is located underneath the sliding floor. B shows one of the sense rope snouts. C shows the lower UI, the UI structure is shown transparent in the figure (dashed black line). D shows one of the sense ropes, attached to the attachment blocks (E). F represents the top of the acrylic neck (chimney). The dimensions are not accurate in the figure.

the sense rope configuration where three ropes are attached to the block number 1 and two ropes are anchored to each of the blocks numbered 2 and 3. At the other end, each rope runs into to a fixed box, known as sense rope snout. Sense rope snouts are mounted downward to a fixed plate which is located underneath the sliding floor (see section 2.4.3.2). The sense rope snouts are fixed with respect to the SNO+ deck. Each sense rope snout contains a high precision potentiometer which enables recording any changes in the length of the ropes. The potentiometers are connected through a simple circuit to the DeltaV system

which is located in the SNO+ control room. DeltaV provides a user interface to read the electrical current passing through the circuit. In order to express displacement (the length of the ropes) in terms of the DeltaV reading, the system required to be calibrated. The system has been calibrated in the SNO+ control room and installed in fall 2014, alongside the sliding floor installation. The following sections will discuss the system in more detail. The underground calibration which was performed by the author will be also described. Finally, we will provide an overview of the steps taken to install the system underground.

4.2 The Sense Rope System

The system consists of both mechanical components as well as the electronics. The mechanical components include ropes, attachment blocks and sense rope snouts. The electronics which enables the final reading, include the DeltaV system and a simple circuit which links the potentiometers to DeltaV. A similar system was also used in the SNO experiment to monitor the position of the neck. The SNO+ sense rope snout has been designed slightly different compared to the SNO experiment, due to the different geometry of the universal interface structure. In addition, the SNO+ sense rope system uses 10 turn potentiometers instead of 5 turn pots used in the SNO system, which enables us to monitor a greater range of displacement. Furthermore, the circuit has been designed in order to monitor the rope lengths with DeltaV. The following sections will describe the sense rope parts in detail.

4.2.1 The Ropes

The SNO+ sense rope system is using the same rope material as the SNO experiment. The rope was a special order of multi-strand Vectran® rope, specifically produced for SNO. Vectran® is a manufactured fiber, spun from a liquid crystal polymer. Vectran golden fiber was selected as the material for the ropes because of its high strength and elastic modulus. In addition, Vectran has a relatively low creep and good chemical stability. The tensile

modulus or elastic modulus of the Vectran is found to be 9.4 Msi (64 GPa) [94]. The elasticity of the ropes has been tested at Laurentian University. Using a theodolite the strain has been recorded for various forces on the rope. The diameter of the rope has been measured as 1.6 mm (fully retracted) to 1.1 mm (200 N applied force). Figure 4.2 shows the strain of the rope versus the applied force. In addition to the elasticity, The stability of the ropes has been tested by remeasuring the strain.

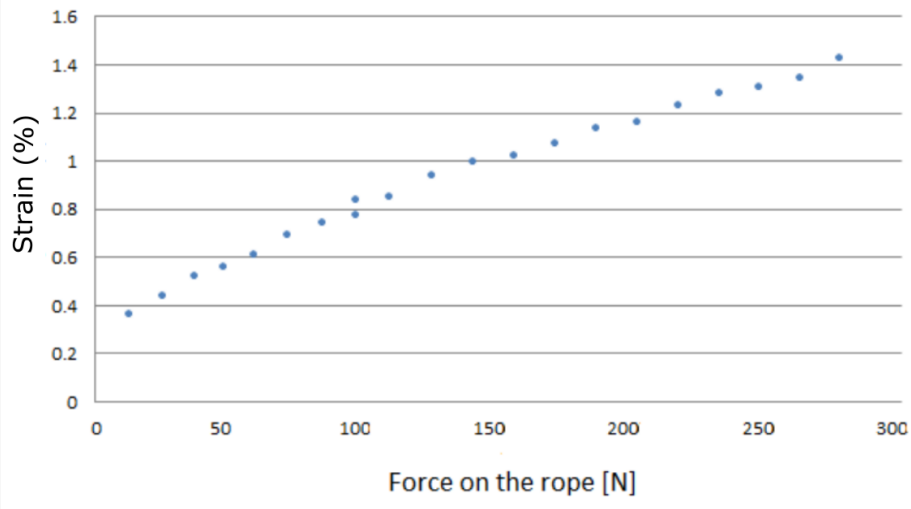

Figure 4.2: The strain of the sense ropes has been recorded for different forces between 9N and 271N. The maximum strain was measured as 1.4±0.02%.

4.2.2 Sense Rope Snouts

The sense rope system consists of 7 sense rope boxes, known as sense rope snouts which are mounted downward on a fixed plate (see drawings B.3a and B.3c), underneath the sliding floor, as shown in figure 4.1. A sense rope snout is shown in drawings B.1a, B.2a and B.2b. Each sense rope snout includes a 2" ×2.5" ×5.5" box which contains a retraction mechanism and a potentiometer. The retraction system keeps the rope retracted, and includes a spring which is connected to a 14 groove brass drum, shown in figure 4.3. Additionally, there is a 5.5" length cylinder which is attached to the bottom of the box, pointing downward as shown in drawing B.1a . The rope runs through the cylinder into the snout, winds around the drum and attaches to the end point using a tiny screw. The drum is connected to

the potentiometer through a plastic connector. The system uses high precision 10 turn BOURNS® potentiometers. This model has a resistance range of ∼100-5000 Ω [95] and independent linearity of ±0.25%. The 5 kΩ BOURNS® pots are specifically designed for control applications where accuracy and high reliability is important. Typical applications include measuring linear distance due to their high resolution of 0.021 Ω [95] and their high stability with the maximum total resistance shift of 2%. The potentiometer has three terminals, where two of the pins are connected to either end of the core and the third pin (middle) is connected to the wiper. Since the potentiometer is not used as a voltage divider,

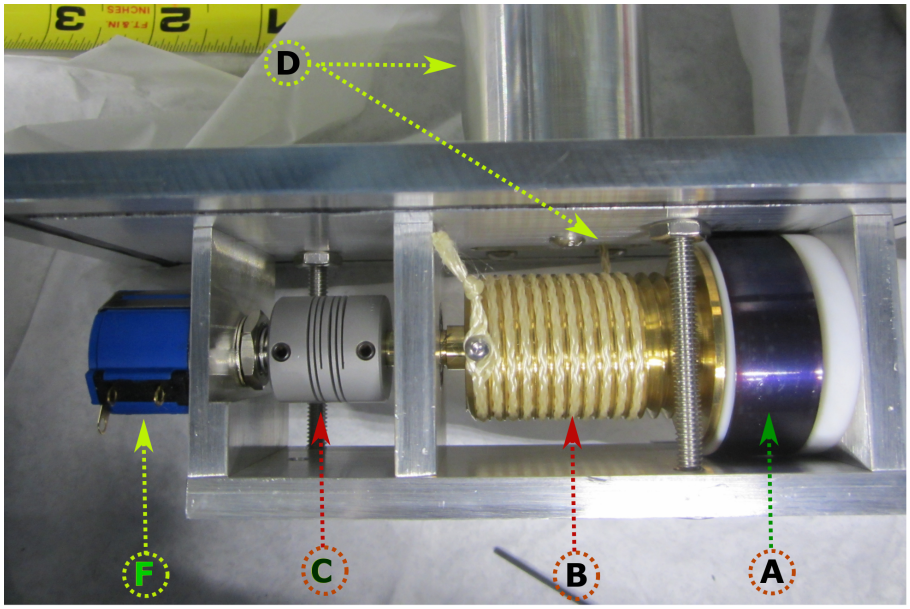

Figure 4.3: Sense rope snout which contains the following parts: **A** shows the spring which retracts the rope. **B** is the brass drum with 14 grooves. **C** shows a plastic connector which connects the potentiometer to the drum and, **F** shows the 10 turn potentiometer. The rope runs through the cylinder, **D**, and winds around the drum.

but simply acts as a variable resistor (rheostat), only two terminals are connected to the circuit. The next section describes the circuit which links the potentiometers to the DeltaV system.

4.2.3 The DeltaV System and the Circuit

DeltaV® is a process control system manufactured by the Emerson Elecric Company, which is used by SNOLAB for many different purposes such as controlling and monitoring the water plant. SNO+ also uses DeltaV for a variety of purposes such as monitoring the LAB purification plant. DeltaV consists of the following: **(i)** a workstation, **(ii)** a control network for communication between the system and nodes, **(iii)** DeltaV controllers that perform local control and manage data and communications between the I/O subsystem and the control network, **(iv)** at least one I/O subsystem per controller that processes information, and **(v)** a power supply. The potentiometers are linked through a circuit to the DeltaV system, shown in figure 4.4. DeltaV has a consistent graphical interface similar to that of the Microsoft Windows operating environment which enables monitoring electrical current passing through the system. Any changes in electrical current represent changes in the length of the ropes. By calibrating the sense rope snouts the length of the ropes can be expressed in terms of the DeltaV reading. DeltaV provides a 22.8V power supply for the sense rope system. The allowable range of electrical current passing through DeltaV is 4 to 20 mA [96]. Therefore, a simple circuit has been designed to keep the current within the allowed range. The circuit includes two resistors, R_1 which is connected in parallel with the potentiometer, and R_2 is connected in series with DeltaV as shown in figure 4.4. The electrical current passing through DeltaV can be expressed as equation 4.1.

$$I_{dv} = \frac{V(R_s + R_1)}{R_{dv}R_s + R_{dv}R_1 + R_2R_s + R_2R_1 + R_1R_s} \tag{4.1}$$

where I_{dv} represents the current passing through DeltaV, R_s is the variable resistance of the potentiometer and V is the applied voltage by DeltaV ($\sim$22.8V). Assuming that $R_1 \sim$ 51.82 k ohm and $R_2 \sim$ 890 ohm, the change in the current versus the resistance of the potentiometer, which is linearly proportional to the change of the rope length, is shown in figure 4.5. As shown in the plot, the suggested circuit keeps the electrical current within the allowed range (4-20 mA). The DeltaV system can measure the current indirectly by measuring the voltage across the R_{dv} resistor with a span of 0-5 V. DeltaV has a 16-bit

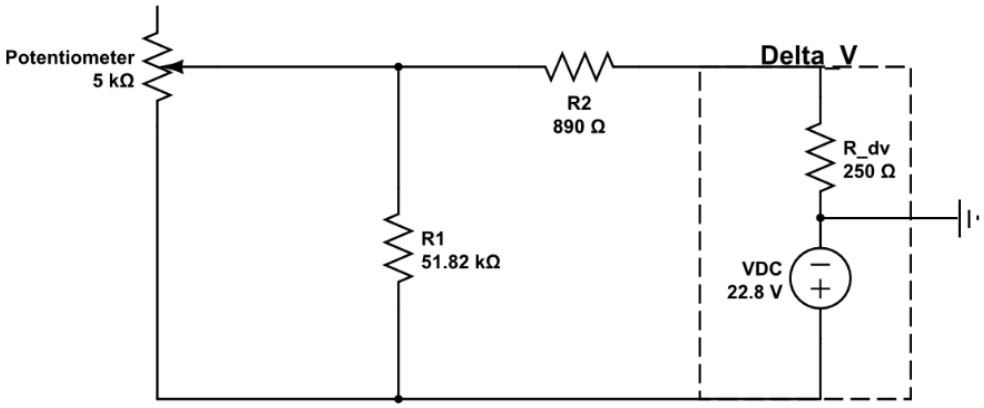

Figure 4.4: Schematic diagram of the sense rope circuit which links the potentiometers to DeltaV.

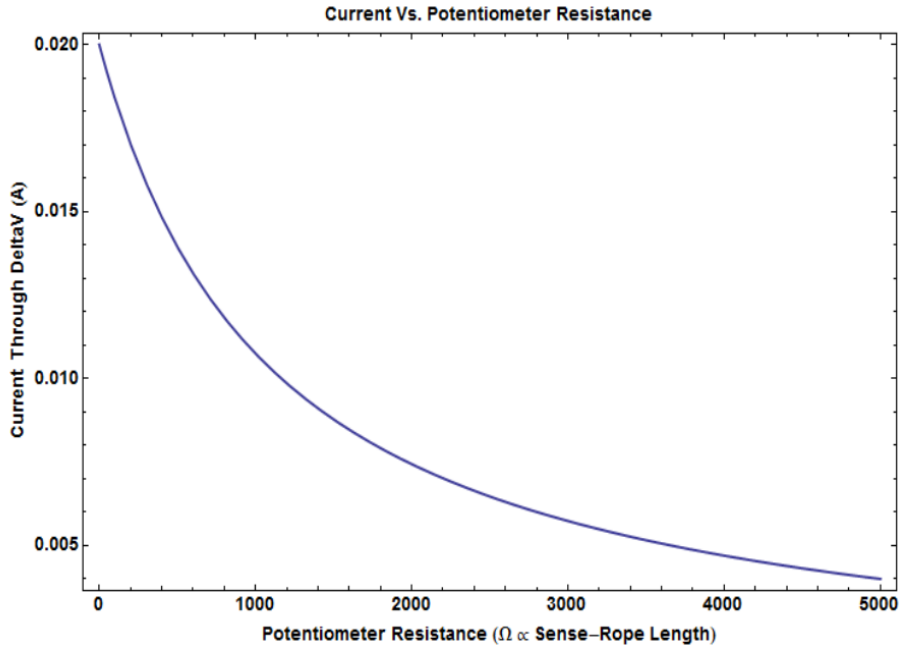

Figure 4.5: The current passing through DeltaV versus the resistance of the potentiometer, where $R_1 \sim 51.82$ k ohm and $R_2 \sim 890$ ohm.

analog to digital converter (ADC) which converts a continuous physical quantity (voltage) to a digital number that represents the quantity's amplitude. The resolution of the system was calculated as 0.076 mV, which means any changes less than 0.076 mV can not be registered. This much voltage resolution corresponds to a 0.305 μA changes in current. From a practical point of view, we are concerned with $\frac{\delta I_{dv}}{\delta L}$, where δL is the smallest measurable change in length of the ropes and $\delta I = 0.305 \mu A$. Using the chain rule, equation 4.2 can be written to

calculate the length resolution.

$$\frac{\delta I}{\delta L} = \frac{dI}{dR_s}\,\frac{dR_s}{dL} \tag{4.2}$$

Where $\frac{dR_s}{dL} \sim 62.5$ ohm/cm is constant since the potentiometers are linear. The value of $\frac{dI}{dR_s}$ depends on the resistance of the potentiometer as shown in figure 4.5. The minimum value of $\frac{dI}{dR_s}$ at R_s=5000 ohm is calculated as 0.6 μA/ohm. The maximum value of δL was calculated as 0.08 mm, which is the smallest measurable displacement. Keep in mind that the 0.08 mm shows the length resolution for DeltaV and the actual precision of the system is affected by many other factors such as the stability of the system (e.g. the stability of potentiometers), precision of the calibration and the accuracy of the deck survey which indicates the initial position of the sense rope snouts and attachment blocks.

4.2.4 Methods to Locate the Neck

As the first step to locate the position of the neck, the DeltaV readings for each sense rope should be converted to a length quantity. The first step is straight forward and requires a comprehensive calibration of the sense rope snouts which will be discussed later in section 4.3. The second step includes calculating the position of the three attachment blocks. There are seven independent rope lengths but the motion of a rigid object can be described using six independent variables. Thus, there is extra information for error checking. In order to find the six components through the seven rope lengths, either the problem can be solved through a linear approximation or the non-linear exact solution can be applied. In the following section, two different methods will be described in detail.

4.2.4.1 Matrix Solution

In this method [97] we define a unit vector for each sense rope, $\hat{r}_i$ $(i = 0, 1, ..., 6)$, which is pointing along the length of the i^{th} rope from the snout to the attachment block. The position of the j^{th} attachment block is also shown as (x_j, y_j, z_j). For small displacements, if length of the i^{th} rope changes by l mm, we can assume that the attachment block moves l

mm as well in the direction defined by $\hat{r}_i$. Since ropes are not orthogonal we should use the inner products of the unit vectors and the Cartesian basis to form a 7×9 transformation matrix shown in equation 4.3.

$$\begin{pmatrix} \hat{x}.\hat{r}_0 & \hat{y}.\hat{r}_0 & \hat{z}.\hat{r}_0 & & & & & & \\ \hat{x}.\hat{r}_1 & \hat{y}.\hat{r}_1 & \hat{z}.\hat{r}_1 & & & & & & \\ \hat{x}.\hat{r}_2 & \hat{y}.\hat{r}_2 & \hat{z}.\hat{r}_2 & & & & & & \\ & & & \hat{x}.\hat{r}_3 & \hat{y}.\hat{r}_3 & \hat{z}.\hat{r}_3 & & & \\ & & & \hat{x}.\hat{r}_4 & \hat{y}.\hat{r}_4 & \hat{z}.\hat{r}_4 & & & \\ & & & & & & \hat{x}.\hat{r}_5 & \hat{y}.\hat{r}_5 & \hat{z}.\hat{r}_5 \\ & & & & & & \hat{x}.\hat{r}_6 & \hat{y}.\hat{r}_6 & \hat{z}.\hat{r}_6 \end{pmatrix} \begin{pmatrix} \Delta x_0 \\ \Delta y_0 \\ \Delta z_0 \\ \Delta x_1 \\ \Delta y_1 \\ \Delta z_1 \\ \Delta x_2 \\ \Delta y_2 \\ \Delta z_2 \end{pmatrix} = \begin{pmatrix} \Delta L_0 \\ \Delta L_1 \\ \Delta L_2 \\ \Delta L_3 \\ \Delta L_4 \\ \Delta L_5 \\ \Delta L_6 \end{pmatrix} \tag{4.3}$$

The matrix transforms the displacement of three attachment blocks to the change in length of the ropes. Equation 4.3 is not sufficient since we have 9 unknowns. The rigidity constraints should be applied as well. The distance between the attachment blocks stays unchanged due to the rigidity of the UI structure, which can be expressed as equation 4.4.

$$\sqrt{(x_i - x_j)^2 + (y_i - y_j)^2 + (z_i - z_j)^2} = d_{ij}\ (const) \tag{4.4}$$

Where d_{ij} is the distance between the i^{th} and the j^{th} attachment blocks. Furthermore, equation 4.5 can be written for displaced attachment blocks.

$$\sqrt{(x_i + \Delta x_i - x_j - \Delta x_j)^2 + (y_i + \Delta y_i - y_j - \Delta y_j)^2 + (z_i + \Delta z_i - z_j - \Delta z_j)^2} = d_{ij} \tag{4.5}$$

Where $(\Delta x_i, \Delta y_i, \Delta z_i)$ is the displacement vector associated with the i^{th} block. Combining the two equations, the constraint can be expressed as equation 4.6.

$$2X_{ij}\ \Delta X_{ij} + 2Y_{ij}\ \Delta Y_{ij} + 2Z_{ij}\ \Delta Z_{ij} = 0 \tag{4.6}$$

Where $X_{ij} = x_i - x_j$ and $\Delta X_{ij} = \Delta x_i - \Delta x_j$. Applying the constraints we are having a total of 10 equations which are excessive to calculate 9 unknowns. One of the equations can be dropped and the nine components can be calculated. The omitted equation can be plugged in to recalculate the position of the blocks for error checking. After calculating the position of the blocks, a new set of unit vectors $(\hat{r}_i)$ should be defined according to the new position of the blocks.

4.2.4.2 Derivatives Method

This method is computationally faster than the matrix solution. The position and orientation of the neck are expressed using 6 quantities, denoted by χ_j $(j = 1, 2, ..., 6)$. The rope lengths can be written in terms of χ_j and the change in the rope lengths with respect to the blocks position, $\frac{\partial L_i}{\partial \chi_j}$, can be calculated numerically. Using the derivatives, we can form a 7×6 matrix similar to the transformation matrix described in the last method. The matrix can be expressed as follows:

$$M_{ij} = \frac{\partial L_i}{\partial \chi_j} \qquad i = 0, 1, ...6. \quad j = 1, 2, ..., 6. \tag{4.7}$$

Where the element in the i^{th} row and the j^{th} column is denoted by M_{ij}. For a narrow range of motions, the change in the rope lengths can be expressed as equation 4.8.

$$\Delta\vec{L} = \mathbf{M}\ \Delta\vec{\chi} \tag{4.8}$$

$\Delta\vec{L}$ will be measured through the potentiometers and we have to calculate $\Delta\vec{\chi}$ which is the unknown quantity. Therefore, we are interested in the inverse of the transformation matrix. In order to make the matrix invertible we have to eliminate one of the rows. To increase accuracy, the eliminated row can be substituted with one of the rows and the position can

be recalculated. Using the inverse of the 6×6 matrix, the motion components can be written as equation 4.9.

$$\Delta\vec{\chi} = \mathbf{M}^{-1}\,\Delta\vec{L} \tag{4.9}$$

Where $\mathbf{M}^{-1}$ is the inverse of $\mathbf{M}$ with one eliminated row.

This method is faster compared to the matrix method, although for big displacements (greater than couple of inches) it reduces the accuracy of the calculated position due to the nonlinear nature of the system.

4.2.5 Sense Rope Survey

The location of the attachment blocks and seven sense rope snouts need to be recorded through a high precision survey. Since the DeltaV reading (current) depends non-linearly on the rope lengths, the intial length of the ropes (the initial position of the anchor points and sense rope snouts) must be known to calculate the neck displacement . Thus, using a theodolite and few fixed calibration points on the deck, the position of the snouts and blocks should be recorded with respect to a fixed origin. The precision of the survey is expected to be about 1-2 mm. Surveying the attachment blocks is challenging since the anchor points are underneith the sliding floor and difficult to see and locate them through a theodolite. In order to address this issue, three points were marked on top edge of the lower UI, right above the attachment blocks, using rotating laser.

4.3 Sense Rope Calibration and Installation

DeltaV registers a number between 0 and 100 for each sense rope snout, which is associated with the electrical current between 4 and 20 mA. In order to convert the readings to the rope lengths, all the sense rope snouts need to be calibrated. Furthermore, a comprehensive calibration is required to investigate the accuracy and the stability of the system. The sense rope snouts have been built in the SNOLAB machine shop and transferred underground. The system was calibrated underground in fall 2014. Simultaneously, the sense rope snouts have been prepared to be installed alongside with the sliding floor. This section will discuss the taken steps to calibrate and install the system.

4.3.1 Preparation and Calibration of the Snouts

The DeltaV response to the change in the rope lengths was investigated by calibrating the system underground. The sense rope circuit which was described in section 4.2.3, was built and tested underground. The value of the resistors were measured using a high precision Fluke® multimeter and the average found to be $R_1 \sim 51.006\text{k}\Omega$ and $R_2 \sim 869\ \Omega$. The resistors are slightly different than what was suggested for the sense rope circuit (see figure 4.4), still keep the current within the allowed range. The uncertainty of the resistors were found to be about $\pm 0.2\%$. In preparation for the calibration, the sense rope snouts needed to be assembled. The following steps were taken in order to prepare the snouts:

- **Visual Inspection**: First, all the snouts were visually inspected to make sure that all the parts are assembled properly and the potentiometers work. The retraction system has been checked for each snout and a sanity test was performed on each potentiometer.

- **Attaching the Ropes**: The proper length of the ropes were calculated according to the position of the sense rope snouts on the fixed plate. This calculation will be discussed later. The ropes were passed through the snout cylinder, wound around the drum and attached to the end point (see figure 4.7b).

- **Snout Wiring**: Each sense rope potentiometer has three terminals, labeled by 1, 2 (wiper), and 3 (slider). A proper length (∼20m) of RHOS® 6-core shielded cable, shown in figure 4.6a, was used to connect each potentiometer to the circuit. The cable has an aluminum shield which reduces the electrical noise. Three of the wires in the cable were soldered onto the three legs of the potentiometer in the following color order: blue to the leg number 1, red to the number 2 and black to 3. In addition to the soldering, a ground connection has been made for each snout by mounting a spade connector as shown in figure 4.6b.

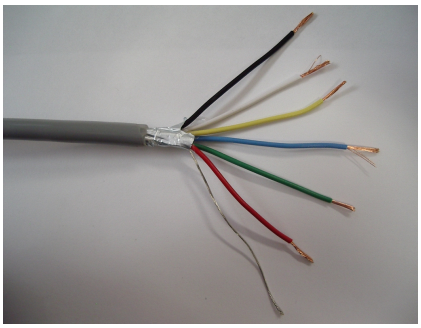

(a)

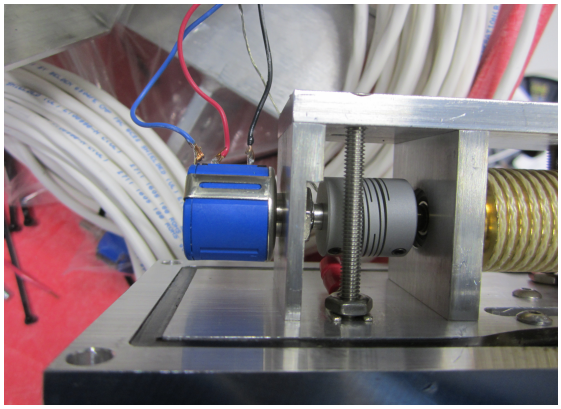

(b)

Figure 4.6: (a) The 6-core shielded cable which used to connect the potentiometers to the circuit. (b) Wires were soldered to the legs of the potentiometers and a ground connection has been made for each snout using the spade connector which is mounted under the nut.

- **Cleaning and Labeling**: After assembling the snouts, they were cleaned and wiped using UPW. Using a piece of heat shrink the shielded cables were sealed at the spot that they run into the snout as shown in figure 4.7a. In addition, all the sense rope snouts were labeled as A, B, ..., G.

In order to perform a calibration, a calibration jig was built out of Unistrut® channels. The calibration jig was a 175 cm long frame including three 33 cm vertical bars (**C**) which were fixed at the end of the frame and a 31 cm movable bar (**B**) as shown in figure 4.8. Sense rope snouts were mounted to the fixed bars at one end of the frame and at the other end the ropes were attached to the attachment block which was mounted on the movable bar. The potentiometers were also linked to the DeltaV circuit, where a user interface has

been provided to monitor the current. For each snout a calibration file was prepared to document the procedure and describe any issues.

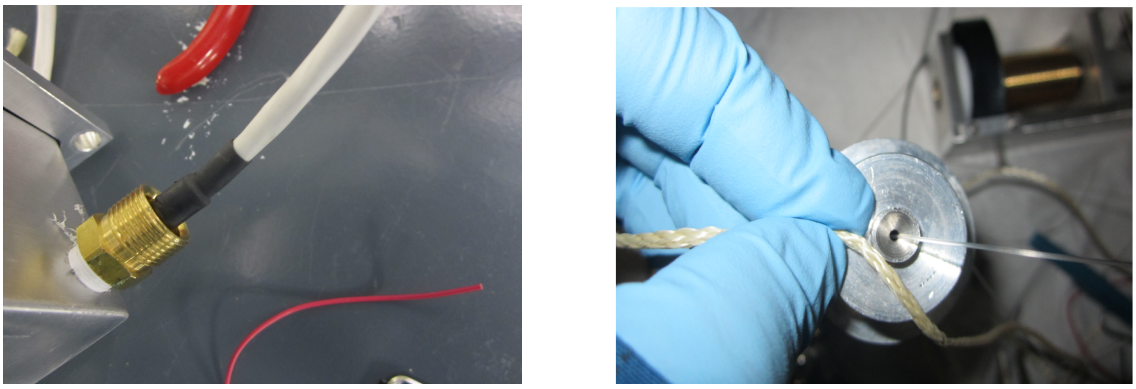

(a) (b)

Figure 4.7: (a) Heat-shrink sealing seal on the sense rope snout. (b) Passing the rope through the cylinder using fishing line.

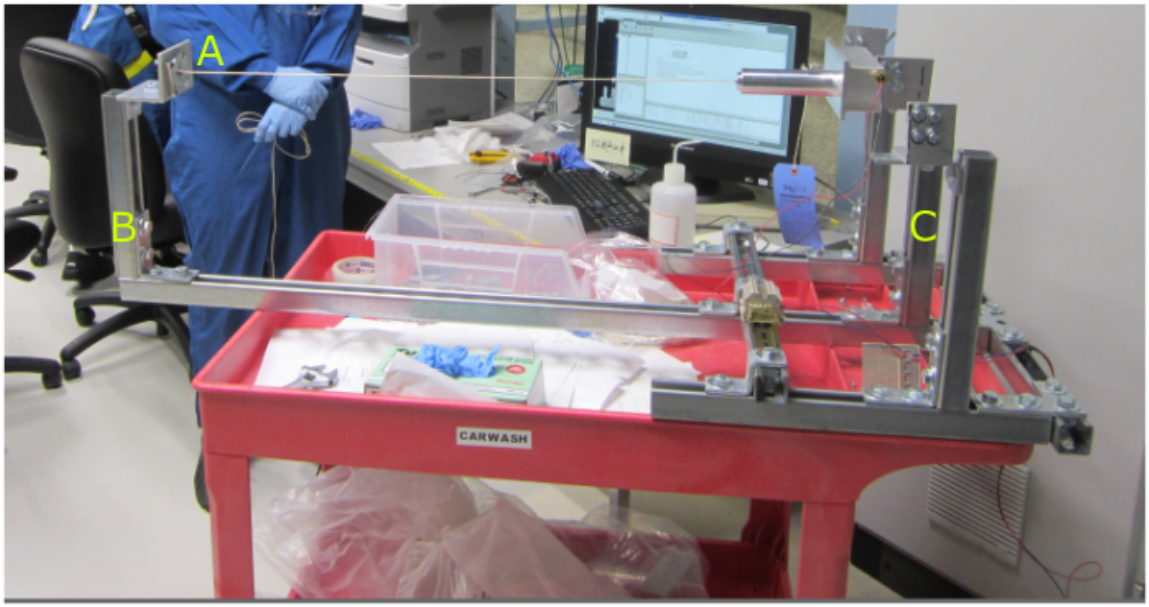

Figure 4.8: Sense rope calibration jig in the SNO+ control room.

in order to calibrate the snouts three main steps has been taken as follow:

- **Sanity Check**: First, The snout has been visually inspected and length of the rope on the snout has been recorded. The snout was mounted and the the resistances and DeltaV readings were measured for the fully retracted and fully extended rope.

- **Calibration Points**: The rope lengths and the corresponding DeltaV readings were recorded starting from the fully extended length to fully retracted. The movable bar was displaced by about 3 cm every time and the calibration point has been recorded. Roughly, 30 calibration points has been recorded for each snout. In addition to that, the applied voltage by DeltaV was monitored to investigate the consistency.

- **Stability Check**: The stability of the system was investigated as the final step. The attachment block set fixed about at the middle of the calibration frame and using three thin spacers (thickness∼1mm) between the plate and the attachment block, the DeltaV readings were measured. Then the spacers were taken off and the readings were remeasured. This procedure has been repeated couple of times to investigate the precision and stability of the system.

The calibration results were presented in a technical report [98]. A curve was fit to the calibration data points in order to find the relation between the rope lengths and the DeltaV readings. The model has five free parameters which has been estimated for each set of data points (snouts). In addition, the standard deviation and residuals of the data points were calculated as well. As an example table 2.10 shows the calibration data for snout B. In addition the best fit curve is shown in figure 4.9a. The residual plot of the data points is also shown in figure 4.9b. The mean of the residuals was calculated as 0.133cm for snout B. The standard deviation was also calculated as 0.8cm.

Displacement [cm]	0.0	4.8	10.1	17.0	24.5	29.6
DeltaV reading [%]	-1.143	-0.085	1.362	3.501	6.246	8.584
Displacement [cm]	34.2	38.2	40.8	44.1	48.1	51.45
DeltaV reading [%]	10.999	13.448	15.076	17.601	20.701	24.501
Displacement [cm]	55.4	62.8	65.6	71.3	76.0	———
DeltaV reading [%]	29.224	41.646	48.109	65.770	89.995	———

Table 4.1: Calibration data for snout B. The retracted length of the rope was measured as 42.8 cm (0.0 cm displacement) with the corresponding deltaV reading of -1.143.

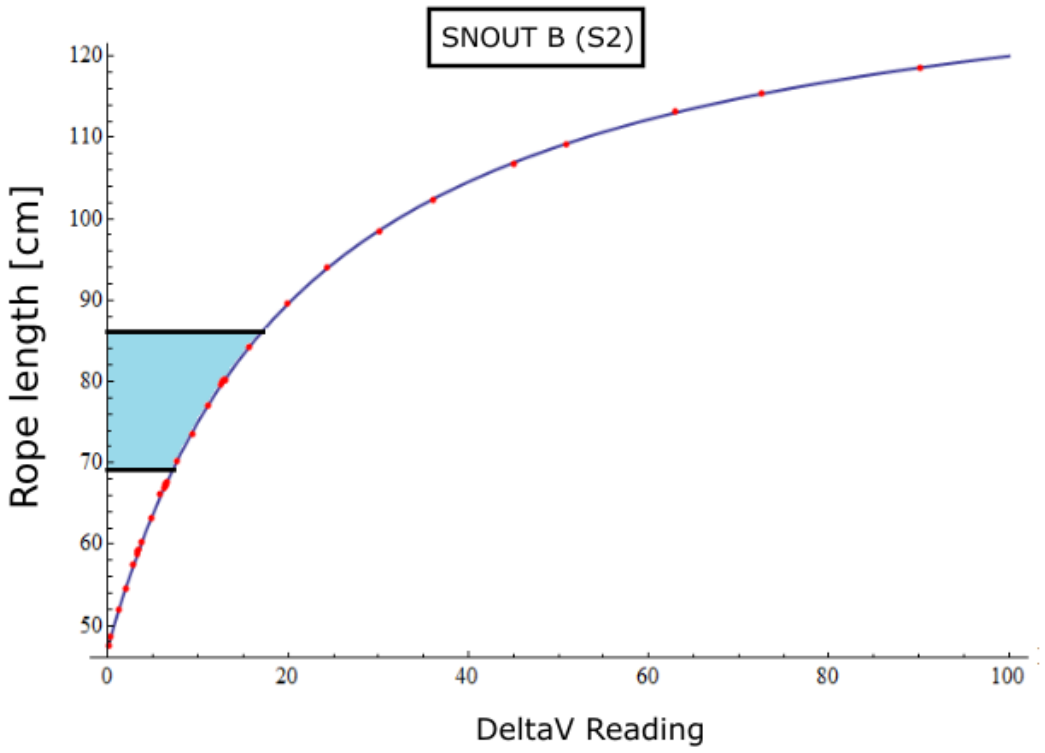

(a)

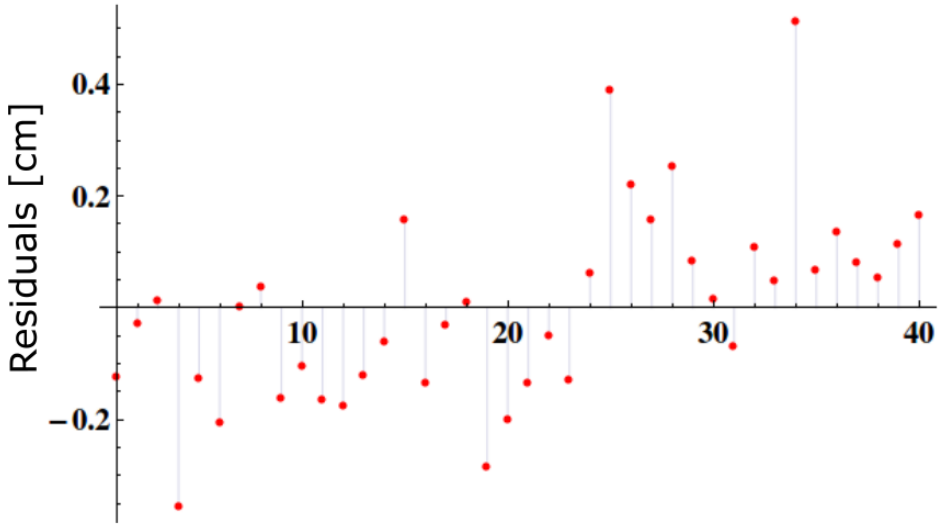

(b)

Figure 4.9: (a) The calibration data points for snout **B** with the best fit curve. The plot shows the rope lengths[cm] versus the DeltaV readings. The blue region is the expected displacement for the rope. (b) The residual plot for the calibration data.

4.3.2 Installation

There are seven 2"×2" square shape sensor plates with a thickness of 1/4", attached to the bottom of the fixed plate as shown in drawing B.3c. The snouts were mounted downward on the sensor plates in the way that the axis of the cylinder aligns with the center of the sensor plate, shown in drawing B.1a. The proper length of the rope was calculated for each snout according to their position. We expect the ropes be about to the center of their length range (middle of the drum) in the LAB phase. The length of the rope from the tip down to the attachment block can be calculated through equation 4.10. Cylindrical coordinate system was picked due to the geometry of the problem.

$$L = \sqrt{(\Delta R)^2 + (\Delta\theta)^2 + (\Delta z)^2} \tag{4.10}$$

Where ΔR, $\Delta\theta$ and Δz are the difference between the radius, polar angle and elevation of the snouts and the attachment blocks. The value for ΔR and $\Delta\theta$ were extracted from the drawings, and Δz was set to $\sim$ 8.7", which is the vertical distance between the tip of the snouts and the attachment blocks when the detector is fully filled with LAB. The sense rope parts including bolts, nuts and the attachment blocks have been cleaned in an ultrasonic cleaner underground. In order to mount the snouts, the fixed plate was held up in the SNO+ DCR, as shown in figures 4.11 and 4.12. The shielded cables are supposed to come up through the pipes cut off (see drawing B.3c). In order to hold the cables under the

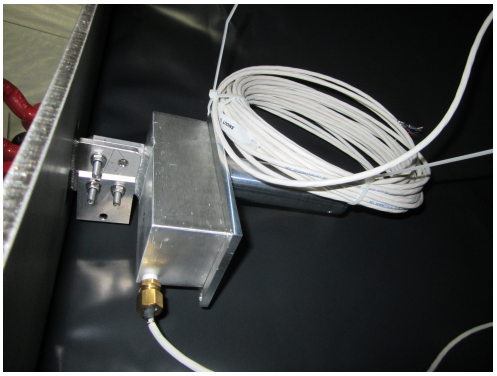

(a)

(b)

Figure 4.10: (a) The holder plates bolted to the sensor plates, on the opposite of the snouts. (b) Ashley stopper knot.

membrane and pass them to the cut off, an aluminum plate (holder) has been built for each sensor plate. They were mounted on the sensor plate, on the opposite side of the snouts, as shown in figure 4.10a. The cables were strapped to a hole on the holders. Using a proper type of knot, known as Ashley stopper knot [99] (see figure 4.10b), the ropes were knotted down to the attachment blocks. The attachment blocks were bolted down to the anchor points, alongside with installing the fixed plate and the sliding floor.

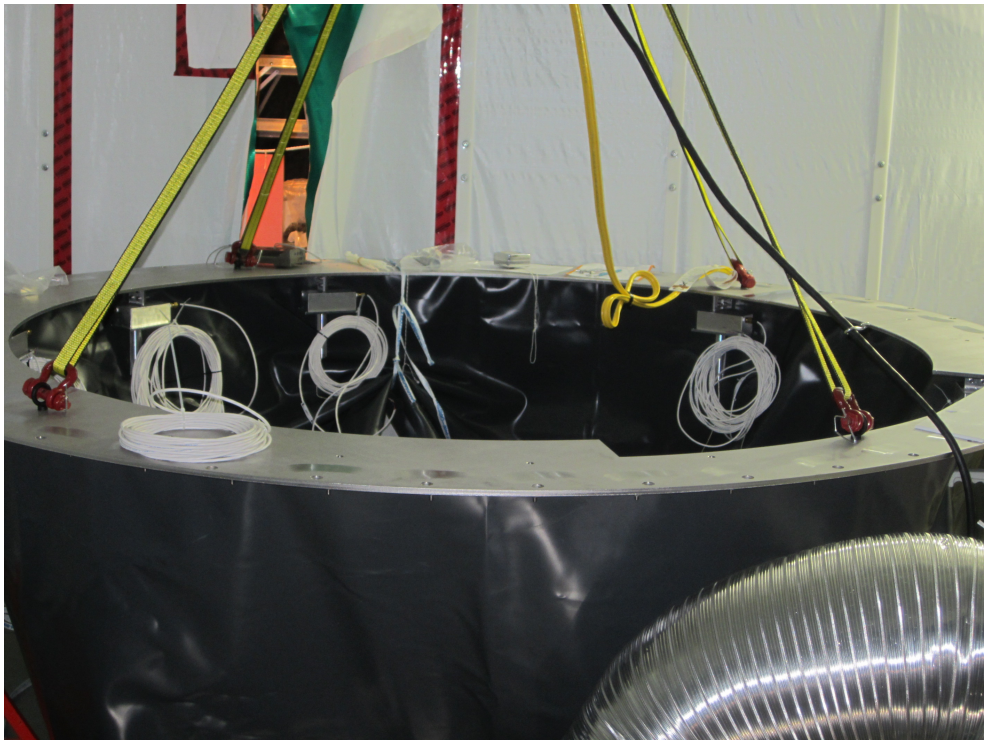

Figure 4.11

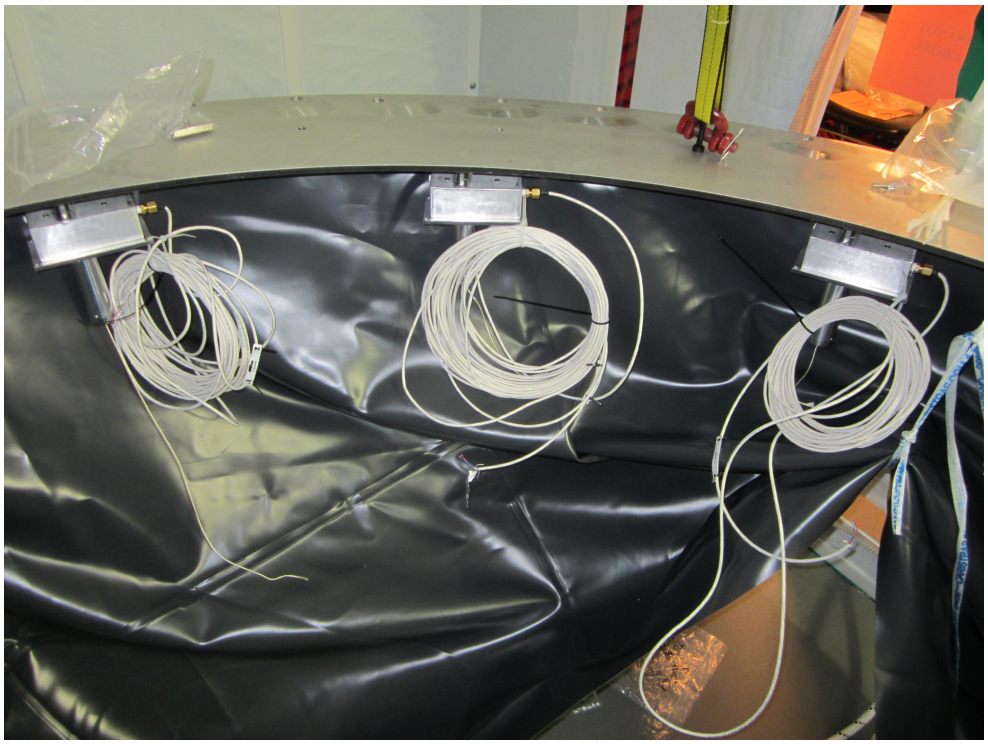

Figure 4.12

Chapter 5: Summary and Conclusions

As pointed out in chapter 2, the highest priority for SNO+ is searching for neutrinoless double beta decay of ^{130}Te. The detector will be loaded with 0.3% natural tellurium with an expected effective Majorana neutrino mass sensitivity in the range of 55-133 meV, just above the inverted mass hierarchy [53]. The possibility to deploy up to ten times more natural tellurium has also been investigated which can lead to a breakthrough in particle physics. In addition to the search for $0\nu\beta\beta$, the SNO+ detector will be able to detect low energy solar neutrinos, geo- and reactor- anti-neutrinos as well as the galactic supernova neutrinos. This thesis has outlined important developments within the SNO+ experiment: The leaching kinematics of the radon daughters into the SNO+ detector and the SNO+ neck sense rope system. The following two sections will summarize these two projects and present the results and the possible future work.

5.1 Modeling the leaching of ^{222}Rn daughters into the SNO+ Detector

Searching for rare events requires very stringent background limits. As it was previously discussed, one of the sources of background in SNO+ originates from the ^{222}Rn daughters implanted into the inner surface of the acrylic vessel. The surface contamination can leach into the detector volume and increase the internal background. SNO+ is concerned with how quickly the radon daughters will leach into the detection medium. Using spiked acrylic samples, several bench-top measurements have been performed to measure the leaching rate of radon daughters into the different media such as UPW, EDTA+UPW and LAB. Based

on the physics of mass transfer, a temperature dependent model has been developed by the author, which can estimate the background levels originating from leaching of radon daughters over time. The model has been applied to study the effect of loading EDTA into UPW in order to accelerate the leaching process. The result indicates that the activity of the radon daughters in the acrylic would be reduced by roughly 90% in about 500 days with a 0.027M EDTA cocktail. The reduction rate would be five times faster with 0.25M EDTA (see figure 3.7). In addition, the model has been used to calculate the levels of backgrounds for a possible time-line for the experiment (see section 3.4.2). The calculation showed that the activity of radon daughters in the acrylic would be reduced by 90% in about three years for the suggested time-line including six months of 0.027 M EDTA loading.

The model has also been used to estimate the amount of leached ^{210}Pb during the 4 month water-fill [81]. In addition, the author had the opportunity to compare the measured data from a lead assay with the calculated value and determine the accuracy of the leaching model. Since the detector had been exposed to the lab air before and during the water-fill, more calculations have been performed to estimate the amount of ^{210}Pb in the UPW which had been produced through radon diffusion into the water [90]. The total specific activity of ^{210}Pb during the water-fill, from the leaching process plus the ^{210}Pb produced through the radon diffusion, was calculated as $A_{calculated} = 0.169^{+0.085}_{-0.073}$ Bq/m^3 which is compatible to within 1 sigma with the measured value from the lead assay, $A_{measured} = 0.26^{+0.04}_{-0.04}$ Bq/m^3 (shown in figure 3.18). There are more possible sources of ^{210}Pb such as diffusion of airborne particles which can be taken into account. Additionally, The leaching medium is treated as a still liquid in this model, although there are fluid streams due to the thermal gradients. Furthermore, filling the AV increases the air diffusion into the water and can affect the leaching process as well. The diffusion and leaching kinetics is very complicated due to the environmental factors such as thermal fluctuations and humidity, although the results from the lead assay showed that the process can be described adequately through the simple suggested model. However there is a possibility for the other effects mentioned above to play a significant role in the leaching process.

5.2 Neck Sense Rope System

Neck sense rope system, described in chapter 4, is a mechanical system which monitors the displacement of the detector neck with respect to the SNO+ deck. Monitoring the displacements during the operation will ensure that neither the neck nor the acrylic vessel would hit the surrounding structures. It can also provide us with some valuable information about the geometrical properties of the AV such as deformation. The system includes seven independent sense rope potentiometers which enable registering possible rotations of the neck as well as translations (6 independent components). The potentiometers are connected to the DeltaV system which reads the electrical current and provides a user interface to monitor the displacement. The system has been calibrated by the author to investigate the DeltaV response to displacements [98]. The accuracy of the calibration found to be about 1mm. The sense rope snouts have also been assembled underground and a circuit has been designed to keep the electrical current within the allowable range for DeltaV. The accuracy of the system depends on many different factors such as the accuracy of the calibration data, the accuracy of the initial position of the sense rope components (survey) and the time-stability of potentiometers, the circuit resistors as well as the chemical stability of the ropes. The sensitivity of the system is expected to be 2mm for translational displacements and 0.3° for rotational components [98]. However, the system might suffer from a higher level of uncertainty due to the imperfect design of the circuit which leads to nonlinear DeltaV response over a large range of displacements. The system has been calibrated and installed by the author alongside with the sliding floor.

In order to complete the project the system requires a proper user interface on DeltaV to monitor the 7 sense ropes. The readings should be converted to rope lengths and as the final step the displacement can be determined using the methods described in section 4.2.4.

Bibliography

[1] W. Pauli, Cambridge Monogr. Part. Phys. Nucl. Phys. Cosmol., 14, 122, 2000.

[2] L. B. Auerbach *et al.* Measurement of electron-neutrino electron elastic scattering, arXiv:hep-ex/0101039, Jan 2001.

[3] E. Fermi. Nuovo Cim., 11, 119, 1934.

[4] E. Fermi. Z. Phys., 88, 161177, 1934.

[5] F. Reines, C. L. Cowan, F. B. Harrison, A. D. McGuire, and H. W. Kruse, Phys. Rev., 117, 159173, 1960.

[6] T. D. Lee and C.-N. Yang, Phys. Rev., 104, 254258, 1956.

[7] C. S. Wu, E. Ambler, R. W. Hayward, D. D. Hoppes, and R. P. Hudson, Phys. Rev., 105, 14131414, 1957

[8] G. Danby *et al.*, Observation of high-energy neutrino reactions and the existence of two kinds of neutrinos. Phys. Rev. Lett., 9, 3644, 1962

[9] M. L. Perl *et al.*, Phys. Rev. Lett., 35, 14891492, 1975.

[10] K. Kodama, N. Ushida, C. Andreopoulos, N. Saoulidou, et al. Observation of tau neutrino interactions. Physics Letters B, 504(3):218 224, 2001.

[11] M. Goldhaber, L. Grodzins, and A. W. Sunyar. Helicity of neutrinos. Phys. Rev., 109:1015 1017, Feb 1958.

[12] J. N. Bahcall, R. K. Ulrich. Solar models, neutrino experiments, and helioseismology *Reviews of Modern Physics*, 1988 - APS.

[13] G. Fiorentini, M. Lissia, F. Mantovani. Geo-neutrinos and Earth's interior, physics.geo-ph-arXiv:0707.3203, 2007.

[14] A. Porta, Reactor neutrino detection for non proliferation with the Nucifer experiment, IOPScience J. Phys 2010.

[15] M. Hounda, T. Kajita, K. Kasahara, S. Midorikawa. Calculation of the Flux of Atmospheric Neutrinos, arXiv:hep-ph/9503439, 1995.

[16] F.J.P. Soler, Colin D. Froggatt, Franz Muheim, Neutrinos in Particle Physics, Astrophysics and Cosmology, 2008

[17] V. Trimble, Rev. Mod. Phys., 60, 859871, 1988.

[18] J. C. Wheeler, Observations and Theory of Supernovae, Am. J. Phys., 71, 11, 2002, astro-ph/0209514.

[19] K. Hirata *et al.*, Observation of a neutrino burst from the supernova SN1987A, Phys. Rev. Lett., 58, 14901493, 1987.

[20] R. M. Bionta *et al.*, Observation of a neutrino burst in coincidence with supernova 1987A in the Large Magellanic Cloud, Phys. Rev. Lett., 58, 1494, 1987.

[21] E. N. Alekseev, L. N. Alekseeva, V. I. Volchenko, and I. V. Krivosheina, Detection of the neutrino signal from SN 1987A using the INR Baksan underground scintillation telescope, JETP Lett., 45, 589592, 1987.

[22] V. L. Dadykin *et al.*, Detection of a rare event on 23 February 1987 by the neutrino radiation detector under Mont Blanc, JETP Lett., 45, 593595, 1987.

[23] J. Bahcall, A. Serenelli, S. Basu, New solar opacities, abundances, helioseismology, and neutrino fluxes, The Astrophysical Journal 621 (1) (2005) L85.

[24] R. Davis Jr. A half-century with solar neutrinos. Usp. Fiz. Nauk, 174(4):408 417, 2004.

[25] R. Davis. Solar neutrinos. II. experimental. Phys. Rev. Lett., 12:303 305, Mar 1964.

[26] J. N. Bahcall and R. J. Davis. Solar Neutrinos: A Scientic Puzzle. Science, 191:264 267, January 1976.

[27] R, Davis JR. and *et al.*, Measurement of the solar Electron-neutrino Flux with the HOMESTAKE Chlorine Detector, The Astrophysical Journal, 496:505 526, 1998 March 20.

[28] K. S. Hirata and *et al.* Observation of 8B solar neutrinos in the Kamiokande-II detector. Phy. Rev. Lett., 63:16 19, July 1989.

[29] D. Casper and *et al.* Measurement of atmospheric neutrino composition with the IMB-3 detector. Phys. Rev. Lett., 66(20):2561 2564, May 1991.

[30] P. Anselmann and *et al.* Solar neutrinos observed by GALLEX at Gran Sasso. Phys. Lett. B, 285(4):376 389, July 1992.

[31] Q. R. Ahmad and *et al.* Measurement of the rate of $\nu_e + D \longrightarrow p + p + e$ interactions produced by ^{8}B solar neutrinos at the Sudbury Neutrino Observatory. Phys. Rev. Lett., 87:071301, June 2001.

[32] The Super-Kamiokande Collaboration, Evidence for oscillation of atmospheric neutrinos, arXiv:hep-ex/9807003, 1998 PRL.

[33] Q. R. Ahmad *et al.*, Direct Evidence for Neutrino Flavor Transformation from Neutral-Current Interactions in the Sudbury Neutrino Observatory, Phys. Rev. Lett. 89, 011301 June 2002.

[34] B. Pontecorvo, Mesonium and antimesonium, Zhur. Eksptl'. i Teoret. Fiz., 1957.

[35] M. C. Gonzalez-Garcia, M. Maltoni, J. Salvado, T. Schwetz,Global fit to three neutrino mixing: critical look at present precision, arXiv:1209.3023-Sept 2012.

[36] A. Gando *et al.* Constraints on θ_{13} from a three-flavor oscillation analysis of reactor antineutrinos at KamLAND, Phys. Rev. D 83, 052002 March 2011.

[37] P. Adamson and *et. al.* Measurement of the Neutrino Mass Splitting and Flavor Mixing by MINOS. Phys. Rev. Lett., 106:181801, May 2011.

[38] W. H, Furry, On transition probabilities in double beta-disintegration, Physical Review, 1939

[39] H. V. Klapdor-Kleingrothaus *et al.* Evidence for Neutrinoless Double Beta Decay, Mod. Phys. Lett. A 16, 2409 (2001).

[40] H. V. Klapdor-Kleingrothaus *et al.*, The Evidence for the Observation of $0\nu\beta\beta$ Decay: The Identification of $0\nu\beta\beta$ Events from the full Spectra, Mod. Phys. Lett. A 21, 1547 (2006).

[41] M. Auger *et al.* Search for Neutrinoless Double-Beta Decay in Xe136 with EXO-200, Phys. Rev. Lett. 109, 032505 July 2012.

[42] A. Gando *et al.* Limit on Neutrinoless $\beta\beta$ Decay of Xe136 from the First Phase of KamLAND-Zen and Comparison with the Positive Claim in Ge76, Phys. Rev. Lett. 110, 062502 February 2013.

[43] M. Agostini *et al.* Results on Neutrinoless Double-β Decay of Ge76 from Phase I of the GERDA Experiment, Phys. Rev. Lett. 111, 122503 September 2013.

[44] M. Agostini *et al.* Results on Neutrinoless Double-β Decay of Ge76 from Phase I of the GERDA Experiment, Phys. Rev. Lett. 111, 122503 September 2013.

[45] R. Arnold *et al.* Measurement of the $\beta\beta$ Decay Half-Life of Te130 with the NEMO-3 Detector, Phys. Rev. Lett. 107, 062504 August 2011.

[46] G. Bellini *et al.* First Evidence of pep Solar Neutrinos by Direct Detection in Borexino, Phys. Rev. Lett. 108, 051302 February 2012

[47] K. Eguchi *et al.* First Results from KamLAND: Evidence for Reactor Antineutrino Disappearance. Phys. Rev. Lett. 90, 021802 January 2003.

[48] E. Fermi, Ricerca Scientifica, 2, 12, 1933.

[49] C. Kraus et al., Eur. Phys. J., 40, 447, 2005.

[50] V. M. Lobashev *et al.*, Phys. Lett., B460, 227235, 1999.

[51] L. Bornschein *et al.*, eConf, C030626, FRAP14, 2003, Physics in Collision Conference(PIC03), Zeuthen, Germany, June 2003.

[52] M. Goeppert-Mayer, Phys. Rev., 48, 512516, 1935.

[53] SNO+ collaboration, Current Status and Future Prospects of the SNO+ Experiment, 2015.

[54] SNOLAB User's Handbook - Revision 2, 26 June 2006

[55] A. Bialek, *et al.*, A rope-net support system for the SNO+ liquid scintillator detector", Submitted to Nuclear Instruments and Methods in Physics Re-search A , 2015.

[56] Borexino Collaboration, C. Arpesella *et al.*, Direct Measurement of the ^{7}Be solar neutrino flux with 192 days of Borexino data, Physical Review Letters , vol.101, no. 9, Article ID 091302, 2008.

[57] D. Braid, PMT Repair Update, SNO+ internal document, SNO+-doc-2393-v2-2014-03-13

[58] V. Lozza, Neutrinoless double beta decay search with SNO+, EPJ Web of Conferences: 01003 (2014).

[59] Z. Carranza-Barnard, Low Radon Permeable Gloves and Laserball Simulations for SNO+, 2014.

[60] T. Araki, *et. al.*, Experimental investigation of geologically produced antineutrinos with KamLAND, Nature, 2005.

[61] Borexino Collaboration, Observation of Geo Neutrinos, Physics Letters B, 2010.

[62] M. C. Chen, Geo-neutrinos in SNO+, Earth, Moon, and Planets 99:221228 Springer, April 2006.

[63] E. Guillian. SNO+-doc-14-v1, May 2007.

[64] B. Dasgupta, and J. F. Beacom, Reconstruction of supernova ν_μ, ν_τ, anti-ν_μ, and anti-ν_τ neutrino spectra at scintillator detectors", Physical Review D , vol. 86, no. 11, Article ID 113006, 2011.

[65] P. Antonioli *et al.*, SNEWS: The Supernova Early Warning System", New Journal of Physics, vol. 6, Article ID 114, 2004.

[66] R. Ford, M. Chen, O. Chkvorets, D. Hallman and E. Vazquez-Jauregui, AIP Conf. Proc. 1338, 183194 (2011).

[67] RAD7 Radon detector user manual Revision 7.4.0, DURRIDGE Company Inc. 2015

[68] Ian. T. Lawson, Radon Levels in the SNO+ Radon Reduction Room and Acrylic Vessel, SNO+ internal report, August 13, 2012, (SNO+ DocDB1453-v7)

[69] J. Kotila and F. Iachello, Phys. Rev. C 85, 034316 (2012).

[70] J. Barea, J. Kotila, F. Iachello, Phys. Rev. C 87, 014315 (2013).

[71] E. Caden, Calibration Hardware and Radioactive Sources for SNO+, Poster presentation CAP 2014.

[72] A. Reichold, K. Clark, I. Coulter, and K. Majumdar, SMELLIE Status. SNO+-doc-1623-v1, August, 2012.

[73] B.A. Moat *et al.* Optical calibration hardware for the Sudbury Neutrino Observatory. Nucl.Instrum.Meth., A554:255 256, 2005.

[74] E. Caden, Sliding Floor Installation Plan, SNO+-doc-2627-v1.

[75] Peter Liimatainen, Sliding Floor Drawings, SNO+-doc-2604-v1.

[76] N. Fatemi-ghomi, Cover gas commisioning report, operational manual, SNO+ Document 2918-v1.

[77] Z. D. Petriw, An Underwater Six-Camera Array for Monitoring and Position Measurements in SNO+, Fall 2012.

[78] Ian. T. Lawson, Radon Levels in the SNO+ Radon Reduction Room and Acrylic Vessel, SNO+ internal report, August 13, 2012, (SNO+ DocDB1453-v7)

[79] Valentina Lozza, Zack Blair, Oleg Chkvoret, Neutron production due to ^{210}Po decay, September 10, 2013, SNO+-doc-2001-v3

[80] David W. McKee, Jerome K. Busenitz, Igor Ostrovskiy, Nucl. Instrum. Meth. A 587 (2008) 272-276

[81] Lina Anselmo *et al.*, Measurement of ^{210}Pb Activity From Acrylic Vessel (AV) Light Water Assay, (SNO+-doc-3134-v1)

[82] Peter G. T. Fogg, William Gerrard, Solubility of gases in liquids: a critical evaluation of gas/liquid systems in theory and practice, J. Wiley, Jan 29, 1991

[83] Michael Leung, The Borexino Solar Neutrino Experiment: Scintillator Purification and Surface Contamination, June 2006

[84] J. Crank, Clarendon Press, The Mathematics of Diusion, Oxford, 1975.19

[85] Oleg Chkvorets, Results on leaching Pb-210 and daughters from acrylic vessel and spiked acrylic samples Draft, Mar 16, 2013, (SNO+doc 1811-v1).

[86] Mark Chen *et al.*, Expected radioactive backgrounds in SNO+. [SNO+-doc-507-v25] DocDB report.

[87] Eric B. Lieberman, Radon Solubility In Water As A Function Of Salinity And Temperature, 2013.

[88] Andrey Rybalkin, Numerical and Analytical Assessment of Radon Diffusion in Various Media and Potential of Charcoal as Radon Detector, December 2012.

[89] Weigel, F, 1978. Chemiker Zeitung, 102 (1978) 287.

[90] P. Khaghani, Determination of ^{210}Pb activity for the water-fill, SNO+ DocDB.

[91] W. S. Broecker, T. H. Peng, Gas exchange rates between air and sea, Jan 2, 1974, 10964.

[92] Syahrir, S. Usman, H. Spitz, J. Weisman, Transport of Radon in Still Water under Steady-State and Transient Conditions, 2004.

[93] D.M. Rogowsky. Assessment Report for Acrylic Vessel in SNO+. Internal SNO+ document, 2011.

[94] Celanese Acetate LLC, Vectran® engineering data.

[95] BOURNS® Precision Potentiometers Data Sheet. 3540/3541.

[96] DeltaV Product Data Sheet, M-Series traditional I/O, OCT 2014.

[97] C.J. Jillings, The Eletron-Sattering Reation in the Sudbury Neutrino Observatory, 1999.

[98] P. Khaghani, Sense Rope Calibration Report, SNO+ DocDB (work in progress).

[99] Clifford W. Ashley, The Ashley Book of Knots, Faber & Faber, 1993.

[100] Alexander Forstner, Implementation of a Passive Pressure Equalizing System into a Low Radioactive Calibration Source Manipulator for the SNO+ Project. March 2007.

[101] Claude-Alain Roulet, Ventilation and Airflow in Buildings. Taylor and Francis 2012

Appendix A: Pressure Fluctuations and the Necessary Breathing Orifice for the Cavity and AV

A.1 Air Pressure in SNOLAB and the Pressure Swing Model

The absolute air pressure in the 6800 level underground is about 23% higher than the air pressure on the surface. Additionally, in order to keep the mine dust out, SNOLAB is at a slightly higher pressure compared to the mine itself. The lab pressure fluctuates due to the mine ventilation activities and seasonal effects. The pressure changes due to the ventilation activities can sometimes be very rapid with the rate up to 0.5 psi within a 10 minute period [54]. The air pressure in the lab has been continuously monitored, see figure A.1 as an example.

Most of the pressure changes take place within a several hour period, although there are some rapid changes over a period of just 5-10 minutes. The rapid pressure changes can be described through equation A.1, which is known as the pressure swing model.

$$P = P_\circ \pm \Delta P(1 - e^{-\lambda t}) \tag{A.1}$$

where P and $P_\circ$ are the final and initial pressures, respectively. ΔP represents the difference between the final and the initial pressure. λ is called the decay or rise constant, and t represents time. The $+$ sign is used for the case that pressure rises while the $-$ sign is for the pressure drops. A search through the data was done to find sudden pressure changes on

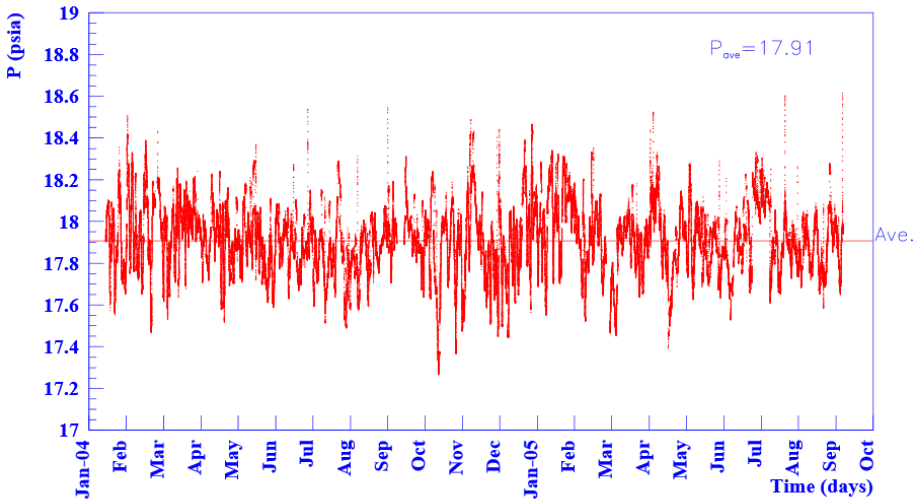

Figure A.1: The change in the air pressure in SNOLAB versus time. Recorded for the time period between Jan 2004 and Sept 2005. It is observed that the absolute pressure is maintained between 17.3 psi 18.6 psi [54].

the order of 15 minutes or less, in which the pressure changed by at least 0.2 psi. Fitting the data to the swing model, λ and ΔP can be determined for the rapid pressure changes. The maximum pressure rise in the lab was found as shown in equation A.2.

$$P = P_\circ + 0.64(1 - e^{-0.20t}) \tag{A.2}$$

while the maximum pressure drop can be expressed as equation A.3.

$$P = P_\circ - 0.63(1 - e^{-0.11t}) \tag{A.3}$$

A.2 Necessary Breathing Orifice for the AV and Cavity

The rapid pressure changes can make a huge pressure difference between the lab and inner volume of the acrylic vessel, which might damage the detector. In order to balance the pressure, breathing is necessary for the cavity and AV. The cover gas system which was briefly introduced in chapter 2, acts as the lung of the detector when the detector is operating. Although, when the detector is empty, a proper size hole is required to let the air flow through and balance the air pressure. The allowable stress (pressure difference) on the detector is found to be 600 Pa [100]. The hole should be big enough to keep the stress below this limit. Assuming the maximum pressure change through the swing model, the proper size of the orifice should be calculated. The flow rate through an orifice can be described through equation A.4 [101].

$$Q = C_d A \sqrt{\frac{2\Delta P}{\rho}} \tag{A.4}$$

where Q is the flow rate [m^3/s], C_d is the discharge coefficient which is 0.61 for an orifice, A is the area of the orifice, ΔP is the pressure difference and ρ is the air density. Assuming the air as the ideal gas, the number of moles passing through an orifice, $n(t)$, can be expressed as shown in equation A.5.

$$n(t) = \frac{\Delta P(t)\, V}{RT} \tag{A.5}$$

where V represents the volume of the cavity or AV in our case, R is the gas constant and T is the temperature. Furthermore, using the molar density of the air, M, the flow rate can be written in terms of the time derivative of the number of the moles (see equation A.6).

$$Q = \frac{\dot{n}(t)\, M}{\rho} \tag{A.6}$$

where $\dot{n}(t)$ represents the rate of the number of moles passing through the hole. Mixing the three equations, the stress on the AV, ΔP, can be derived in terms of the area of the orifice, as shown in equation A.7.

$$\frac{d\Delta P(t)}{dt} = A\frac{C_d RT\sqrt{\rho\Delta P}}{MV} \tag{A.7}$$

Using the pressure swing model, $\Delta P(t)$ can be found through the maximum rapid pressure change. The volume of the cavity and AV are found to be 6263 m^3 and 906.9 m^3, respectively [54]. Assuming the maximum pressure change, the stress on the AV can be determined for different seizes of the orifice, as shown in figure A.2. Theoretically speaking, any orifice with the area bigger than 26 cm^2 should be able to safely balance the pressure and keep the stress below the limit. Likewise, the same calculations has been done for the cavity volume. The stress over a time period of 10 min is shown in figure A.3. The minimum size of the orifice for the cavity is found to be 310 cm^2.

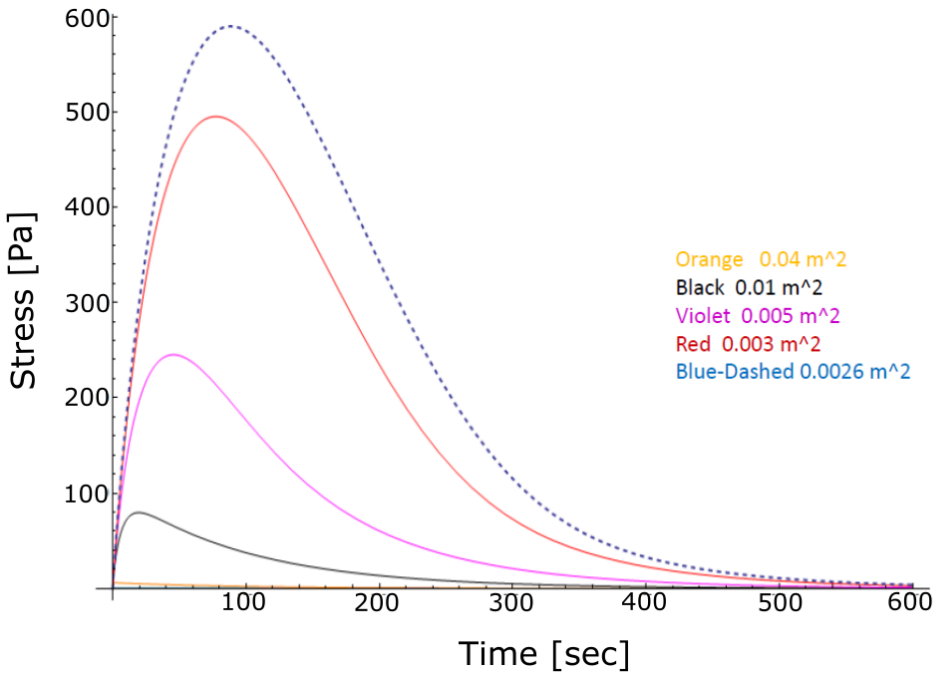

Figure A.2: The stress change on the AV versus time for different sizes of an orifice. The maximum rapid pressure change has been assumed and the stress is shown over a time period of 10 min.

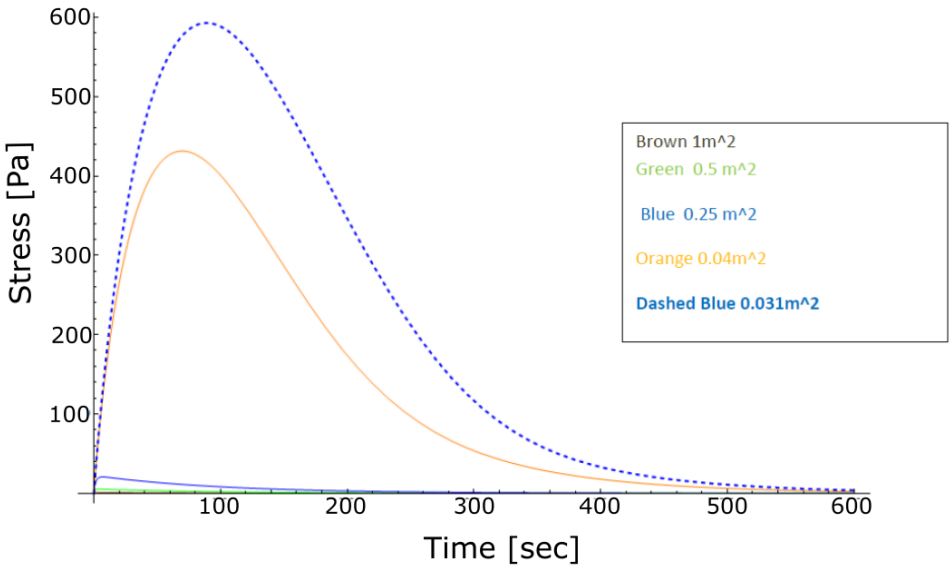

Figure A.3: The stress change for the cavity over a time period of 10 min.

Appendix B: Sense Rope Drawings

Sense Rope Snouts

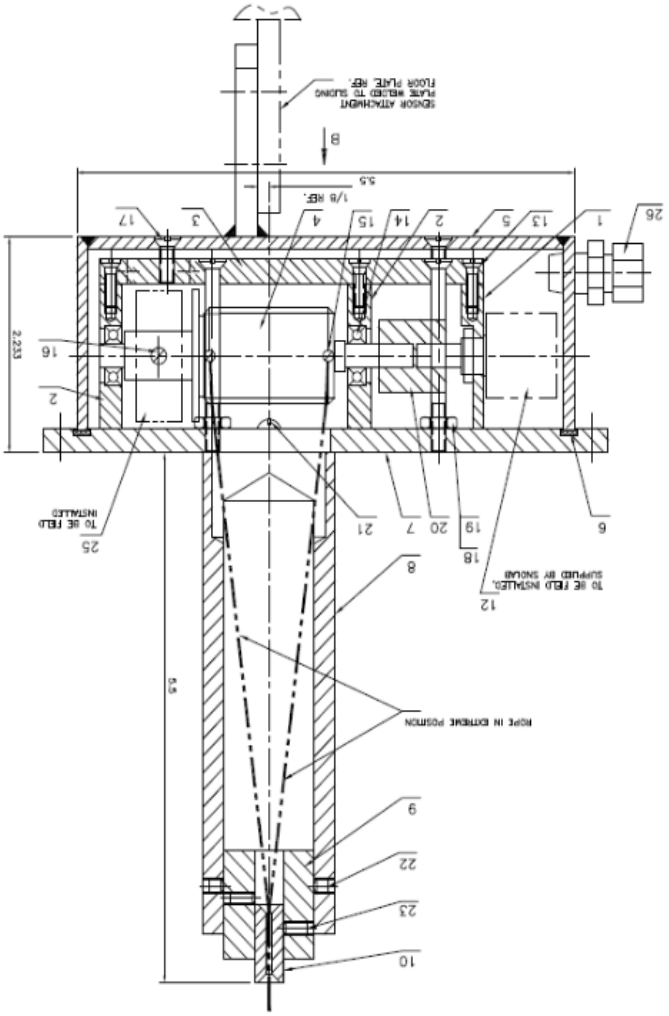

(a)

ITEM	DRAWING NUMBER	QTY	DESCRIPTION	MATERIAL
26		1	BRASS ADAPTOR ⅜" TUBE TO ⅜" NPT, McMASTER-CARR p/n 51875K65	
25		1	CONST. FORCE SPRING 301SS 1/2" WIDE, McMASTER-CARR p/n 9293K17	
24		2	#4x1/4" SS ROUND HEAD SCREW	
23		2	#6x¼" SS CUP POINT SET SCREW	
22		3	#8x¼" SS CUP POINT SET SCREW	
21		3	#6x½" SS ROUND HEAD SCREW	
20		1	AL. ANODIZED COUPLING ⅜"-⅜", ¾"LX⅝"OD, McMASTER-CARR p/n 9861T41	
19		2	#8 SS NUT	
18		2	#8x2" SS FLAT HEAD SCREW	
17		2	#8x1/2" SS FLAT HEAD SCREW	
16		1	#4x1/8" SS FLAT HEAD SCREW	
15		2	#2x1/4" SS ROUND HEAD SCREW	
14		2	SS B/BEAR. R4, O/SEAL ⅜"ODx½"IDx.196"Th. McMAS.-CARR p/n 4668K12	
13		6	#6x½" SS FLAT HEAD SCREW	
12		1	POTENTIOMETER 5 kOhm, SUPPLIED BY SNOLAB	
11	SLDO-SNP-0-1909-04	1	PLATE	
10	SLDO-SNP-0-1909-04	1	ROPE 304SS INSERT	
9	SLDO-SNP-0-1909-04	1	AL. INSERT	
8	SLDO-SNP-0-1909-04	1	HOLLOW BAR	
7	SLDO-SNP-0-1909-04	1	COVER PLATE	
6	SLDO-SNP-0-1902-02	1	⅛" BLACK NEOPRENE GASKET	
5	SLDO-SNP-0-1909-03	1	HOUSING	
4	SLDO-SNP-0-1909-02	1	BRASS DRUM	
3	SLDO-SNP-0-1900-02	1	INNER PLATE	
2	SLDO-SNP-0-1900-02	2	SIDE PLATE	
1	SLDO-SNP-0-1909-02	1	SIDE PLATE	

MATERIAL — FINISH

DRAWN: OLEG LI — DATE: OCT. 16/13 — SUBMITTED — APPD

TOL: FABRICATIONS +- 0.0625 U.N.O. MACHINED SURFACES +- 0.005 U.N.O. ANGLES +- 30' U.N.O. — SCALE: 1:1

ALL DIMENSIONS IN INCHES UNLESS OTHERWISE NOTED

SNOLAB, LIVELY, ONTARIO, P3Y 1N2, CANADA

TITLE: SNO+ AV POSITION SENSE ROPE DEVICE

DRAWING NUMBER: SLDO-SNP-AR-1909-01 Rev 0 — SHEET 1 OF 4

(b)

Figure B.1: The sense rope snout drawing (side view).

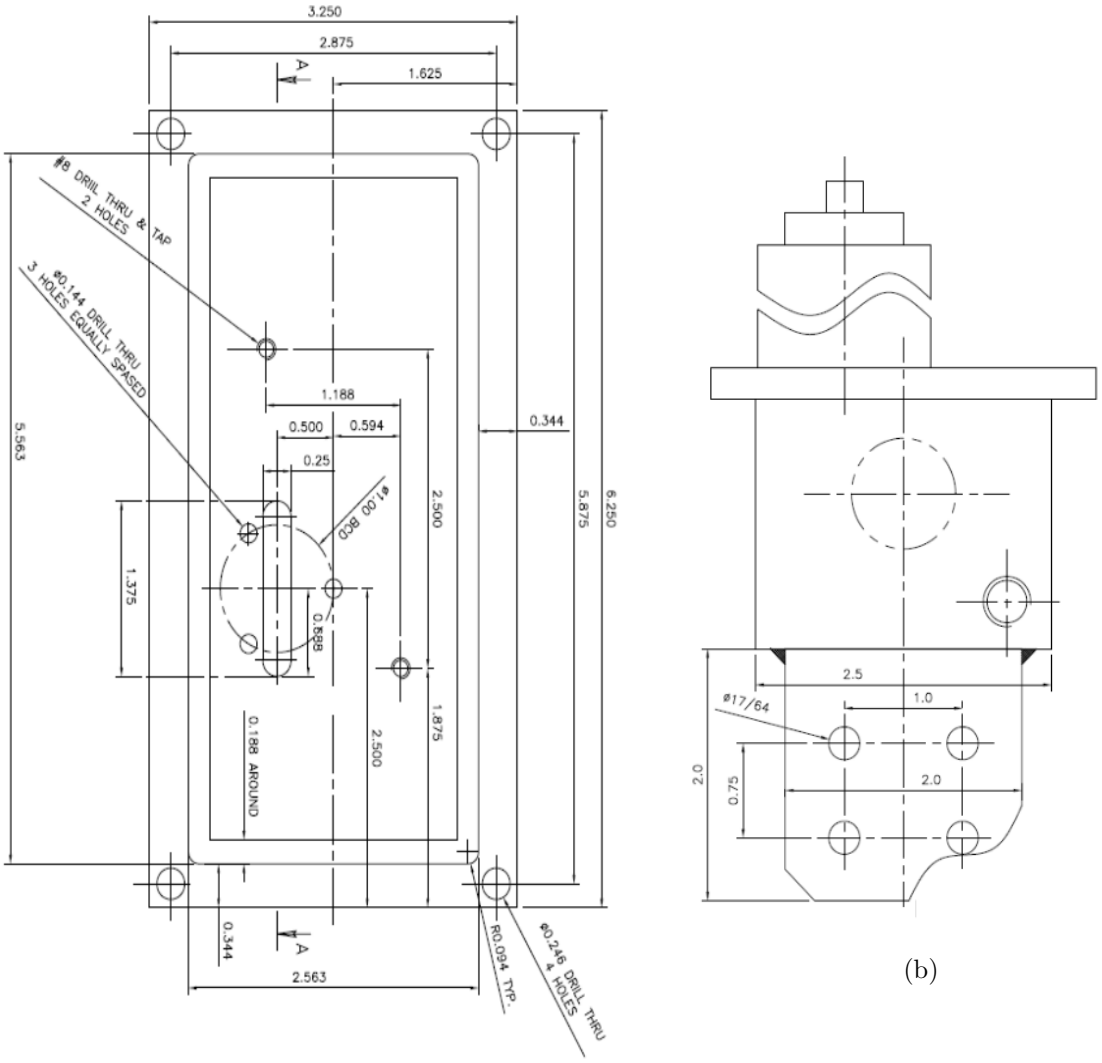

(a)

(b)

Figure B.2: (a): The sense rope snout drawing (top view) and (b) shows the side view.

Fixed plate and the Sensor Plates

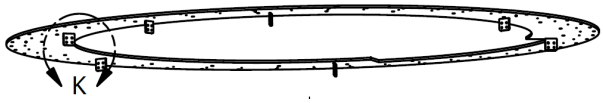

(a)

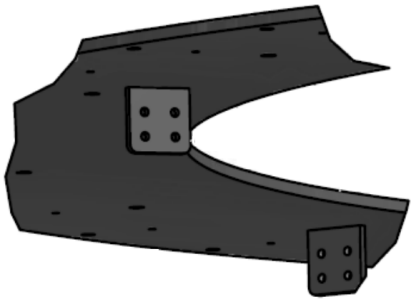

(b)

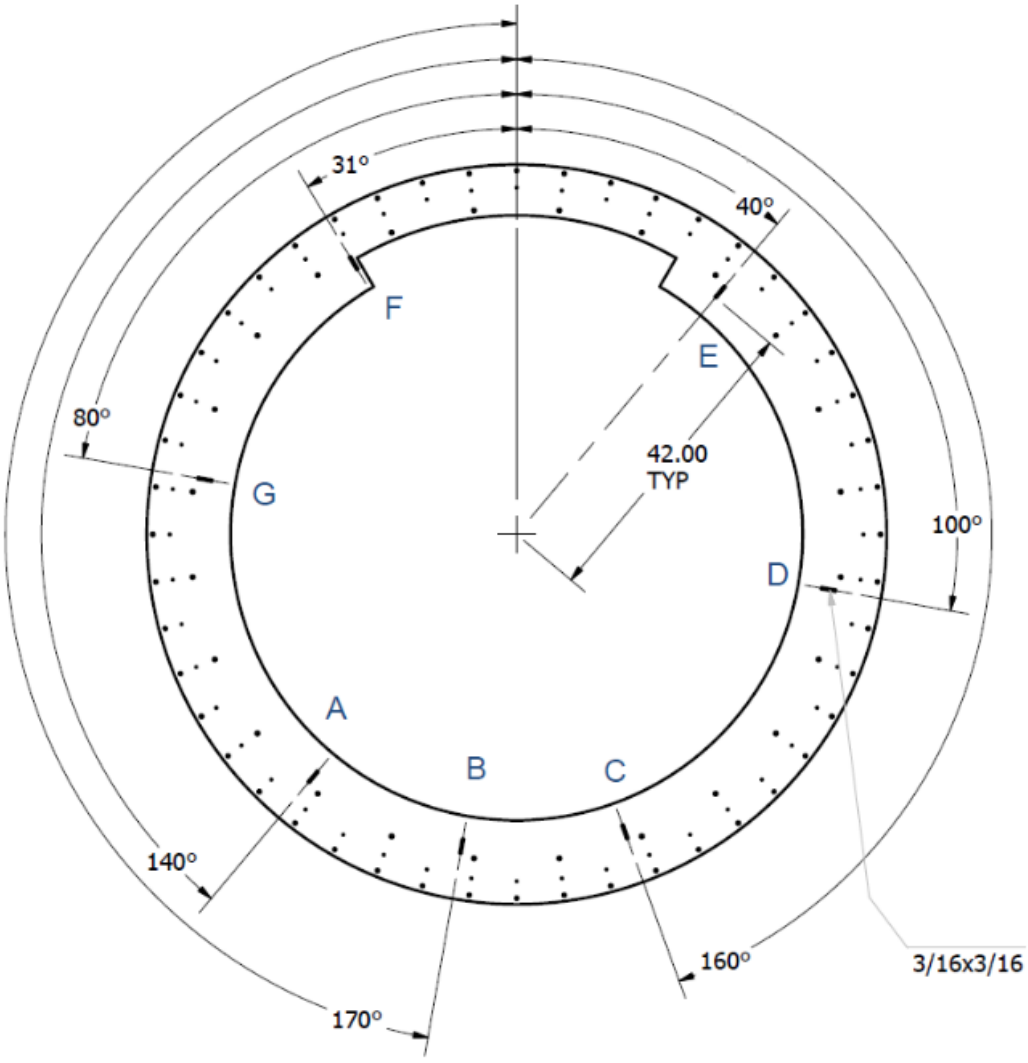

(c)

Figure B.3: (a): The sense rope fixed plate. (b): The square shape sensor plates welded on the underside of the fixed plate. (c): The fixed plate (top view).

Sense Rope Attachment Blocks

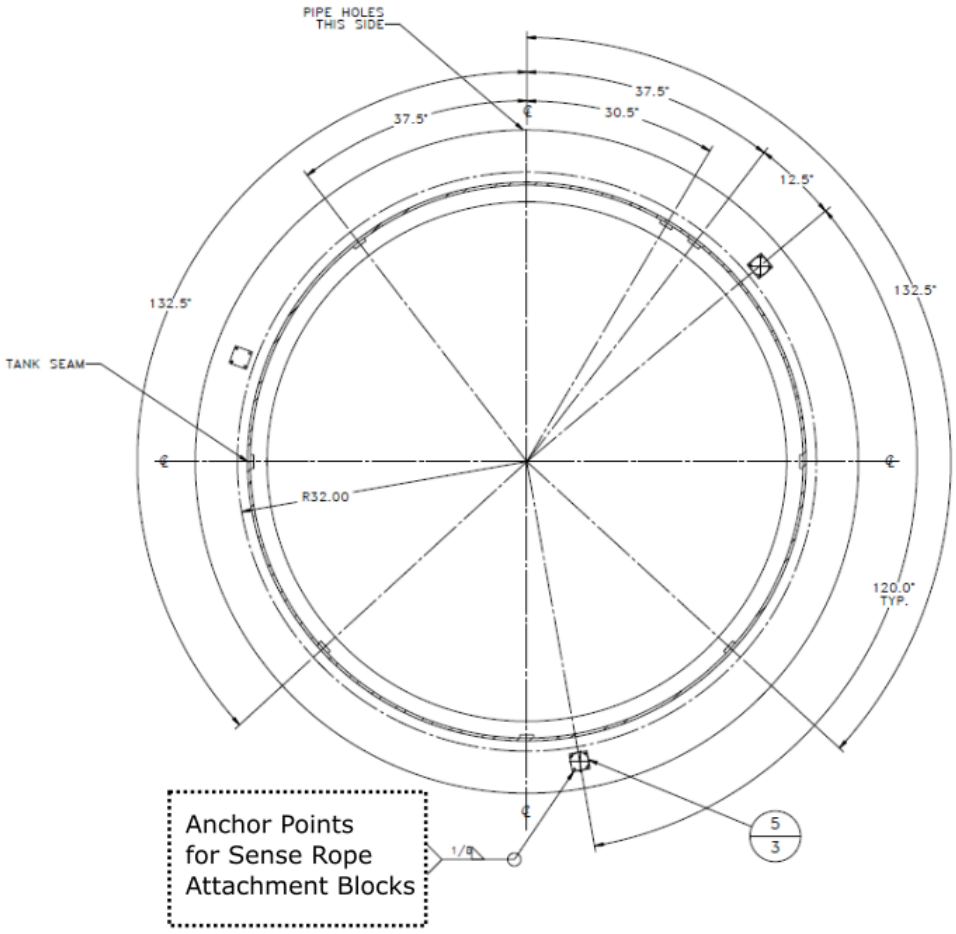

(a)

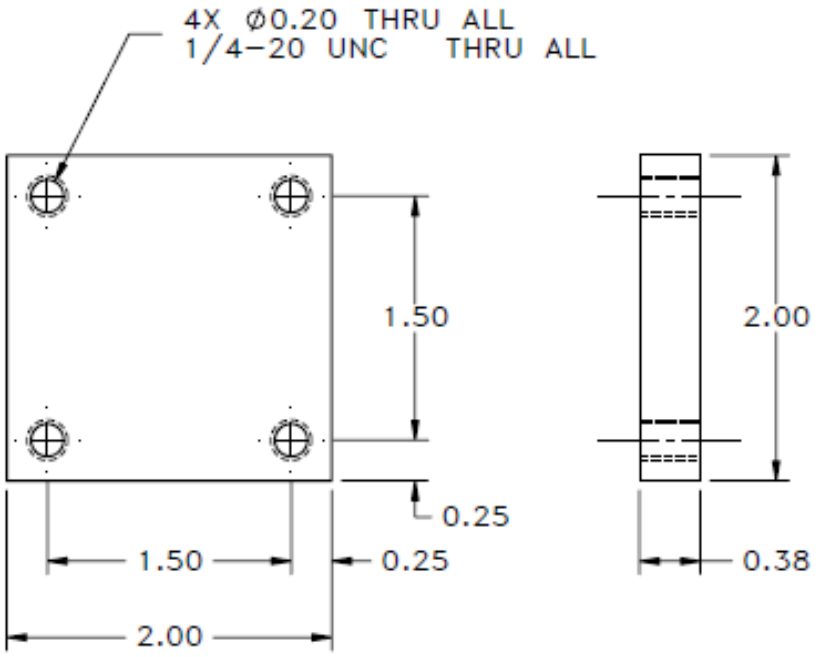

(b)

Figure B.4: (a): The top view of the lower UI and the position of three sense rope anchor points. (b) and (c): The sense rope attachment blocks.